Design and use of guided mode resonance filters for refractive index sensing

Hermannsson, Pétur Gordon

Publication date:
2015

Document Version
Publisher's PDF, also known as Version of record

Design and use of guided mode resonance filters for refractive index sensing

Pétur Gordon Hermannsson
PhD Thesis July 2015

DTU Nanotech
Department of Micro- and Nanotechnology

DTU Nanotech
Department of Micro- and Nanotechnology

Technical University
of Denmark

Design and use of guided mode resonance filters for refractive index sensing

Pétur Gordon Hermannsson
Ph.D. thesis
July 2015

Supervisor:
Prof. Anders Kristensen

Co-supervisors:
Christoph Vannahme
Cameron L.C. Smith

The cover picture shows several microscope images of guided mode resonance filters of varying periods. Although the structures are made from transparent materials, they exhibit resonant reflection in narrow wavelength intervals which depends on the period, leading to their different colors.

Abstract

This Ph.D. thesis is concerned with the design and use of guided mode resonance filters (GMRF) for applications in refractive index sensing. GMRFs are optical nanostructures capable of efficiently and resonantly reflecting a narrow wavelength interval of incident broad band light. They combine a diffractive element with a waveguiding element, and it is the coupling between diffracted light and quasi guided modes that gives rise to the resonant response.

The linewidth of the resonance can be tuned by the material and geometrical configuration of the device. The resonance wavelength is highly sensitive to changes in refractive index that occur within the region overlapped by the quasi guided mode, and GMRFs are thus well suited for optical sensing and tunable filter applications. They produce a polarization dependent response and can be optically characterized in both reflection and transmission.

The structures investigated in this thesis were fabricated in a process based on nanoreplication, in which the surface of a polymer was patterned with a structured master, cured with ultra-violet light and coated with a high refractive index material. The masters were defined using electron beam lithography, a lift-off process, and reactive ion etching.

After an introduction to the history and principles of GMRFs, the thesis describes the state-of-the-art of relevant research in the field, covers the necessary theoretical background required to understand their operation, and discusses the fabrication and characterization methods used. The thesis furthermore includes three journal articles. The first concerns an iterative computational model for the analytical prediction of the wavelengths at which resonances will occur, which is beneficial for e.g. device sensitivity optimization. The second paper discusses an all-polymer GMRF, which exhibits narrow resonance linewidths and a low detection limit, made by rapid and inexpensive fabrication methods. The third paper presents a novel method for measuring the refractive index dispersion of liquids using an array of GMRFs of different periods.

Resumé

Denne Ph.d.-afhandling omhandler design og anvendelse af såkaldte guidet "mode" resonansfiltre til brug indenfor brydningsindeks-følere. Guidet mode resonansfiltre er optiske nanostrukturer, som effektivt er i stand til resonant at reflektere indkommende bredspektret lys, i et snævert bølgelængdeinterval. De virker ved at kombinere et diffraktions-element med et bølgeledende element, og det er koblingen mellem det diffrakterede lys og en pseudo-guidet mode, som giver anledning til det resonante respons.

Resonansens linjebredde kan justeres gennem valg af enhedens materialer og geometriske konfiguration. Bølgelængden af den stående bølge er yderst følsom for ændringer i brydningsindeks i det område, hvor den pseudoguidede mode overlapper, og guidet mode resonansfiltre er derved velegnede til anvendelser indenfor optiske følere og justerbare filtre. De frembringer et polarisationsafhængigt respons, og kan karakteriseres optisk både i refleksion og transmission.

De strukturer, som blev undersøgt i denne afhandling, blev fremstillet i en process baseret på nanoreplikation, hvor en struktureret støbeform blev brugt til at lave et aftryk i en polymer-overflade, som derefter blev hærdet med ultraviolet lys, og belagt med et materiale af højt brydningsindeks. Støbeformene blev defineret med eletronstråle-litografi, en "lift-off" process og reaktiv ion-ætsning.

Efter en introduktion til historien og principperne bag guidet mode resonansfiltre, beskrives den nyeste forskning på området, den teoretiske baggrund som er nødvendig for at forstå, hvordan filtrene virker, samt endelig en diskussion af de metoder, som er anvendt under fabrikationen og karakteriseringen. Afhandlingen indeholder ydermere tre artikler udgivet i videnskabelige tidsskrifter. Den første omhandler en iterativ beregningsmodel til analytisk forudsigelse af den bølgelængde, hvorved resonanserne opstår, hvilket er særligt nyttigt f.eks. ved optimering af enhedernes følsomhed. Den anden artikel diskuterer et guidet mode resonansfilter fremstillet udelukkende i polymer, der udviser resonans med snæver linjebredde, samt en lav detektionsgrænse, og er produceret med hurtige og billige fabrikationsmetoder. En-

delig præsenterer den tredje artikel en nyskabende metode, hvorved væskers brydningsindeks-spredning kan måles med en række guidet mode resonans-filtre af varierende periode.

Preface

This thesis is submitted in partial fulfillment of the requirements for obtaining the Philosophiae Doctor degree at the Technical University of Denmark. The work presented here has been carried out in the Optofluidics group at the Department of Micro- and Nanotechnology, and in the DTU Danchip cleanroom facilities.

The project was supervised by professor Anders Kristensen, whom I thank for his invaluable guidance and insight, and providing me the opportunity to pursue my degree in a world-class research facility. Furthermore, I'm greatly indebted to my co-supervisors, Christoph Vannahme and Cameron Smith; without their enthusiastic support, this work would not have seen fruition.

I would further like to thank my colleagues at the Optofluidics group, past and present, for helping create an enjoyable work atmosphere. I am particularly grateful to my office mates Alexander B. Christiansen for all the great laughs we shared, and Kristian T. Sørensen for helping me vastly improve my (still limited) danish skills.

I gratefully acknowledge funding from the NaPANIL, PolyNano and Cell-o-matic projects, as well as Otto Mønsted Fonden for travel support.

Finally, I would like to thank my loving wife Gunnur Ýr for her support and encouragement, and our wonderful son Birkir Hrafn, who during this thesis-writing fortunately managed to regularly convince me to join him in the living-room to play.

List of publications

Journal articles:

I **P.G. Hermannsson**, C. Vannahme, C.L.C. Smith, and A. Kristensen, *Absolute analytical prediction of photonic crystal guided mode resonance wavelengths*, Applied Physics Letters **105**, 7, 071103 (2014)

II **P.G. Hermannsson**, K.T. Sørensen, C. Vannahme, C.L.C. Smith, J.J. Klein, M. Russew, G. Grützner, and A. Kristensen, *All-polymer photonic crystal slab sensor*, Optics Express **23**, 13, 16529-39 (2015)

III **P.G. Hermannsson**, C. Vannahme, C.L.C. Smith, K.T. Sørensen, and A. Kristensen, *Refractive index dispersion sensing using an array of photonic crystal resonant reflectors*, Applied Physics Letters **107**, 6, 061101 (2015)

Contributions to other work:

I C. Vannahme, M.C. Leung, F. Richter, C.L.C. Smith, **P.G. Hermannsson**, and A. Kristensen, *Nanoimprinted distributed feedback lasers comprising TiO_2 thin films: Design guidelines for high performance sensing*, Laser & Photonics Reviews **7**, 6, 1036-42 (2013).

Conference proceedings:

I **P.G. Hermannsson**, C. Vannahme, C.L.C. Smith, and A. Kristensen, *Accurate wavelength prediction of photonic crystal resonant reflection and applications in refractive index measurement*, IEEE SENSORS 2014 Proceedings, Valencia, Spain, 2-5 Nov. 2014.

Oral conference presentations:

1. **P.G. Hermannsson**, C. Vannahme, C.L.C. Smith, and A. Kristensen, *Nanoreplicated Photonic Crystal Resonant Reflectors for Refractive Index Sensing*, 40th International Conference on Micro and Nano Engineering, Lausanne, Switzerland, September 25th, 2014.

2. **P.G. Hermannsson**, C. Vannahme, C.L.C. Smith, and A. Kristensen, *Accurate Wavelength Prediction of Photonic Crystal Resonant Reflection and Applications in Refractive Index Measurement*, IEEE Sensors 2014, Valencia, Spain, November 4th, 2014,

3. **P.G. Hermannsson**, K.T. Sørensen, C. Vannahme, C.L.C. Smith, J.J. Klein, M. Russew, G. Grützner, and A. Kristensen, *Low-cost polymer guided mode resonance filters for sensing applications*, 3rd EOS Conference on Optofluidics, Munich, Germany, June 23rd, 2015.

Patent application:

1. **P.G. Hermannsson**, C. Vannahme, C.L.C. Smith, and A. Kristensen, *Method of and system for identification or estimation of a refractive index of a liquid*, European patent application no. 14164354.4 (April 11, 2014).

Contents

Abbreviations

Abbreviation	Description
AFM	atomic force microscopy
CCD	charge-coupled device
DFB	distributed feedback (laser)
EBL	electron beam lithography
FP	Fabry-Pérot
FSR	free spectral range
FWHM	full width at half maximum
GMRF	guided mode resonance filter
IBSD	ion beam sputter deposition
LIL	laser interference lithography
PMMA	poly(methyl methacrylate), a polymer
Q factor	quality factor
TE	transverse-electric
TM	transverse-magnetic
UV	ultra-violet
VASE	variable angle spectroscopic ellipsometry

1 Introduction

1.1 Historical overview

Even though the principles of diffraction had been known since the time of Newton, it was Rittenhouse who in 1786, produced the first man-made diffraction grating from hairs spaced by the threads of two fine screws [1]. Years later, in 1902, Wood noticed unexpected rapid intensity variations in light reflected by a metallic grating in response to small changes in incident angle and wavelength [2]. In his experiments, Wood observed that when illuminating the grating with incandescent light polarized perpendicular to the grating grooves, the diffracted spectrum exhibited rapid intensity increases of a factor of ten in a wavelength interval "not greater than the distance between the sodium lines" [2]. These anomalous effects became known as Wood's anomalies, as they could not be explained by ordinary theory of diffraction. In his attempt to shed light on these anomalies, Lord Rayleigh theoretically analyzed the grating structure, and noticed that Wood's anomalies correspond to wavelengths at which new propagating diffraction orders emerge from the grating at the grazing angle (i.e. propagating along the surface), which lead to a rapid redistribution of the total power in the various diffraction orders [3]. Rayleigh had assumed a perfectly conducting, and thus, a perfectly reflecting grating material, but as Fano discovered in 1941 [4], assuming lossy metal gratings, he was able to distinguish between two types of anomalies: a Rayleigh-type, characterized by an "edge" in the intensity, and a second type he termed as being "diffuse", characterized by a minimum and maximum in intensity [5]. Although Wood had only observed anomalies when the electric field polarization was perpendicular to the grating grooves, it was later shown by Palmer that if the grooves are deep enough, anomalies will also occur when the polarization is parallel to the grooves [6]. In 1965, Hessel & Oliner employed a novel theoretical approach to explain Wood's anomalies based on guided waves rather than the scattering approach that had been used up until then, and showed that the second type of anomaly was a resonance phenomenon due to "guided complex waves supportable by

the grating", i.e. leaky waves with complex wavenumbers [7].

In 1973, Neviere et al. published two theoretical studies of light diffracted by non-metallic grating structures composed of dielectric waveguides coated with corrugated photoresist. These structures were shown to exhibit a resonant response with respect to the angle of incidence, both when the polarization of incident light was perpendicular [8] and in parallel [9] to the grating grooves, and the authors related this behavior to the existence of optical modes in the waveguide. In 1985, Mashev & Popov experimentally demonstrated a resonance anomaly in the zeroth reflected diffraction order due to the excitation of guided waves in a corrugated waveguide, which significantly increased the reflectance of the structure in a narrow wavelength band [10]. In 1989, Bertoni et al. demonstrated that total transmission or total reflection of light could be obtained at different frequencies for a dielectric slab structure composed of alternating square bars of different refractive indices. They explained this behavior in terms of excited leaky waves guided by the structure, which became re-radiated both above and below the structure and combined with the directly reflected and transmitted light. When the re-radiated light was out of phase with the reflected light, strong transmission occurred, whereas strong reflection occurred when the two components were in phase. Furthermore, they showed that since the phases were frequency dependent, the reflection exhibited a (resonant) frequency selective behavior [11]. In 1990, Gale et al. experimentally demonstrated highly efficient resonant reflection from dielectric grating structures operating in the visible regime, intended for applications in security and anti-counterfeiting systems [12].

In the early 1990s, Wang & Magnusson published several papers on the diffraction efficiency of subwavelength planar all-dielectric grating waveguides. They demonstrated that a 100% exchange of optical energy between the forward and backward propagating diffraction orders could be achieved over narrow wavelength ranges or incident angle intervals due to coupling of externally propagating diffracted waves to modes of the waveguide [13–18]. They based their work on earlier analysis by Gaylord & Moharam of similar dielectric grating structures using rigorous coupled wave analysis [19, 20]. In their papers, Wang & Magnusson coined the term "guided mode resonance filters" for such resonant grating waveguide structures, and suggested several applications and uses for them, including laser cavity mirrors, polarizers, tunable filters, and electro-optic switches [15]. In 1996, Peng & Morris published both theoretical and experimental studies that demonstrated that resonant reflection is not exclusive to one-dimensional grating waveguides, but is also a feature of two-dimensional structures. Two-diminsional dielectric grating waveguides were shown to give rise to two resonance peaks in

the reflected spectrum when illuminated at normal incidence, instead of the one exhibited by analogous one-dimensional devices [21,22]. In 1997, Sharon, Rosenblatt & Friesem presented a simple ray picture model to explain how light transmitted through dielectric grating waveguide structures is extinguished by total destructive interference when a condition for the waveguide supporting a guided mode is fulfilled, leading to complete reflection at resonance. They furthermore experimentally demonstrated semiconductor-based resonant grating waveguides operating in the visible regime [23, 24]. Finally, in 2002, Fan & Joannopoulos employed three-dimensional photonic crystal theory to analyze the transient behavior of the transmission and reflection through a two-dimensional grating waveguide, which they referred to as a photonic crystal slab. They demonstrated that such structures are able to sustain two types of guided waves, conventional guided modes with infinite lifetimes that do not couple to the far field, and so-called guided resonances that do, and have finite lifetimes as a result [25].

By communicating his curious findings, Wood inadvertently sparked a new field of research within physics, which eventually gave rise to resonant grating waveguide structures capable of exhibiting highly efficient resonant reflection in narrow wavelength bands, which lie at the heart of this thesis. Due to their long history, in which many independent groups and individuals contributed to their understanding, such resonant grating waveguides have become known by several different names in the literature, such as guided mode resonance filters, photonic crystal slabs, or simply photonic crystal resonant reflectors. This depends in part on which branch of optics they are described and understood by, e.g. rigorous coupled wave analysis, or photonic crystal theory. In this thesis, these structures are exclusively referred to as guided mode resonance filters (GMRF), but it should be kept in mind that this is simply a matter of convention and consistency.

1.2 Principles of guided mode resonance filters

Guided mode resonance filters are essentially dielectric slab waveguide structures, in which the waveguide core is in some way periodically modulated, such as by periodic variations in refractive index, waveguide core thickness, or position of the waveguide core. Most of the guided mode resonance filters under study in this thesis are of the third type, in which a high refractive index waveguide core layer (n_2) of thickness t is supported by a low-index substrate (n_3) with a periodic surface height modulation of amplitude h and period Λ, as illustrated in Fig. 1.1. The surface of the high-index layer is further exposed to a superstrate medium of refractive index n_1. By introduc-

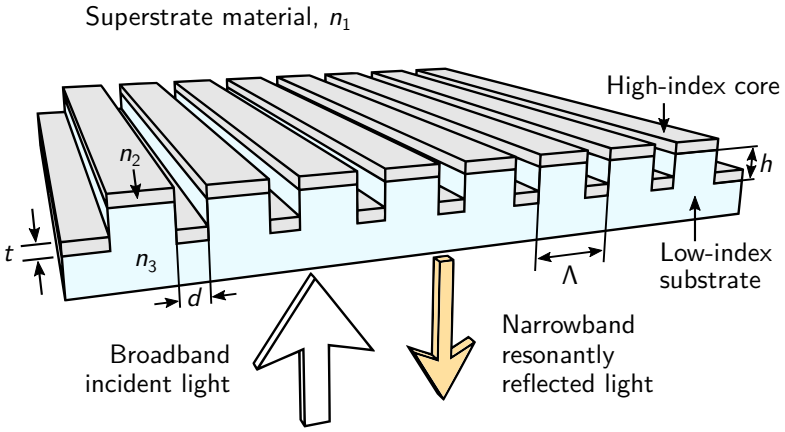

Figure 1.1: Schematic illustration of a guided mode resonance filter and its operation. Normally incident broadband light is resonantly reflected in a narrow wavelength interval, corresponding to the refractive index in the superstrate.

ing a periodicity into the waveguide structure, it exhibits properties of both diffraction gratings and waveguides, and guided modes in the waveguide can couple to externally propagating diffracted light. When under the illumination of out-of-plane incident light, guided modes can be excited within the waveguide core. However, due to the periodicity, as they propagate, they continually leak out energy into the far-field and are thereby attenuated over distance. For this reason, instead of referring to them as guided modes, they are more appropriately termed leaky or quasi-guided modes. As with conventional guided modes, their electric field amplitude takes a maximum in the high-index layer, and then decays exponentially away from it. The light that is de-coupled out of the structure interferes with both the transmitted and reflected light, and at a certain resonance wavelength, the de-coupled light interferes destructively with the transmitted light and constructively with the reflected light, resulting in highly efficient resonant reflection for a particular wavelength interval. An example of such a resonantly reflected spectrum is shown in Fig. 1.2. Naturally, the wavelength at which guided mode resonance filters exhibit resonance depends on the refractive indices of the materials they are composed of, as well their geometrical configuration, such as period and high-index layer thickness. Furthermore, depending on whether the incident light is polarized in parallel to the grating grooves, or perpendicular to them, either transverse-electric (TE) or transverse-magnetic (TM) polarized quasi guided modes will be excited. Due to the inherent difference in the characteristics of these modes, they lead to resonant reflection at separate wavelengths, and thus, guided mode resonance filters essentially

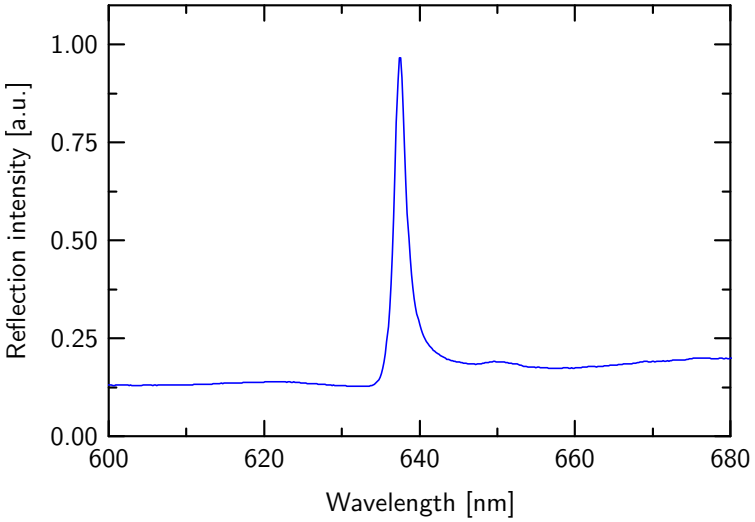

Figure 1.2: The spectrum of resonantly reflected light from a guided mode resonance filter composed of a polymer substrate with a surface height modulation period of $\Lambda = 384$ nm and a titanium dioxide high-index waveguide core covered with water. The resonance is due to the excitation of a TM-polarized quasi guided mode.

behave as wavelength-selective polarizers. As a result, their resonance spectra can be optically characterized in either reflection, or in transmission by placing them between two orthogonally oriented linear polarizers. In the latter, resonances associated with both TE and TM quasi guided modes will inherently be simultaneously measured. Figure 1.3(a) shows resonance spectra acquired in transmission for a guided mode resonance filter in which the refractive index of the superstrate is varied. As the figure illustrates, the higher the superstrate refractive index is, the more the resonance is shifted to longer wavelengths. Figure 1.3(b) shows corresponding photographs of the structure for each of the different superstrate materials.

When the periodicity of the waveguide modulation becomes smaller than the wavelength of the incident light, only the zeroth diffracted orders can propagate with all higher orders cut-off. This can in theory lead to a reflection efficiency of up to 100% at resonance, but is in practice limited by scattering and absorption losses, structural imperfections etc. The linewidth, i.e. quality factor, of the resonance depends on the rate of de-coupling of the quasi guided mode (i.e. photon lifetime), with lower rates of de-coupling (longer lifetimes) leading to narrower linewidths. Factors that influence the rate of de-coupling include refractive index contrast between waveguide core and cladding, core thickness t, grating height h, and grating duty cycle.

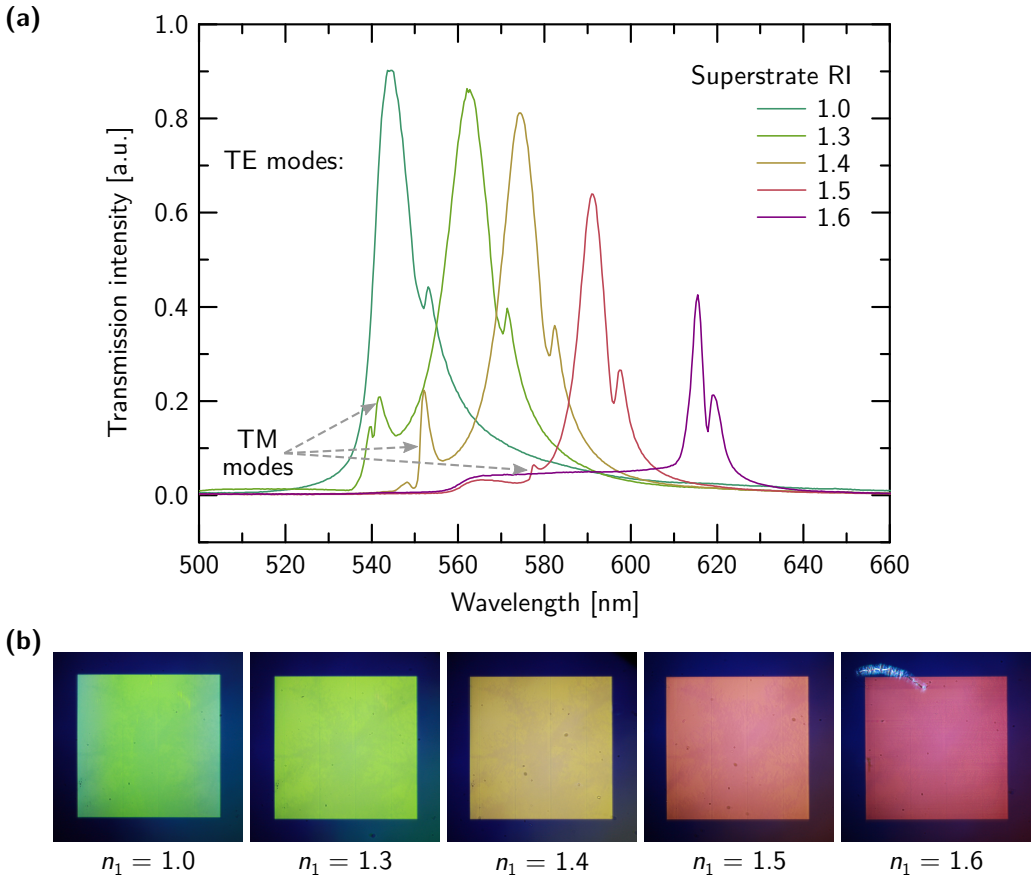

Figure 1.3: (a) The resonance spectra of a 2×2 mm^2 guided mode resonance filter, composed of a low refractive index polymer ($h = 100$ nm, $\Lambda = 384$), covered with a $t = 30$ nm thick titanium dioxide high-index layer, covered with transparent media (i.e. superstrate material) of varying refractive index. (b) Corresponding photographs of the structure when covered with each of the different superstrate materials.

Guided mode resonance filters are commonly fabricated by directly structuring a high refractive dielectric material on a substrate of lower refractive index using lithographic patterning and etching. Another technique, one that is exclusively used in this thesis, is the deposition of a high refractive index material onto a pre-structured periodic substrate, yielding a device such as the one shown in Fig. 1.1. The substrates can be structured directly using electron-beam or photolithography, or alternatively by pattern transferal from a pre-defined master or shim, using e.g. thermal nanoimprint lithography, ultra-violet nanoreplication, or injection molding. In addition to being fast and inexpensive, such approaches have the added benefit that the

electron-beam or photolithography must only be performed once to produce the master, and its cost is distributed over a multitude devices. Guided mode resonance filters can be produced from a wide variety of materials, with popular choices for the high-index core layer including titanium dioxide, tantalum pentoxide, indium tin oxide, hafnium oxide, and silicon nitride.

1.3 Applications in sensing

In the past two decades, thanks to advances in micro- and nanolithography techniques, coupled with the cost-reduction and increased availability of such methods, guided mode resonance filters have found numerous and varied uses in a range of different applications. This has further been aided by advances in computing, which have made accurate optical simulations more accessible. Early on, guided mode resonance filters were primarily of interest in optical filtering and switching applications, such as polarization sensitive and wavelength-selective mirrors, electro-optic switches and tunable filters. However, due to the fact that their resonance spectra can be highly sensitive to refractive index changes in the vicinity of the high-index waveguide core, guided mode resonance filters have been increasingly utilized in a range sensing applications.

Within the field of biological sensing, monitoring of e.g. biological interactions, kinetic processes, and cellular responses to chemical stimuli, has traditionally required the use of fluorescent dyes, radioactive labels, and staining agents. However, the presence of such labels may cytotoxic and interfere with the processes being investigated. As a result, there has been significant emphasis on developing so-called label-free biological sensors which rely instead on biological or chemical receptors to detect target analytes [26]. Guided mode resonance filters are increasingly playing a role in label-free sensing applications, and are implemented such that a layer of receptor molecules is immobilized on the surface of the high-index layer. Selective binding of target molecules to this recognition layer induces a wavelength shift in the resonance spectrum which, in addition to signifying the presence of the target, can yield information about the binding kinetics. More recently, guided mode resonance filters have further been demonstrated in label-free surface imaging as well as three-dimensional imaging applications.

In the field of optical and label-free sensing, there are many competing technologies. Of these, surface plasmon resonance sensing has seen the most widespread industrial adoption. This method is typically implemented such that a laser is used to illuminate a spot on a metallic surface at a range of incident angles, and the reflected intensity is recorded as a function of

reflection angle. At a specific angle, the incident light couples to surface waves on the metal interface which manifests itself as a drop in intensity at the corresponding angle of reflection. The coupling angle depends on the refractive index at the surface of the metal, so if a recognition layer is present, selective molecular binding can be registered as a change in angle at which the reflected intensity drop occurs.

Guided mode resonance filters have several advantages over the surface plasmon resonance technique. Surface plasmon resonance requires the use of a prism in order to couple light into the surface waves, as well as a laser illumination source. In contrast, guided mode resonance filters can be illuminated with inexpensive broadband light sources, such as incandescent lamps or light emitting diodes, and do not require the use of prisms or other external phase-matching elements. Since surface plasmon resonance sensors involve metal surfaces, their transmission is limited, whereas guided mode resonance filters are generally made from transparent materials. As a result, they can be used as transparent microscope slides that combine the capabilities of microscopy with refractive index detection. Furthermore, due to the comparatively long propagation lengths of surface plasmon waves, the method is not well-suited for surface imaging, in contrast to guided mode resonance filters.

Label-free biological sensing has also been pursued using distributed feedback dye lasers, where refractive index changes at the laser surfaces lead wavelength shifts in the emission spectra. The main advantages of such laser sensors is the narrow linewidth of the transduced optical signal, and the speed at which measurements can be performed. The sensors achieve lasing by the incorporation of a dye gain medium into the device structure and optical pumping with a high power pulsed laser. Unfortunately, high power lasers are expensive, and as a result, the laser sensors are not very attractive for low-cost sensing applications. Moreover, the laser sensors have limited lifetimes as the dye molecules eventually undergo a permanent photochemical change which prevents them from emitting light, known as bleaching. In contrast, guided mode resonance filters neither require an optical pumping source, nor a gain medium.

Guided mode resonance filters thus have many advantages over other competing technologies in the field of sensing. They can be made cheaply and quickly using nanoreplication methods, and the structures can be used repeatedly if properly cleaned. They can be fabricated from a variety of different materials to fit the application at hand, and do not require the incorporation of a gain medium in order to function. They exhibit narrow resonance linewidths, yet high sensitivity to refractive index changes, and the distance into which they probe a sample can be tuned e.g. by the ap-

propriate choice of materials and high-index layer thickness. They require only very modest equipment for measuring their resonance spectra, such as a broadband light source, an optomechanical system for positioning, simple optical components for collecting the reflected or transmitted light, and a spectrometer for analyzing the measured spectra. There is thus no need for laser light sources, pulsed laser pumps or other sophisticated light sources, and the resonance spectra can be measured either in reflection or in transmission, depending on the application. Furthermore, since refractive index changes are measured optically, there is no direct physical contact with the specimens, such by electrodes etc.

1.4 Thesis outline

This thesis is concerned with the design and use of guided mode resonance filters for sensing applications. It represents the Optofludics group's first steps into the field of guided mode resonance filters, and lays the foundation in terms of understanding, fabrication, and experimental instrumentation upon which future work in this field will be based. In addition to this, key topics of this thesis include fabrication and device cost-reduction, providing an intuitive understanding of which wavelengths the structures will exhibit resonance, and using that understanding to enable accurate, absolute refractive index dispersion measurements. Following this introduction, the remainder of this thesis is organized as follows:

Chapter 2 reviews the state-of-the-art of guided mode resonance filters used in tunable filter, and sensing applications.

Chapter 3 provides a theoretical background of the operation of guided mode resonance filters.

Chapter 4 covers the methods used to fabricate the guided mode resonance filters used in this thesis, and explains the experimental setups used to measure their resonance spectra, both in transmission, and in reflection.

Chapter 5 summarizes, and elaborates on the journal articles submitted as part of this thesis, which then follow.

Chapter 6 gives a summary, followed by an outlook for possible future work involving guided mode resonance filters.

2 | State of the art

Since their inception, guided mode resonance effects have been utilized in a wide range of different applications, such as wavelength selective mirrors and polarizers [15], waveplates [27], ultra-broadband mirrors [28], non-polarizing narrowband mirrors [29,30], high efficiency passive reflection (bandstop) [31] and transmission (bandpass) [32, 33] filters, and absorption enhancement in solar cells [34, 35]. In addition to such passive filter applications, the ability of GMRFs to support narrow and polarization dependent resonant reflection that is sensitive to refractive index changes and angle of illumination incidence, makes them ideal for tunable filtering and sensing applications.

This chapter reviews the state of the art of applied research involving guided mode resonance filters. Due to the breadth of the field, the scope of the discussion is limited to tunable filter and refractive index sensing, in particular biological sensing and surface imaging. Tunable filtering and sensing are closely related topics as they rely on the same physical principles, and differ mainly by whether a change in resonance spectrum is intentionally induced, or whether it is caused by a process that is being sensed. When guided mode resonance filters were first proposed, their primary application was expected to be in regards to optical filtering, and thus, the discussion starts there.

2.1 Tunable optical filters

In order to tune the output of an active[1] optical device, a refractive index change must be induced in a region overlapped by the light in the system. Options for electrical actuation of refractive index changes include aligning nematic phase liquid crystals by applied electric fields [36], inducing a charge accumulation at semiconductor-insulator interfaces [37], and generating a thermo-optic refractive index change by resistive heating [38, 39]. For the

[1] Active in this contexts refers to the ability to actuate the device's behavior by e.g. optical, electrical or thermal means.

case of optical actuation, active photonic devices based on azobenzene dyes [40] and rhodopsin have been studied [41]. Refractive index tuning using azobenzene has been shown to achieve greater index changes than rhodopsin ($\Delta n = 10^{-1}$ v.s. 10^{-3} RIU [42, 43]), but occur on time-scales on the order of minutes, compared to microseconds for rhodopsin.

In order to tune the resonant response of a guided mode resonance filter, a refractive index change must be induced within the evanescent decay length of the associated quasi-guided mode. An optically tunable guided mode resonance filter based on refractive index changes in azobenzene molecules has been demonstrated, in which the superstrate of the GMRF constituted a PMMA polymer matrix into which azobenzene molecules[2] had been incorporated [42]. Under the illumination of a specific wavelength of light, azobenzene molecules can be excited from a so-called *trans* state to a higher energy *cis* state, which is more compact and less optically dense. By simultaneously illuminating the aforementioned dye-doped GMRF with broadband light and a laser with an emission wavelength that matched the absorption spectrum of the dye, it was shown that the refractive index of the dye-doped polymer could be reduced, leading to wavelength tuning of the GMRF's resonance spectrum, as shown in Fig. 2.1(a). The figure shows the peak wavelength of resonant reflection resulting from normally incident broadband light as a

[2]Namely, N-ethyl-N-(2-hydroxyethyl)-4-(4-nitrophenylazo)aniline

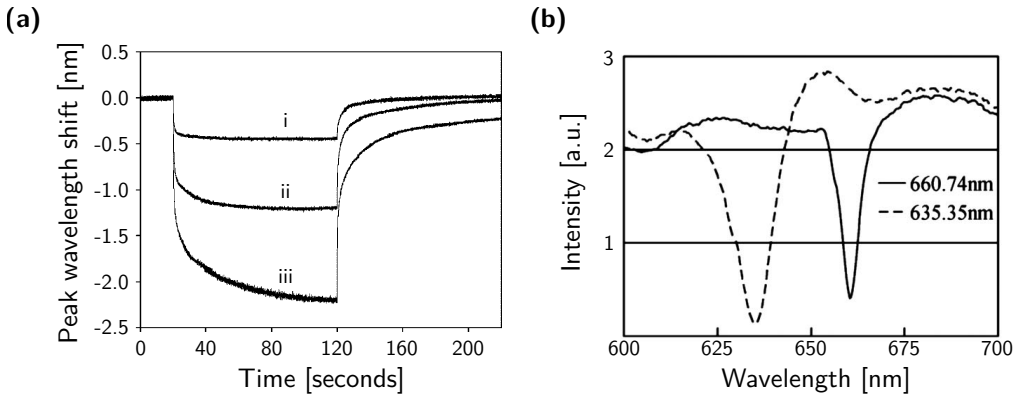

Figure 2.1: (a) The change in measured peak resonance wavelength as a function of time for a GMRF with an azobenzene-doped PMMA superstrate, when illuminated with TE-polarized light and a laser source with a power of: (i) 10 mW, (ii) 62 mW and (iii) 124 mW. The figure is adapted from Ref. [42]. (b) The transmission spectrum for TE polarized light passed through a GMRF with an azobenzene liquid crystal superstrate, before (solid) and after illumination with 30 mW laser light (dashed). The figure is adapted from Ref. [44].

function of time for three different laser excitation powers. A maximum peak wavelength tuning of 2.5 nm, corresponding to a refractive index change of around 0.09 RIU, was demonstrated after illumination with a laser intensity of 124 mW for two minutes. This behavior was demonstrated for both for transverse-electric (TE) and transverse-magnetic (TM) polarized resonances, and upon discontinuation of laser illumination the peak wavelengths relaxed to their initial positions on a time scale of minutes. An alternative approach was furthermore demonstrated, in which the azobenzene molecules were suspended in isopropanol instead of PMMA, resulting in a tunability of up to 14 nm with a laser excitation power of 600 mW [42]. Optical tunability of the spectral transmission dip in light passed through a GMRF structure has further been demonstrated with the use of an azobenzene-liquid crystal superstrate [45]. Here, a tunability of up to 25 nm was achieved with an applied laser power of 30 mW, as shown in Fig. 2.1(b).

Electrical tuning of resonant reflection from a guided mode resonance filter has also been demonstrated by using a liquid crystal solution as a superstrate material [45]. Here, tuning was achieved by applying a voltage bias to two transparent indium tin oxide electrodes on either side of the device, as shown in Fig. 2.2(a). The applied bias caused the liquid crystals to align to the resulting electric field, and produced a refractive index increase in the direction normal to the device surface, while simultaneously reducing the refractive index in the direction parallel to the surface. This directional

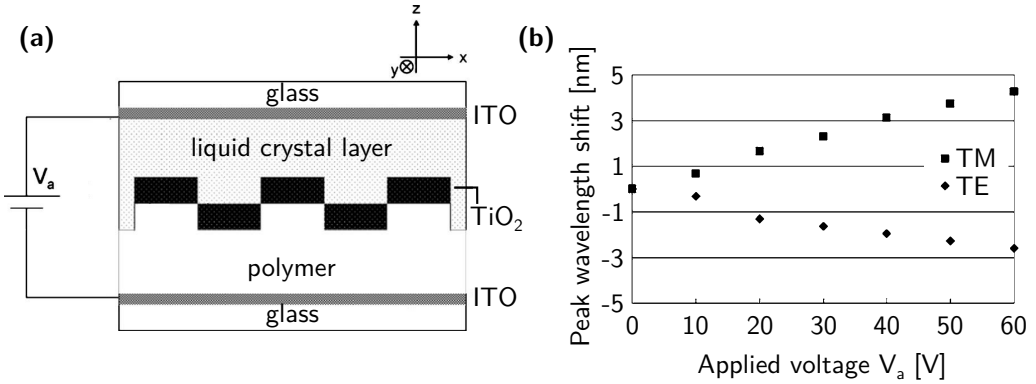

Figure 2.2: (a) Schematic illustration of an electrically actuated tunable GMRF based on aligning nematic liquid crystal molecules to an electric field generated between two transparent indium-tin-oxide (ITO) electrodes. (b) The peak wavelength shift of resonance peaks associated with TE and TM polarized modes, as a function of applied bias. The two peaks move in opposite directions due to the directional nature of electrically induced refractive index changes in liquid crystals. The figure is adapted from Ref. [45].

refractive index change was shown to affect the excited TE and TM quasi guided modes differently, with TE modes experiencing a reduction in refractive index and thus their associated peak resonance wavelengths were shifted to lower values, whereas TM modes experienced an increase in refractive index and the associated peaks were shifted to greater values, as illustrated in Fig. 2.2(b).

Since the refractive index of materials is inherently dependent temperature, the resonance spectra of GMRFs can in principle be controlled by thermal means. In fact, a thermo-optically tunable guided mode resonance filter exhibiting narrowband resonant reflection with a FWHM of 7 nm at telecommunication wavelengths has been experimentally demonstrated [46]. In this work, a periodic grating was etched into a high index amorphous silicon layer, which simultaneously served as a waveguide and electrical conductor, and was supported by an insulating glass substrate. By passing a current through the amorphous silicon layer and thereby increasing its refractive index by Joule heating, a peak-wavelength tuning of 15 nm due to an electrically induced temperature increase of 100 °C was demonstrated.

Barring tuning by means of refractive index changes, or structural tuning by, say, stretching, the resonance spectra of GMRFs can also be tuned, in a manner of speaking, by the angle of incidence of the illumination source. However, when the angle of incidence deviates from zero, the resonance peak becomes split and the structure exhibits resonant reflection at two separate wavelengths, which is unfavorable behavior for e.g. color filtering applications. Given a device's refractive index parameters, by careful selection of the

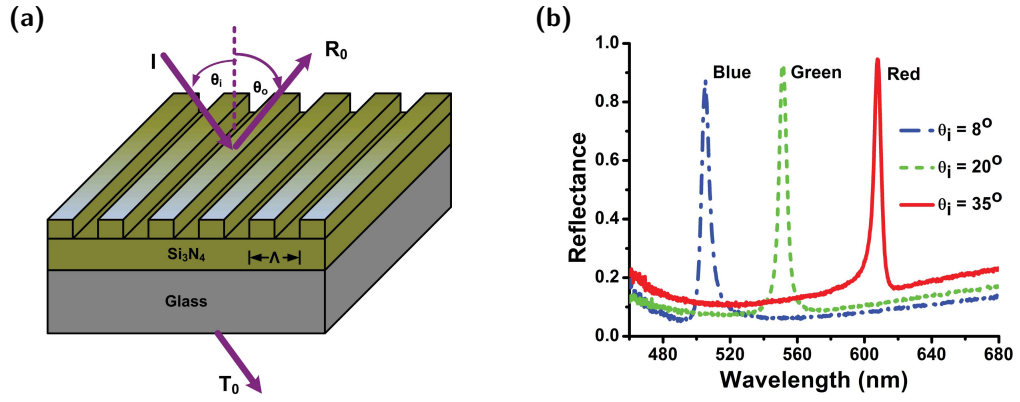

Figure 2.3: (a) A high efficiency angle-tunable color reflection filter composed of a silicon nitride subwavelength grating waveguide layer on glass. (b) The three primary colors obtained by tuning the angle of incidence of the broadband illumination. The figure is from Ref. [47]

grating's geometrical parameters, the device can be engineered so that one of these reflected peaks exists outside of the visible wavelength spectrum, and is thus invisible to the human eye. Figure 2.3(a) shows such an angle-tunable color reflection filter based on a silicon nitride grating, in which the three primary colors are achieved with high reflection efficiencies (Fig. 2.3(b)) using angles of incidence ranging from 8° to 35° [47].

2.2 Biosensing

2.2.1 Targeted biomolecular sensing

As opposed to intentionally inducing refractive index changes in order to tune the resonance spectrum of guided mode resonance filters, the resonance can be used instead to monitor refractive index changes that occur close to the waveguide surface, and hence, can be utilized in sensing applications. Biological sensors (or biosensors, for short) are widely used in the life-science and pharmaceutical industry as well as in medical diagnostics to perform screening of biological agents or chemical substances, and to measure biological interactions and kinetic processes, etc. Traditionally, biosensors have required the use of labels such as fluorescent dyes and radioactive tags, which can be disruptive to the process under investigation, and potentially alter experimental outcomes. For this reason, there has been a significant impetus to develop a new generation of sensors which operate without the need for dying or tagging, where instead, a layer of receptor molecules (ligands) is immobilized on a sensing element via covalent attachment, to which complementary target molecules (analytes) selectively bind in a lock-and-key fashion[3]. The recognition layer may be formed from peptides, proteins, DNA, RNA or small molecules [48], depending on the target analyte. In label-free optical biosensors, binding of analytes to a recognition layer causes a change in refractive index, which is transduced to a change in the output optical signal. The principle advantage of optical biosensors over, say, electrical sensors, is that sensor interrogation is performed without the need for electrical connections which may significantly complicate both fabrication and measurements, especially if the biosensor is part of an array and needs to be addressed individually. As discussed in the introduction, the currently established method for optical label-free biosensing is based on surface plasmon resonance, in which refractive index changes at a metal-dielectric interface cause a change in a monitored optical parameter, such as wavelength or coupling angle [49].

[3]The term functionalization is often used to refer to both the immobilization process, as well as the resulting recognition layer.

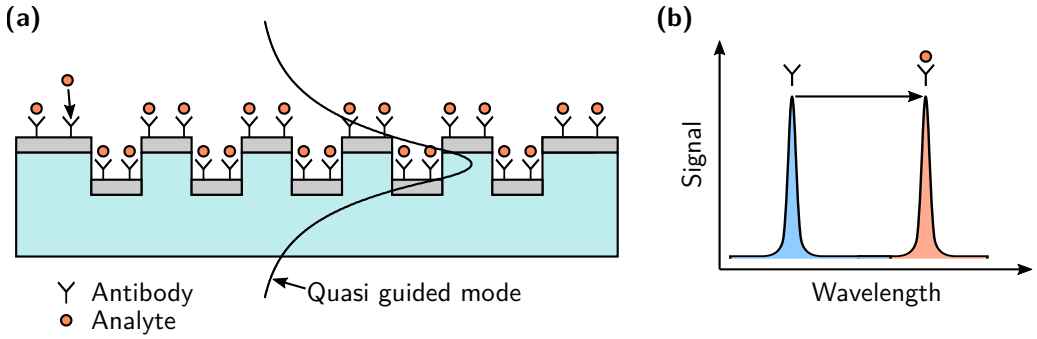

Figure 2.4: (a) A guided mode resonance filter treated with a molecular recognition layer to which target analytes selectively bind. The molecular binding induces a refractive index within the evanescent field of a quasi guided mode supported by the structure, which leads to a change in the exhibited resonance wavelength, as shown in (b).

In the past decade, guided mode resonance filters have made significant inroads into the field of optical label-free biosensing [50, 51], and have been successfully demonstrated in e.g. screening of small molecule and biochemical interactions [48, 52–54], cell-based assays [55], the detection of ovarian [56] and breast cancer [57] biomarkers, and HIV viruses [58].

For biosensing applications, guided mode resonance filter sensors are generally prepared such that a recognition layer is immobilized directly on the high-index waveguide layer, as illustrated in Fig. 2.4(a). Under the illumination of broadband, collimated, and normally incident light, the structure will exhibit resonant reflection at a particular wavelength. However, when an aqueous solution containing target analytes is passed over the surface, they will selectively bind to the receptor molecules and increase the optical density at the surface. This alters the propagation constant of the quasi guided mode, which manifests itself as a wavelength shift of the resonantly reflected light, as illustrated in Fig. 2.4(b). As with conventional dielectric slab waveguides, the electric field of the quasi guided mode takes a maximum within the waveguide core, and then decays exponentially away from it. Thus, GMRF sensors selectively measure refractive index changes that occur within the evanescent decay length of the optical mode, close to the surface. Furthermore, the wavelength shift of the resonant reflection is directly linked to the optical density of the attached analyte, and monitoring the resonance shift as a function of time can be used to quantify binding kinetics. Figure 2.5 shows the results of an experiment carried out to sense the presence of biotin molecules using a GMRF sensor with a recognition layer composed of avidin [52]. As the results demonstrate, the peak wavelength

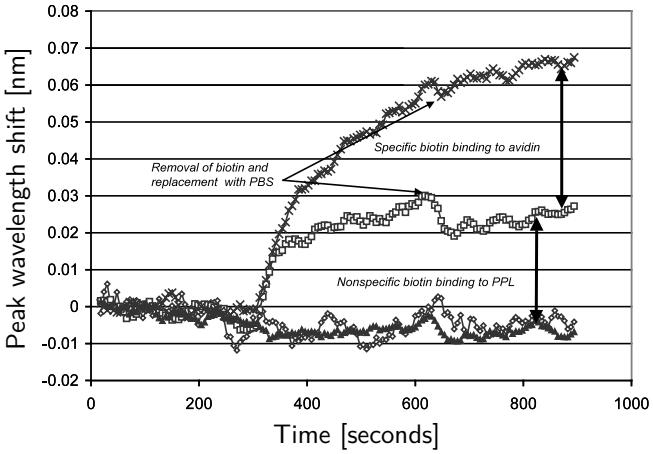

Figure 2.5: Selective biosensing of small biotin molecules by a GMRF surface coated with avidin. PBS refers to phosphate-buffered saline, whereas PPL refers to poly-phe-lysine, which the surface was treated to as part of the functionalization. The topmost curve clearly reveals the presence of biotin. The figure is adapted from [52].

shift due to binding of biotin to the avidin layer is small, but nevertheless clearly discernible. This is to be expected, as biotin molecules are much smaller than avidin, or 244 amu compared to 60.000 amu.

A key challenge faced by optical resonant refractive index sensors is that since refractive indices are not only a function of wavelength but also temperature, signal read-out is susceptible to e.g. thermal drift, optical heating, evaporative cooling, and temperature variations brought on by addition of sample material. In addition to this, molecules may adsorb to the sensor surface, and the background bulk refractive index of the material being sensed may vary. These sources of noise must therefore be either mitigated by e.g. temperature stabilization, or otherwise accounted for by an appropriate choice of signal reference. However, since the reference will inherently be placed some distance away from the sensor, it may experience slightly different, or delayed, temperature fluctuations and refractive index variations, as well as leading to less efficient use of space on the sensor chip. In order to address these issues, GMRF biosensors exhibiting multiple resonances due to both transverse-electric and transverse magnetic modes (Fig. 2.6) have been demonstrated [59, 60]. Instead of measuring the peak resonance wavelength with respect to a reference, the relative peak wavelength difference between two resonances associated with different polarization states is measured, thereby eliminating common-mode sources of error. By back-fitting the results to physical models, refractive index changes due to selective bind-

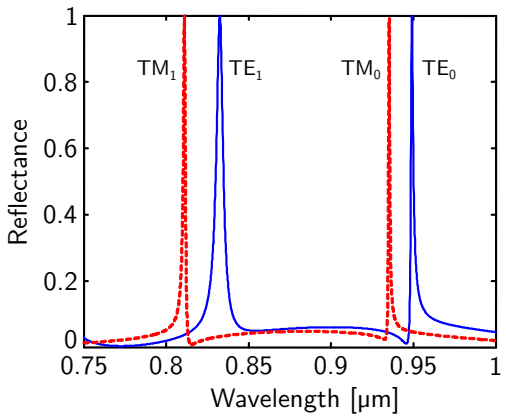

Figure 2.6: Resonance peaks associated with the two lowest order TE and TM polarized quasi guided modes. Instead of measuring a single resonance's peak wavelength with respect to a reference signal originating elsewhere on the sensor, the relative difference between two resonance peaks corresponding to different polarization states emanating from the same location may be used instead. Figure is from [59].

ing may be distinguished from that of temperature effects and background index changes [60]. Additionally, this method can yield more complete information regarding the biological process monitored, such as the thickness of the attached biolayer and its refractive index.

For some low-cost sensing applications, requiring a spectrometer for signal read-out may represent an unacceptable cost-overhead. In such cases, the resonance shift may be measured indirectly by the use of an illumination source whose emission intensity either rises or falls as a function of wavelength in the spectral region in which the guided mode resonance filter operates [61]. Since the GMRF sensor signal is a convolution of a guided mode resonance and the illumination spectrum, a resonance shift will lead to a change in signal intensity, as shown in Fig. 2.7(a). Thus, the signal intensity gives in indirect measure of the resonance shift, and can be measured with an inexpensive photo-diode instead of a spectrometer. This approach requires that GMRF sensors are designed such that they exhibit only a single resonance in the emission spectrum of the illumination source.

For illumination at normal incidence, it can be a challenge to fit both a light source and a signal monitor into the beam-path, and thus, beam-splitting or optical fibers are commonly used [53]. In order to simplify the instrumentation, instead of measuring the resonantly reflected light, the resonance spectra of GMRFs can be obtained in a transmission configuration by placing them at an angle between two orthogonally orientated linear po-

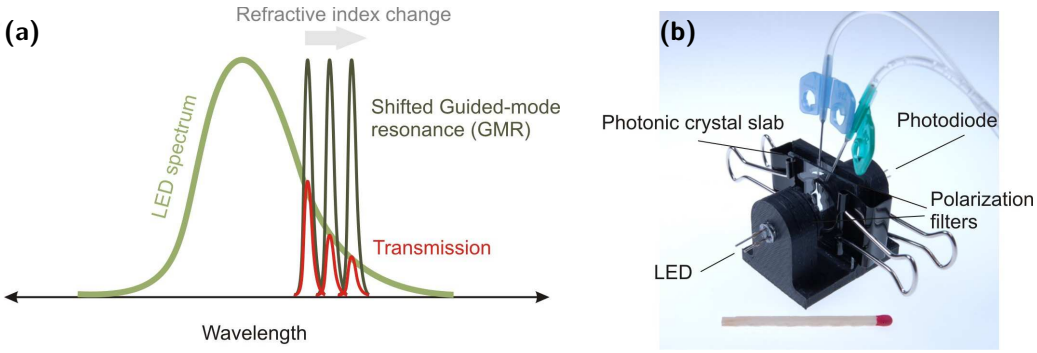

Figure 2.7: (a) Indirect measurement of a peak resonance wavelength shift exhibited by a GMRF sensor, based on an illumination source whose emission intensity monotonously varies in the operating regime of the GMRF. (b) Low-cost biosensing instrumentation consisting of a light-emitting diode, a GMRF placed between two crossed polarizers, and a photo-diode, in which signal read-out is based on measured transmitted intensity instead of spectral peak-tracking. The figure is adapted from [61].

larizers [62, 63], as is discussed in section 4.2.1. This both reduces costs, and allows for a more compact measurement apparatus, albeit at the expense of lower signal intensities and the inability to selectively measure either transverse-electric or transverse-magnetic resonances independently. Figure 2.7(b) shows a complete and compact biosensing system that combines the two cost-saving approaches discussed above, in which sensing is performed using an intensity-based measurement instead of spectral peak tracking, in a transmission configuration.

2.2.2 Quantifying the performance of resonant refractive index sensors

In order to compare the performance of different sensors, one must first establish a suitable figure of merit that characterizes their performance. A commonly used figure of merit to describe resonant refractive index sensors is the sensitivity of the resonance to refractive index changes $s = \Delta\lambda/\Delta n$, i.e. the rate at which the transduced resonance signal shifts with changing refractive index. The disadvantage of relying solely on sensitivity as a figure of merit is that it neglects how precisely a shift in resonance can be measured. In the complete absence of noise and assuming a spectrometer with an infinite resolution, any refractive index change no matter how small can be measured, and the device's sensitivity is enough to describe its performance. In reality however, signal noise and the resolution of the instrumentation will limit how

precisely a resonance shift can be measured. Thus, a more appropriate figure of merit for describing the performance of resonant refractive index sensors is the sensor's so-called detection limit [64]. It quantifies the smallest refractive index change that a sensor can measure and is given by

$$\mathrm{DL} = \frac{R}{s}\ [\mathrm{RIU}] \tag{2.1}$$

where R is the sensor resolution, i.e. the smallest spectral shift in the resonance signal that can be accurately detected. In order to measure spectral shifts, the resonance signals are typically fitted with an appropriate analytical function (e.g. a Lorentzian curve) and a spectral feature such as peak wavelength is tracked. Alternatively, the resonance's center of intensity[4] can be calculated and tracked instead,

$$\lambda_\mathrm{c} = \frac{\sum_{i=n}^{m} \lambda_i I_i}{\sum_{i=n}^{m} I_i} \tag{2.2}$$

where I_i is the measured intensity at wavelength λ_i in spectral position i, and the integers n and m are chosen such that the calculation encompasses the resonance peak only. This approach can be more suitable for e.g. asymmetric line-shapes or resonances which are not well described by analytical functions, and is computationally simple and less time consuming than fitting. Due to noise, the wavelength location of the tracked spectral feature will exhibit statistical variation, and the sensor's resolution is commonly taken as being three standard deviations of this wavelength variation, $R = 3\sigma$. All things being equal, the lower the resonance linewidth, i.e. the higher the quality factor Q, the better the sensor's resolution. Thus, during the theoretical design phase of a refractive index sensor, an reasonable figure of merit to optimize is $s \times Q$.

2.2.3 Laser biosensors

Generally, there exists a trade-off relationship between the sensitivity and quality factor, i.e. enhancing one leads to a reduction of the other. Thus, for a given set of refractive indices comprising the sensor, its geometrical parameters must be engineered to yield the optimum figure of merit. However, an inventive method for circumnavigating this issue has been devised, and involves utilizing guided mode resonance filters simultaneously for line-narrowing a laser, and as a refractive index transducer element [65]. This way, the output signal is in the form of laser emission with its associated high

[4] corresponding to the center of mass of an object

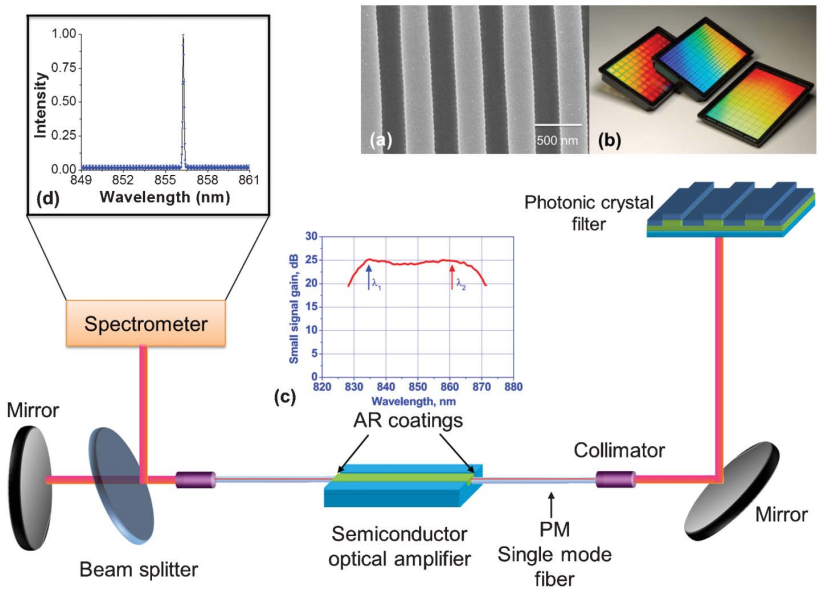

Figure 2.8: An external cavity laser biosensor in which a guided mode resonance filter simultaneously serves as a sensor surface and a wavelength-selective mirror. (a) A scanning electron micrograph of the GMRF surface, (b) a photograph of the GMRF, (c) the gain spectrum of the semiconductor optical amplifier, and (d) an example of the emission spectrum. Figure is from Ref. [65]

Q-factor, while retaining the sensitivity of a guided mode resonance filter. Such an external cavity laser biosensor is shown in Fig. 2.8.

Essentially, this sensor is a solid state laser, in which one of the mirrors that provides optical feedback is a guided mode resonance filter sensor. The GMRF behaves as a wavelength-selective mirror with the reflected wavelength peak corresponding the the density of biomaterial attached to its surface. The optical gain is provided by a semiconductor optical amplifier, and the GMRF is designed such that its resonant reflection when exposed to aqueous solutions (i.e. refractive index conditions close to that in which biological sensing takes place) coincides with the gain spectrum of the amplifier. Sensor read-out is achieved by siphoning off a small fraction of the light from the beam path and directing it to a spectrometer. This enhances the Q factor of the read-out signal compared to that of the passive GMRF by a factor of $> 10^4$, thus improving the sensor's detection limit [65].

In addition to improving the quality factor, the detection limit can improved further by enhancing the device sensitivity. Periodically structured metal films have been shown to exhibit a wavelength filtering response reminiscent of guided mode resonances known as extraordinary optical transmis-

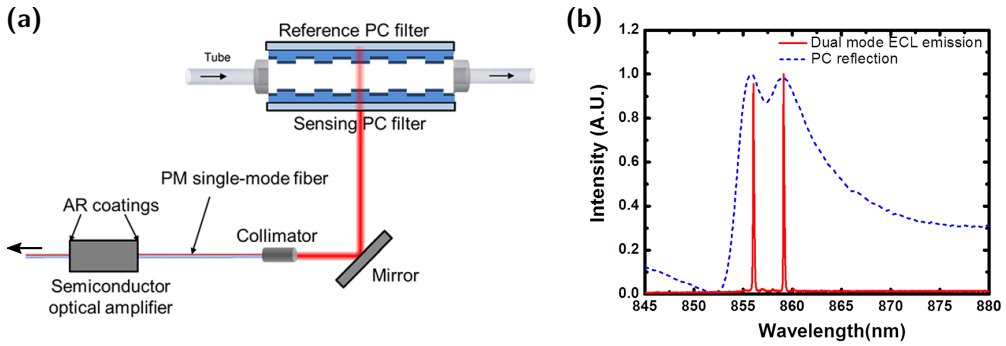

Figure 2.9: (a) The same external cavity laser biosensor as in Fig. 2.8, but to which a secondary reference sensor has been added, and the two GMRFs constitute the inward-facing walls of a flow-cell. (b) The recorded laser emission spectra from this dual-sensor setup, superimposed on the passive GMRF resonant reflection. Figure is adapted from Ref. [70].

sion [66–68]. Furthermore, metal films exhibit high sensitivities to refractive index changes due to their strong light-matter interaction [49]. Replacing the high-index dielectric of a guided mode resonance filter with a thin metal film produces its plasmonic counterpart, known as a plasmonic crystal. Although they exhibit the high refractive index sensitivity inherent to metallic structures, they also produce resonances with considerably larger linewidths than GMRFs. However, when used simultaneously as a sensor and a wavelength selective mirror in an external cavity laser, the issue of linewidth is sidestepped as before, producing a refractive index sensor with the sensitivity of a metal, yet the linewidth of a laser [69].

Now, returning back to conventional guided mode resonance filters, the main disadvantage of employing them in external laser cavity biosensors as described is the lack of a reference signal. Since the laser sensor can only probe a single position on the GMRF at a time, a secondary guided mode resonance filter must be added [70]. The reference should either be non-functionalized or treated with an adsorption blocking layer, and made from identical materials and periodicity. However, in order to compensate for the lack of functionalizing biomolecules at the surface, the high-index layer should be slightly thicker to ensure that the wavelength-separation between reference and sensor signals is small, with the reference occurring at slightly shorter wavelengths. The two GMRF surfaces can be fashioned such that they constitute the inward facing walls of a flow cell, as shown in Fig. 2.9(a). By taking this approach, two laser signal peaks are recorded, one corresponding to the non-functionalized reference, and the other to the functionalized sensor, as shown in Fig. 2.9(b). Now, instead of measuring the peak wave-

length with respect to its position at the start of the sensing procedure, it is the wavelength difference between the two peaks that is of interest. The advantage of this approach is that by constituting part of a flow-cell, the two sensor surfaces are exposed simultaneously and equally to e.g. temperature and bulk refractive index variations, and the sensor can thus be referred to as being self-referencing [70].

An alternative to the external cavity laser approach is to introduce a gain medium into the GMRF structure itself, essentially transforming it into a distributed feedback (DFB) laser sensor. DFB laser sensors composed of a dye-doped periodically nanostructured polymer covered with a high-index layer produce narrow-linewidth laser emission when optically pumped with a pulsed laser. As with conventional guided mode resonance filters, the peak wavelength of the emission is highly sensitive to refractive index changes at the device surface [71], and due to the narrow emission linewidth, they can achieve very low detection limits [72]. An additional advantage of these structures is that they are capable of fast time-resolved refractive index sensing, limited primarily by the pumping frequency, and the instrumentation used for spectral analysis [73]. Unfortunately, such dye laser sensors have limited lifetimes as the dye molecules eventually undergo a permanent photochemical change known as bleaching. This causes a drop in emission intensity and a change in emission wavelength, or even complete cessation of light emission. Furthermore, the optical pump source is expensive, and is thus a significant hindrance for low-cost applications. A high index layer is not an inherent requirement for the operation of DFB laser sensors [74], however they do increase their sensitivity [72], and can further be used as transduction elements [75].

2.2.4 Surface imaging

Similarly to biomolecular sensing, microscopy of living cells typically involves selective dying or staining of cell components or the attachment of fluorescent tracker molecules. These molecules eventually bleach, and their presence is cytotoxic, prohibiting the monitoring of cellular processes over long periods of time, as well as being otherwise disruptive. There is thus a clear demand for label-free microscopy and surface imaging methods, in regards to which guided mode resonance filters have shown promising results. One such method is photonic crystal enhanced microscopy, in which refractive index variations over the surface of a GMRF sensor can be used to add contrast to conventional microscope images [76]. The greater the concentration of biomaterial within the evanescent field of resonant light within a GMRF, the greater the shift in peak resonance wavelength of the transduced signal em-

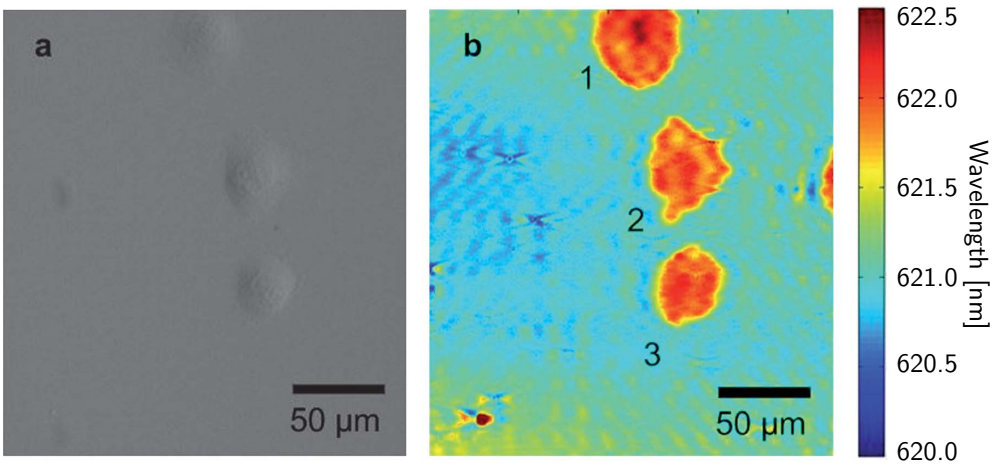

Figure 2.10: (a) A bright-field image of human pancreatic cancer cells and (b) a peak-wavelength image of the same, illustrating the contrast enhancement by the photonic crystal enhanced microscopy method. Figure is from Ref. [77]

anating from that particular region. By focusing an image of the resonantly reflected light onto the slit of an imaging spectrometer, the peak wavelengths along a single line of the image (corresponding to the light passing through the slit) can be automatically obtained. Then, by scanning the sample laterally with a motorized stage, a full two-dimensional image of the wavelength peaks can be constructed with a sub-micron spatial resolution [77]. Figure 2.10 shows a comparison of a bright field image and a peak wavelength image of several human pancreatic cancer cells on a GMRF surface.

Because of the time required to determine the peak wavelength for each pixel and stage scanning, it takes approximately 10 seconds to generate such a full 2D image. The method can therefore not capture time-lapse images in real-time, but is still fast enough to monitor many interesting biological processes, such as cellular responses to chemical stimuli, division and apoptosis. While still an inherently in-vitro[5] method, the lack of staining, fluorescent molecules, etc, mimics the natural conditions of cells more closely and thus offers the potential for obtaining results more representative of in-vivo conditions[6].

For cells and other objects that lie within the evanescent decay length of the quasi guided modes, the scanning-imaging technique of peak resonance wavelengths can be used to perform non-contact, three-dimensional topo-

[5]A term originating from Latin that refers to the study of cells or biological molecules in a setting different from that in which they occur naturally.

[6]Latin for, "in the living".

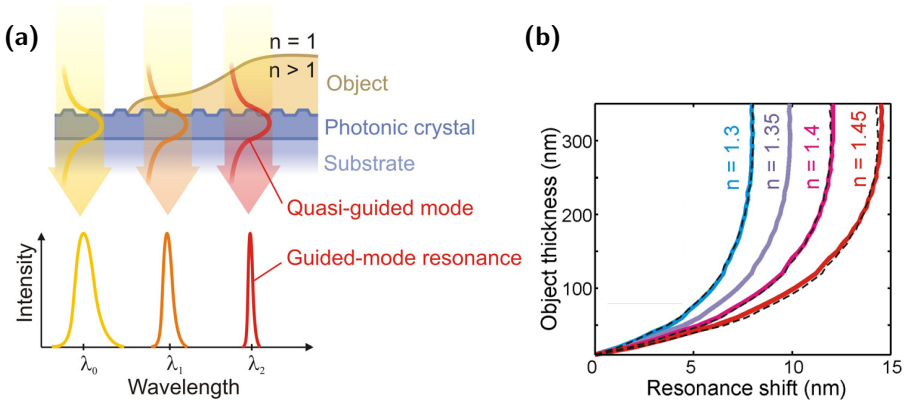

Figure 2.11: (a) An illustration of how the thickness of an object on the surface of a guided mode resonance filter influences both the peak resonance wavelength as well as the resonance quality factor. (b) Calibration curves that relate the thickness of objects to observed spectral resonance shifts for several different object refractive indices. The figure is adapted from Ref. [78]

graphical imaging of the object's upper surface [78]. For an object fulfilling this thickness criterion, its thickness influences both the peak resonance wavelength and its quality factor, as illustrated in Fig. 2.11(a). For a given uniform refractive index of the object, there is a unique, non-linear relationship between the object's thickness and the peak resonance wavelength shift it causes, as shown in Fig. 2.11(b). Thus, by combining this information with measurements of the spectral peak resonance wavelengths as a function of position using an image spectrometer and stage-scanning, a three-dimensional

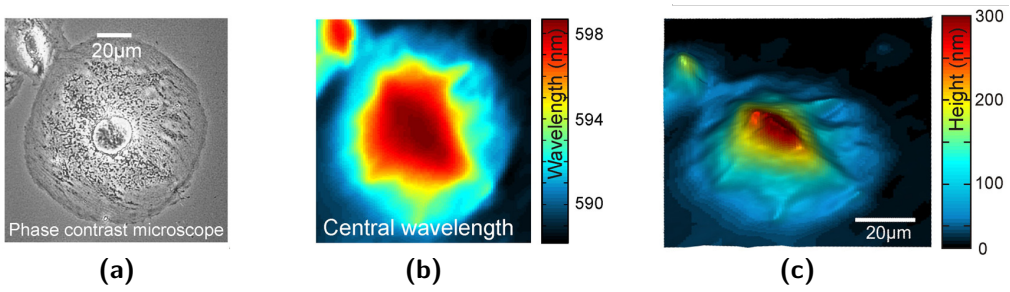

Figure 2.12: (a) A two-dimensional microscope image of a rat embryonic fibroblast cell attached to a guide mode resonance filter surface. (b) A peak wavelength image of the same cell, obtained using an imaging spectrometer and stage-scanning. (c) A three-dimensional topographical image of the cell's surface, obtained from the peak wavelength image and a calibration curve. The figure is adapted from Ref. [78].

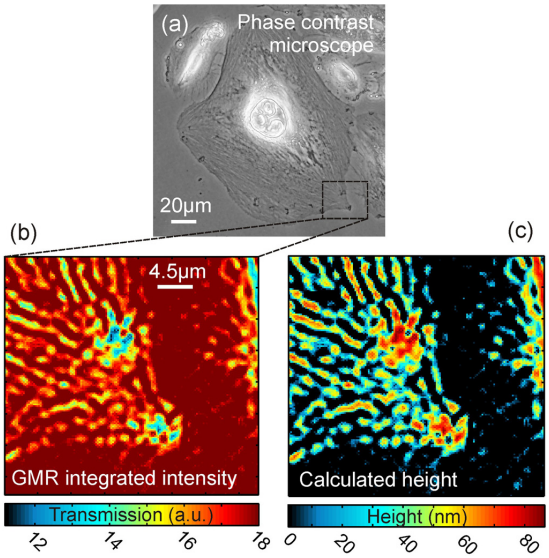

Figure 2.13: (a) A microscope image of a cell. (b) An intensity image of a portion of the same cell, obtained with a camera. (c) The resulting topographical image obtained by means of an intensity-height calibration curve. The figure is from Ref. [78].

image of the object's topography can be obtained. Figure 2.12 shows such an image for the case of an rat embryonic fibroblast cell attached to a guided mode resonance filter surface. The validity of the assumption regarding the cell's average refractive index was confirmed by comparison with measurements obtained by atomic force microscopy. Such topographical imaging cannot be obtained using conventional two-dimensional microscopy, and this method is furthermore considerably faster than atomic force microscopy, as well as being capable of imaging much larger areas. For the imaging of thicker objects, the evanescent decay length of the quasi guided mode can be engineered to an extent by the appropriate choice of high refractive index layer material and its thickness.

Due to this method's reliance on spectral imaging, it is not a real time method. However, as mentioned before, the thickness of the imaging subject also directly influences the quality factor of the resonances. Moreover, the quality factor is directly related to the brightness or intensity of resonant light emanating from a particular region, and hence the height of an object at a given location can be obtained from the observed brightness. Thus, a gray-scale image of the object can be transformed into a three-dimensional surface height image by use of a calibration curve, as shown in Fig. 2.13. The advantage of this method is that since it doesn't rely on obtaining spectral

resonance wavelengths, scanning is no longer needed and thus an entire image of an object's height can be obtained simultaneously, in real-time.

Real time peak wavelength (shift) imaging has further been demonstrated using distributed feedback dye lasers without the use of stage-scanning. In this method, the DFB laser is composed of multiple grating regions of varying periods, all in parallel with each other. Each of these regions produces laser emission at a different wavelength, and thus light emanating from a particular spatial position can be identified by its spectral position alone. By collecting the laser emission produced by all the regions simultaneously and focusing it into an imaging spectrometer using a cylindrical lens, the recorded wavelength shifts of each peak can be used to construct a two-dimensional image. The spatial position in one coordinate is given by the spatial position on the spectrometer CCD, and the spatial position in the other coordinate is given by the spectral position of the emission peak. This method has been shown to be capable of producing images of refractive index changes quickly (12 Hz) without any moving parts [79].

3 | Theoretical background

This chapter provides an introduction to the theoretical background describing guided mode resonance filters. The discussion starts with conventional, un-modulated dielectric slab waveguides with cores of constant refractive index. Then, it is shown that by introducing a refractive index modulation to the waveguide core, its guided modes can couple to externally propagating light, which results in the structure exhibiting resonant reflection when illuminated with out-of-plane incident light. After that, an alternate form of modulated waveguide is considered, in which the thickness of the core varies periodically in the guiding direction, and exhibits anologous resonant behavior.

3.1 Dielectric slab waveguides

The phenomenon of optical waveguiding is arguably most readily understood with respect to a dielectric slab waveguide, shown in Fig. 3.1. It is a three-layer device, composed of a thin waveguide core of thickness t and refractive index n_2, clad in two semi-infinite layers of refractive indices n_3, n_1. These are referred to as the substrate and superstrate, respectively, and referred to collectively as the waveguide cladding. If the refractive index of the waveguide core is higher than that of the cladding, $n_2 > n_1, n_3$, the structure is able to sustain a guided mode that propagates along the x-axis (c.f. total internal reflection). The following analysis of the slab waveguide follows that of Yariv [80] and Maier [81].

For systems composed of linear and isotropic media, with no free charges and no free currents, carrying light with an angular frequency ω and a har-

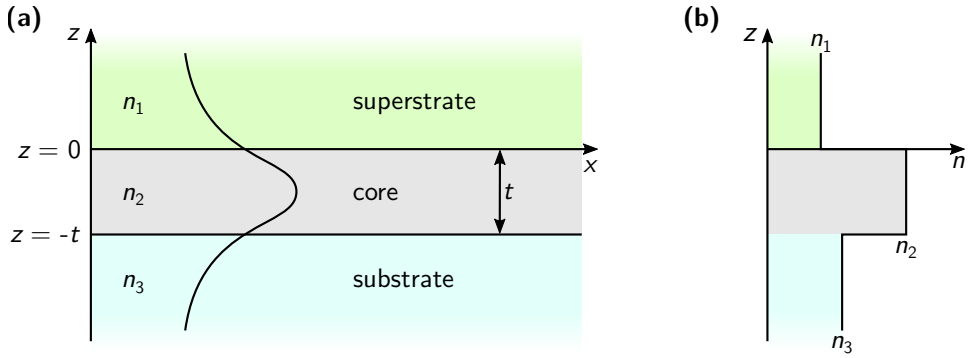

Figure 3.1: (a) Schematic illustration of an asymmetric ($n_1 \neq n_3$) slab waveguide carrying a bound mode. (b) The refractive index profile of an asymmetric slab waveguide, for the case where $n_1 < n_3 < n_2$.

monic time dependence of the form $e^{i\omega t}$, Maxwell's equations are as follows:

$$\nabla \cdot \mathbf{E} = 0 \tag{3.1}$$
$$\nabla \cdot \mathbf{B} = 0 \tag{3.2}$$
$$\nabla \times \mathbf{E} = -i\omega\mathbf{B} \tag{3.3}$$
$$\nabla \times \mathbf{B} = i\omega\mu\epsilon\mathbf{E} \tag{3.4}$$

where $\mathbf{E}$ is the electric field, $\mathbf{B}$ is the magnetic field, and ϵ and μ are the permittivity and permeability of the material in which the light propagates, respectively. These quantities are related to the refractive index of the material n via the following:

$$\epsilon = \epsilon_r\epsilon_0, \quad \mu = \mu_r\mu_0, \quad n^2 = \epsilon_r\mu_r \tag{3.5}$$

where ϵ_r and μ_r are the material's relative permittivity and permeability, and ϵ_0 and μ_0 are the vacuum permittivity and permeability. Throughout this chapter, non-magnetic materials will be assumed, $\mu_r = 1$. Due to the lack of spatial variation in the y-coordinate, and the homogeneity in the x-direction, we look for solutions to Eqs. (3.3) and (3.4) of the form:

$$\mathbf{E}(\mathbf{r}, t) = E_m(z)\exp\left[i(\omega t - \beta x)\right] \tag{3.6}$$
$$\mathbf{B}(\mathbf{r}, t) = B_m(z)\exp\left[i(\omega t - \beta x)\right] \tag{3.7}$$

where $\mathbf{r}$ is the position vector, $E_m(z)$ and $B_m(z)$ are the wavefunctions of the guided mode and m is an integer denoting the mode number. Furthermore, β is the propagation constant of the guided mode, and corresponds to the x-component its wave vector, $\mathbf{k}$. Thus, for the present system: $\frac{\partial}{\partial y} \to 0$

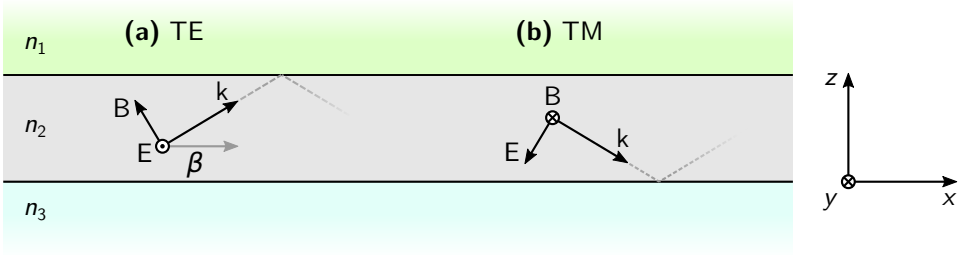

Figure 3.2: Directions of the electric and magnetic fields of a propagating mode for the cases of (a) transverse-electric, and (b) transverse-magnetic polarization.

and $\frac{\partial}{\partial x} \to -i\beta$. Applying these two conditions to Maxwell's curl equations yields two sets of equations, the solutions of which correspond to propagating waves with different polarization properties [81]. One set describes transverse-electric (TE, or s) modes, in which the only non-zero field components are E_y, B_x, and B_z, and the other set describes transverse-magnetic (TM, or p) modes, in which the only non-zero field components are B_y, E_x, and E_z, as illustrated in Fig. 3.2. The two sets of equations are as follows:

TE:		TM:	
$\frac{\partial^2 E_y}{\partial z^2} + (k_0^2 n^2 - \beta^2) E_y = 0$	(3.8)	$\frac{\partial^2 B_y}{\partial z^2} + (k_0^2 n^2 - \beta^2) B_y = 0$	(3.11)
$B_x = -\frac{i}{\omega} \frac{\partial E_y}{\partial z}$	(3.9)	$E_x = i \frac{1}{\omega \mu \epsilon} \frac{\partial B_y}{\partial z}$	(3.12)
$B_z = \frac{\beta}{\omega} E_y$	(3.10)	$E_z = -\frac{\beta}{\omega \mu \epsilon} B_y$	(3.13)

where $k_0 = 2\pi/\lambda$ is the vacuum wavenumber and λ is the free space wavelength of the light. Equations (3.8) and (3.11) are known as the TE, and TM wave equations, respectively[1].

3.1.1 Transverse-electric modes

In transverse-electric modes, the electric field is perpendicular to the plane of incidence, i.e. it only has a non-zero electric field component in the y-direction, and is thus of the form

$$E_y(\mathbf{r}, t) = E_m(z) \exp\left[i(\omega t - \beta x)\right] \tag{3.14}$$

[1]Here, we have made use of the following relations: $k_0 = \omega/c$ and $1/c^2 = \epsilon_0 \mu_0$, where c is the speed of light in vacuum.

By solving the TE wave equation (3.8) for each of the three layers, looking for solutions that vanish at $z = \pm\infty$, and then applying the boundary conditions that E_y and B_x must be continuous across the two material interfaces at $z = 0$, and $z = -t$, yields the wavefunction of the mode $E_m(z)$:

$$E_m(z) = C \begin{cases} \exp(-qz) & 0 \leq z \\ \cos(hz) - \dfrac{q}{h}\sin(hz) & -t \leq z \leq 0 \\ \left[\cos(ht) + \dfrac{q}{h}\sin(ht)\right]\exp(p(z+t)) & z \leq -t \end{cases} \tag{3.15}$$

where t is the thickness of the waveguide core, C is a constant, and

$$q = \left[\beta^2 - n_1^2 k_0^2\right]^{1/2} \tag{3.16}$$

$$h = \left[n_2^2 k_0^2 - \beta^2\right]^{1/2} \tag{3.17}$$

$$p = \left[\beta^2 - n_3^2 k_0^2\right]^{1/2} \tag{3.18}$$

The wavefunction thus has an oscillatory form in the waveguide core, and decays exponentially away from the two material interfaces. A further consequence of the application of the boundary conditions is the following transcendental equation

$$\tan(ht) = \frac{p+q}{h(1-pq/h^2)} \tag{3.19}$$

known as the mode condition, which the propagation constant β of TE-polarized guided modes must satisfy. Calculating the allowed modes for a particular slab waveguide structure thus involves the following steps: Given the material parameters n_{1-3}, geometric parameter t, and the wavelength of light λ, the mode condition is numerically solved for the propagation constant β. This will yield a finite number of solutions, and at least one if the refractive index contrast between the core and cladding, and thickness t are large enough. Each solution for β corresponds to a particular mode, with the shape of the electric field in the waveguide given by Eq. (3.15).

3.1.2 Transverse-magnetic modes

For the case of transverse-magnetic modes, it is the magnetic field that is perpendicular to the plane of incidence (i.e. in the y-direction), while the electric field components E_x and E_z lie in the plane of incidence. Hence, B_y is of the form

$$B_y(\mathbf{r}, t) = B_m(z)\exp\left[i(\omega t - \beta x)\right] \tag{3.20}$$

Analogously to before, solving the TM wave equation (3.11) for the three layers and applying the boundary conditions that B_y and E_x must be continuous across the two material interfaces, yields the following solution for $B_m(z)$

$$B_m(z) = C \begin{cases} \frac{h}{\bar{q}} \exp(-qz) & 0 \leq z \\ \frac{h}{\bar{q}} \cos(hz) - \sin(hz) & -t \leq z \leq 0 \\ \left[\frac{h}{\bar{q}} \cos(ht) + \sin(ht)\right] \exp(p(z+t)) & z \leq -t \end{cases} \tag{3.21}$$

where

$$\bar{p} \equiv \frac{n_2^2}{n_3^2} p \tag{3.22}$$

$$\bar{q} \equiv \frac{n_2^2}{n_1^2} q \tag{3.23}$$

As before, this process yields a mode condition that β must satisfy, given by

$$\tan(ht) = \frac{h(\bar{p} + \bar{q})}{h^2 - \bar{p}\bar{q}} \tag{3.24}$$

3.1.3 Guided modes in a polymer-TiO_2 slab waveguide

In the following, a slab waveguide composed of a low refractive index polymer substrate (Efiron PC-409), a titanium dioxide (TiO_2) waveguide core, and either an air or water superstrate, is investigated. This structure mirrors that of a guided mode resonance filter configuration commonly used in this thesis work, where instead of the waveguide core being a single, continuous layer, its z-coordinate is periodically varied, as shown in Fig. 1.1.

Having established the governing equations of guided modes in slab waveguides, we are ready to proceed with the analysis. The first step in understanding the behavior of a particular slab waveguide structure is to learn at which core thicknesses t it becomes waveguiding, in which regime it operates as a single-mode waveguide, etc. Figure 3.3 shows the propagation constant β of both TE and TM modes as a function of core thickness t for the polymer-TiO_2 slab waveguide structure in question, obtained by numerically solving Eq. (3.19) and (3.24). Here, the propagation constant is expressed using a

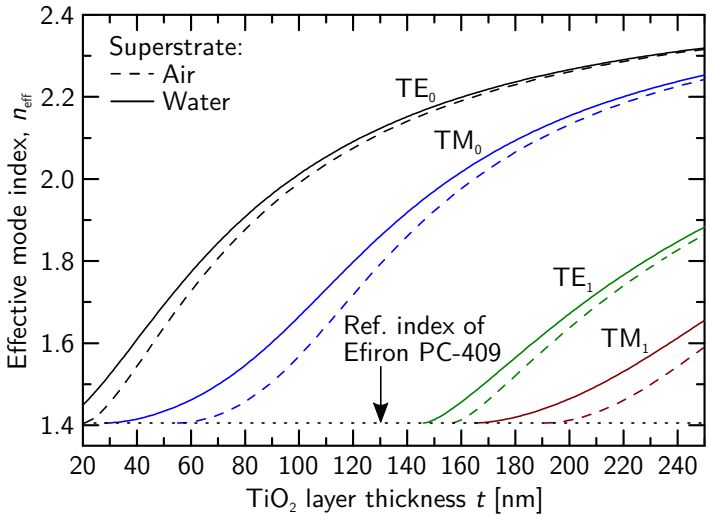

Figure 3.3: The effective mode index as a function of waveguide core thickness t for a slab waveguide composed of a polymer substrate (Efiron PC-409) ($n_3 = 1.405$), a titanium dioxde waveguide core ($n_2 = 2.458$), and either air ($n_1 = 1.0$) or water ($n_1 = 1.335$) as the superstrate, at a wavelength of $\lambda = 550$ nm.

more intuitive quantity known as the effective mode index n_{eff}

$$n_{\text{eff}} = \frac{\beta}{k_0} \tag{3.25}$$

that is, the propagation constant normalized to the vacuum wavenumber. The effective mode index is a dimensionless constant with values in the range $\max\{n_1, n_3\} < n_{\text{eff}} < n_2$. As shown in Fig. 3.3, the structure becomes waveguiding for TiO_2 thicknesses of the order of $t = 20$ nm, with the onset of TE modes occuring sooner than for TM modes. The device remains single mode for thicknesses of up to $t = 140$ nm, but for greater thicknesses, more modes become available, and the device enters multimode operation.

Figure 3.4 shows the wavefunctions for the fundamental TE and TM guided modes ($m = 0$) for several waveguide thicknesses t, as given by Eqs. (3.15) and (3.21). The general behaviour is that as the waveguide core thickness increases, the more the mode becomes confined to the core. The distance which the eletromagnetic field of a mode extends into the superstrate is an important factor for sensing applications, as it determines how far into a sample material it probes. The mode confinement is quantified by the evanescent decay length $\hat{e}$, defined the distane from the waveguide core at which the field amplitude has decreased to a fraction of $1/e$ of its amplitude at the surface.

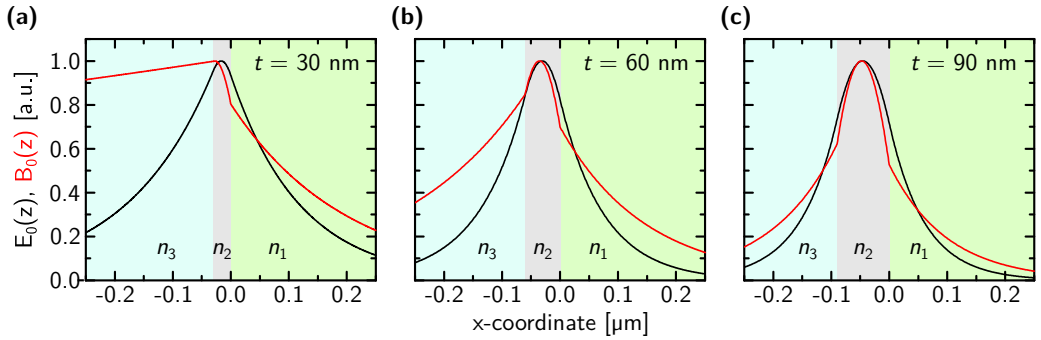

Figure 3.4: The wavefunctions of the fundamental TE and TM modes for a polymer-TiO_2 slab waveguide with a water superstrate, at a wavelength of $\lambda = 550$ nm.

Comparison with Eqs. (3.15) and (3.21) yields that $\hat{e} = 1/q$, or

$$\hat{e} = \frac{\lambda}{2\pi}\left[n_{\text{eff}}^2 - n_1^2\right]^{-1/2} \tag{3.26}$$

Figure 3.5 shows the evanescent decay length of the fundamental TE and TM modes of the polymer-TiO_2-water slab waveguide structure as a function of waveguide thickness t. As illustrated by the figure, the decay length decreases monotonously as a function of thickness t for both modes, with the TE

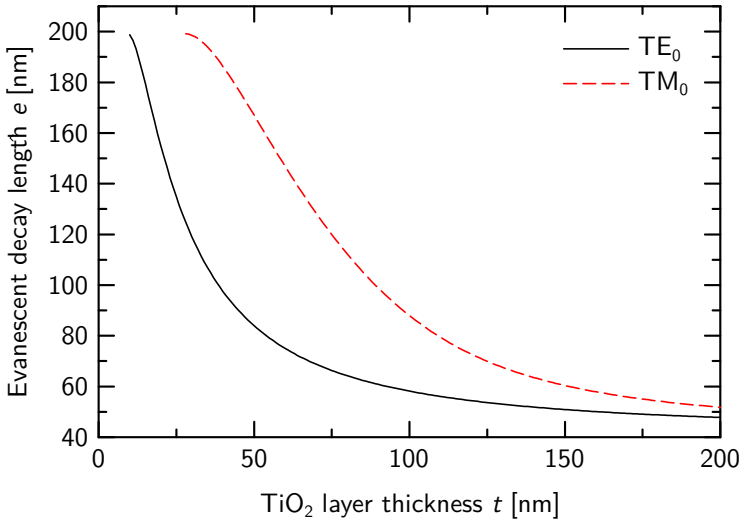

Figure 3.5: The evanescent decay length $\hat{e}$ as a function of waveguide core thickness t for the fundamental TE and TM modes for a polymer-TiO_2 slab waveguide with a water superstrate, at a wavelength of $\lambda = 550$ nm.

mode generally exhibiting greater confinement than the TM mode for a given thickness.

As a final remark, the guided modes sustained by these slab waveguide structures have no coupling to externally propagating light. Thus, barring any material losses or scattering, the photons in these modes will have infinite lifetimes. However, as will be shown in the following sections, by introducing a periodic perturbation to the waveguide structure, the guided modes will start to couple to the far field, and as a result, the photon lifetimes will become finite.

3.2 Dielectric slab waveguides with periodically modulated cores

3.2.1 A brief introduction to diffraction gratings

When a plane wave of monochromatic light of wavelength λ is incident at an angle θ' on a periodically corrigated material interface of period Λ, instead of just being refracted and reflected as with a flat surface, it is also diffracted into several waves of light travelling in different directions, known as diffraction orders (Fig. 3.6). Such structures are known as diffraction gratings, and diffract light in both the backward-diffracted (reflected) and forward-diffracted (transmitted) directions. The angle of diffraction of re-

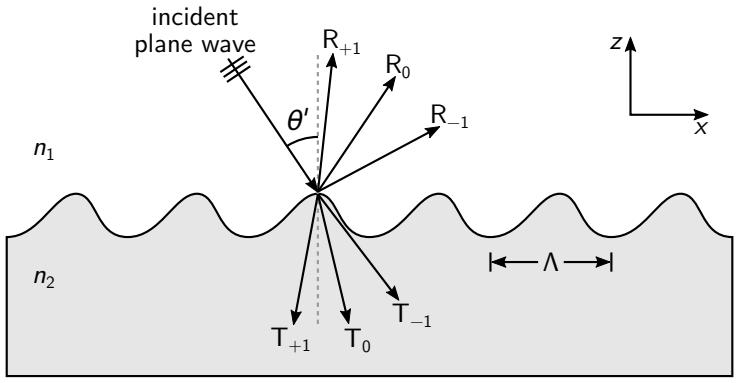

Figure 3.6: A plane-wave of monochromatic light incident on an arbitrarily corrugated material interface with period Λ, known as a diffraction grating. The grating causes the light to be diffracted in several directions in both the reflected and transmitted directions. Here, R_m refers to the mth diffracted order in the reflected direction $+z$, whereas T_m refers to the mth diffracted order in the transmitted direction $-z$.

flected order m as measured with respect to the surface normal θ_m is given by:

$$n_1 \sin\theta_m - n_1 \sin\theta' = \frac{m\lambda}{\Lambda}, \quad m \in \mathbb{Z} \tag{3.27}$$

where n_1 is the refractive index of the medium carrying the incident light. For the case of transmitted orders, θ_m is given by:

$$n_2 \sin\theta_m - n_1 \sin\theta' = \frac{m\lambda}{\Lambda}, \quad m \in \mathbb{Z} \tag{3.28}$$

where n_2 is the refractive index of the corrugated medium [82]. Diffraction orders are classified as being either propagating or evanescent, depending on whether they tend towards $z \to \pm\infty$ or not. For propagating diffraction orders to exist, θ_m must be a real number. However, for increasing values of $|m|$, there comes a point where Eqs. (3.27) and (3.28) no longer yield real values of θ_m, but rather complex solutions of the form $\theta_m = (90 + \alpha i)^\circ$, where α is a real number. Such solutions correspond to evanescent diffraction orders, which propagate along the x-axis in the vicinity of the grating surface and decay exponentially in the propagation direction.

For a given grating structure and incident wave, only a finite number of propagating diffraction orders can exist, as opposed to an infinite number of evanescent orders. When only the $m = 0$ diffraction orders propagate, with all others being evanescent, or cut-off, the grating is referred to as being a zero-order grating. This requires that:

$$\frac{\Lambda}{\lambda} < \frac{1}{\max\left[n_1, n_2\right] + n_1 \sin\theta'_{\max}} \tag{3.29}$$

where $\theta'_{\max}$ is the maximum angle of incidence at which the grating is to operate [82]. Now, since the denominator of the right side of Eq. (3.29) must always be greater than 1, it is clear that zero-order-only operation requires that the grating period be smaller than the wavelength of the incident light $\Lambda < \lambda$. Such gratings are thus referred to as being subwavelength in nature. Furthermore, for the case of $m = 0$, inspection of Eq. (3.27) yields that $\theta_0 = \theta'$, i.e. the zeroth reflected order propagates in the specular reflection direction, whereas for the case of transmitted orders, substitution of $m = 0$ in Eq. (3.28) reduces it to Snell's law:

$$n_1 \sin\theta' = n_2 \sin\theta_0 \tag{3.30}$$

Hence, the zeroth transmitted diffracted order propagates in the same direction as a wave refracted by an uncorrugated surface. The zeroth reflected

order will always exist, as will the zeroth transmitted order, barring total internal reflection.

Finally, an important paramater describing the behavior of diffraction gratings is the so-called diffraction efficiency. The diffraction efficiency is defined as the fraction of the optical power in order m propagating in medium j with respect to the input power, DE_{jm}. Thus, by this definition, for the case of lossless systems, the following must hold true

$$\sum_{j,m} DE_{jm} = 1 \tag{3.31}$$

3.2.2 Slab waveguides with periodically modulated core indices

Now, turning our attention back to waveguide structures, consider a slab waveguide analogous to the one dicussed previously, where instead of the refractive index of the waveguide core being constant, it varies periodically in the guiding direction with a period of Λ, stated in terms of relative permittivity as:

$$\epsilon_2(x) = \epsilon_a + \Delta\epsilon \cos Kx \tag{3.32}$$

where ϵ_a is the average relative permittivity of the core layer, $\Delta\epsilon$ is the modulation amplitude, and $K = 2\pi/\Lambda$. If the average permittivity of the core is greater than that of the cladding $\epsilon_a > \epsilon_1, \epsilon_2$, the structure is referred to as being a grating waveguide, and is capable of both diffracting and guiding light. Figure 3.7 shows a schematic illustration of the structure in question, in which a monochromatic plane wave with wave vector $\mathbf{k}_1$ impinges on the core of thickness t at incident angle of θ', and is diffracted in both the backward and forward directions.

Now, since the refractive index of the waveguide core is no longer homogenous in the guiding direction (i.e. along the x-axis), we can no longer make the same assumptions regarding the form of the electric and magnetic fields that were made earlier, and thus the previously derived wave equations no longer hold. We must therefore resort to the more general form of the wave-equation, which is obtained by applying the vector identity

$$\nabla\times\nabla\times\mathbf{A} = \nabla(\nabla\cdot\mathbf{A}) - \nabla^2\mathbf{A} \tag{3.33}$$

to Maxwell's equations (3.1)-(3.4), to yield:

$$\nabla^2\mathbf{E} + k_0^2\epsilon_r\mathbf{E} = 0 \tag{3.34}$$

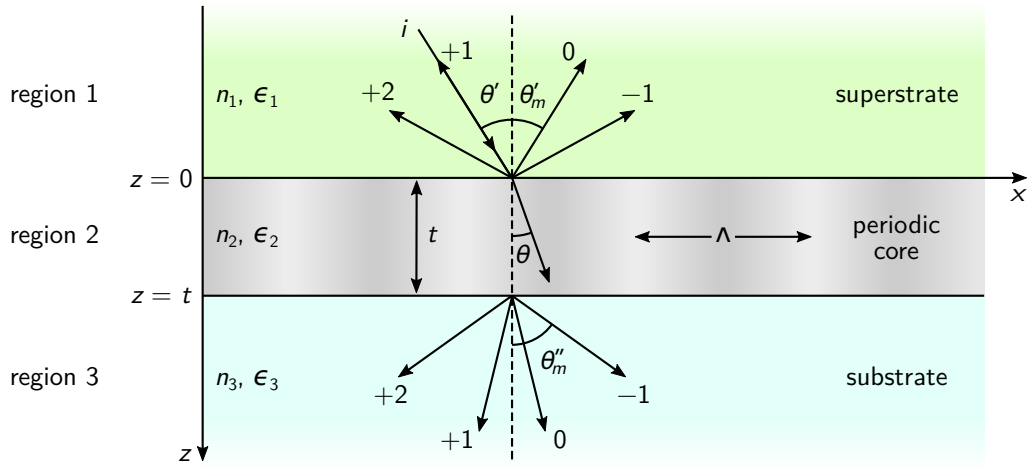

Figure 3.7: (a) Schematic illustration of an asymmetric slab waveguide in which the refractive index of the core varies periodically in the guiding direction, leading to diffraction of an incident monochromatic plane wave in both the backward and forward directions.

also known as the Helmholtz equation. For the case of TE-polarized light, the wave equation for the electric field inside the core, $E_{y,2}$, becomes

$$\nabla^2 E_{y,2}(x,z) + k_0^2 \epsilon_2(x) E_{y,2}(x,z) = 0 \tag{3.35}$$

Solving this equation is a significantly greater challange than for the case of an un-modulated waveguide, and requires more advanced approaches. One popular method for treating such periodic structures is rigorous coupled wave analysis (RCWA) [83], in which Maxwell's equations are solved in Fourier space and fields are represented as infinite sums of space-harmonic fields[2]. In the following, the main results of the works of Gaylord & Moharam et al. [19, 20, 83–85], and Wang & Magnusson, et al. [13–17] in applying RCWA to the present structure are summarized for the case of TE polarized light.

In the RCWA approach, the total electric field inside the grating region (i.e. waveguide core) is expressed as a Fourier expansion in terms of space harmonic fields (inhomogenous plane waves) propagating along the x axis with wave vectors σ_m [85]:

$$E_{y,2}(x,z) = \sum_{m=-\infty}^{\infty} \hat{S}_m(z) \exp\left[-i\sigma_m x\right] \tag{3.36}$$

[2]That is, harmonic in space, analogous to e.g. fields that are harmonic in time, or time-harmonic.

where $\hat{S}_m(z)$ is the normalized amplitude of the mth space harmonic component and is a function of z only, and σ_m is given by the Floquet condition as

$$\sigma_m = \mathbf{k}_2 \cdot \hat{\mathbf{x}} - mK \tag{3.37}$$

where $\mathbf{k}_2 \cdot \hat{\mathbf{x}}$ is the x component of the wave vector of the refracted zeroth order in the grating core, or, equivalently, of the wave vector that the incident refracted wave would have in the absense of a grating modulation ($\Delta\epsilon = 0$). Thus,

$$\sigma_m = k_0 \left[\sqrt{\epsilon_a} \sin\theta - m\frac{\lambda}{\Lambda} \right] \tag{3.38}$$

where θ is the angle of refraction. Substitution of the $E_{y,2}$ Fourier expansion (3.36) in to the wave equation (3.35) yields the following coupled-wave equation [13, 19]:

$$\frac{d^2\hat{S}_m(z)}{dz^2} + \left(k_0^2\epsilon_a - \sigma_m^2\right)\hat{S}_m(z) + \frac{1}{2}k_0^2\Delta\epsilon\left[\hat{S}_{m+1}(z) + \hat{S}_{m-1}(z)\right] = 0 \tag{3.39}$$

which governs the wave propagation inside the core. There are chiefly two points that should be taken away from this expression: 1) $\hat{S}_m(z)$ couples to both $\hat{S}_{m+1}(z)$ and $\hat{S}_{m-1}(z)$, and 2) this coupling disappears for the case of an un-modulated waveguide $\Delta\epsilon = 0$. Now, in the regions of constant refractive index (1 and 3), the the electric field of the diffracted light can be given by a so-called Rayleigh expansion [86], which is a superposition of plane waves corresponding to the diffraction orders [87]. Thus in region 1, the total electric field is the sum of the incident wave and the backward diffracted waves:

$$E_{y,1} = \exp\left(-i\mathbf{k}_1 \cdot \mathbf{r}\right) + \sum_{m=-\infty}^{\infty} R_m \exp\left(-i\mathbf{k}_{1m} \cdot \mathbf{r}\right) \tag{3.40}$$

whereas in region 3, the total electric field is

$$E_{y,3} = \sum_{m=-\infty}^{\infty} T_m \exp\left(-i\mathbf{k}_{3m} \cdot (\mathbf{r} - t\hat{\mathbf{z}})\right) \tag{3.41}$$

where R_m and T_m are the normalized amplitudes of the mth reflected or transmitted waves, with wave vectors $\mathbf{k}_{1m}$ or $\mathbf{k}_{3m}$, respectively [13, 19]. Their magnitudes are naturally given by

$$|\mathbf{k}_{1m}| = k_0 n_1 \tag{3.42}$$

$$|\mathbf{k}_{3m}| = k_0 n_3 \tag{3.43}$$

where n_1 and n_3 are the refractive indices of the superstrate (region 1) and substrate (region 3), respectively. Each mth field in both the superstrate and the substrate must be phase matched with the corresponding mth space harmonic field in the grating region, i.e. the x components of the wave vectors must be equal:

$$\mathbf{k}_{1m} \cdot \hat{\mathbf{x}} = \sigma_m \tag{3.44}$$

$$\mathbf{k}_{3m} \cdot \hat{\mathbf{x}} = \sigma_m \tag{3.45}$$

Evaluating these two expressions and utilizing Snell's law:

$$n_1 \sin\theta' = \sqrt{\epsilon_a} \sin\theta \tag{3.46}$$

yields the familiar grating equations for the backward- and forward-diffracted waves:

$$n_1 \sin\theta'_m = n_1 \sin\theta' - m\frac{\lambda}{\Lambda} \tag{3.47}$$

$$n_3 \sin\theta''_m = n_1 \sin\theta' - m\frac{\lambda}{\Lambda} \tag{3.48}$$

where θ'_m and θ''_m are the angles of diffraction of the mth reflected and transmitted orders, respectively. According to Gaylord & Moharam [19], each mth space-harmonic field inside the grating produces a corresponding mth field in the superstrate and substrate[3]. However, these fields can be either propagating plane waves, or evanescent waves, depending on whether the z components of $\mathbf{k}_{1m}$ and $\mathbf{k}_{3m}$ are real or complex [86].

Weakly modulated gratings

In the case of weakly modulated gratings where $\Delta\epsilon \to 0$, the coupling term in Eq. (3.39) vanishes, and it takes a form analogous to the wave equation for an unmodulated waveguide:

$$\frac{d^2\hat{S}_m(z)}{dz^2} + \left(k_0^2\epsilon_a - \sigma_m^2\right)\hat{S}_m(z) = 0 \tag{3.49}$$

[3]In Ref. [19] Gaylord & Moharam offer this view of the diffraction process: "In an overly simplified manner, the diffraction process is sometimes interpreted as 1) the incident wave is refracted into the grating medium, 2) the refracted plane wave in the grating is diffracted into an infinite set of plane waves (or "coupled waves") propagating toward the [grating] boundary, and 3) the waves inside the grating are phase matched into propagating (and evanescent) waves in the third region." However, they warn that this view is incomplete as "backward-diffracted waves in region 1 are not predicted in this interpretation".

Comparison with Eq. (3.8) yields that the effective propagation constant of a guided mode governed by this equation β_m is given by

$$\beta_m = \sigma_m \tag{3.50}$$

For β_m to correspond to a propagating guided wave, $k_0^2\epsilon_a - \sigma_m^2$ must be positive, and thus

$$|\sigma_m| < k_0\sqrt{\epsilon_a} \tag{3.51}$$

Furthermore, an additional condition for β_m to be guided, is that the corresponding diffraction orders m in the superstrate and substrate be non-propagating [13]. This requires that the z components of their respective wave vectors $\mathbf{k}_{1m}$ and $\mathbf{k}_{3m}$ are complex, corresponding to evanescent waves. Since we know the magnitude of these vectors (Eqs. (3.42) and (3.43)), and their x components from the phase matching conditions (Eqs. (3.44) and (3.45)), we can work out their z components:

$$\mathbf{k}_{1m} \cdot \hat{\mathbf{z}} = \sqrt{k_0^2 n_1^2 - \sigma_m^2} \tag{3.52}$$

$$\mathbf{k}_{3m} \cdot \hat{\mathbf{z}} = \sqrt{k_0^2 n_3^2 - \sigma_m^2} \tag{3.53}$$

Thus, for both of these components to be complex, the following condition is required:

$$k_0 n_1, k_0 n_3 < \sigma_m \tag{3.54}$$

Combining Eqs. (3.51) and (3.54) then yields the following composite condition

$$n_1, n_3 < \left|\frac{\sigma_m}{k_0}\right| < \sqrt{\epsilon_a} \tag{3.55}$$

or

$$n_1, n_3 < \left|n_1 \sin\theta' - m\frac{\lambda}{\Lambda}\right| < \sqrt{\epsilon_a} \tag{3.56}$$

where we have made use of Snell's law (Eq. (3.46)). The range of values for the incident angle θ' and diffraction order m that satisfy this condition, correspond to the parametric regions where guided waves can be excited. Naturally, the propagation constant of these guided waves must also satisfy the relevant mode condition (Eq. (3.19)). Figure 3.8 shows the ranges of incident angles θ' that allow for guided waves to be excited within the grating waveguide for a given diffraction order m, for the case of $n_1 = n_3 = 1, \epsilon_a = 2$. From the figure it can be seen that light incident at an angle of $\theta' = 25°$ (dashed line) can excite guided waves corresponding to the $m = -1$ and $m = 2$ diffraction orders. Furthermore, by evaluating the left hand side of

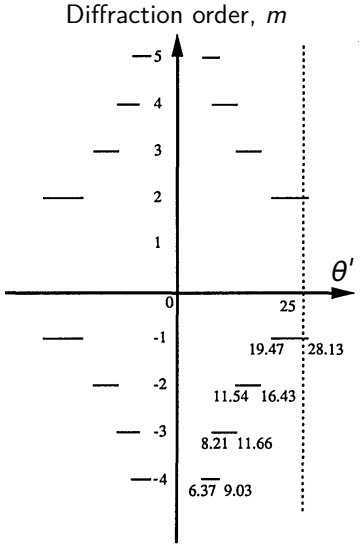

Figure 3.8: Ranges of incident angles which allow for guided modes to be excited within the grating region for the case of $n_1 = n_3 = 1, \epsilon_a = 2$ and $\lambda/\Lambda = 2\sin\theta'$ (i.e. first order Bragg condition satisfied). The dashed line corresponds to an incident angle of $\theta' = 25°$. The figure is adapted from Ref. [13].

Eq. (3.56) it can be seen that the adjacent orders $m = 0$ and $m = 1$ are propagating diffraction orders.

Relaxing the condition that $\Delta\epsilon$ is vanishing, the grating will still be able to support guided waves, with the propagation constants acquiring a non-zero complex component [88, 89]

$$\beta_m = \sigma_m - i\alpha, \quad \alpha \in \mathbb{R}^+ \tag{3.57}$$

However, if $\Delta\epsilon$ is small, Eq. (3.56) will remain a valid approximation for which values of θ' and m the guided waves can be excited. We know from the coupled-wave equation (3.39) that each space harmonic field of order m couples to both of its adjacent orders $m + 1$ and $m - 1$, and that each mth field in the grating produces a corresponding field in the cladding which can either be propagating or evanescent. If a given space-harmonic field of order m corresponds to a guided wave within the grating, but one of it's adjacent orders $m + 1$ and $m - 1$ does not, and instead to a propagating diffraction order, we thus see that guided waves within the grating can couple to externally propagating diffracted waves. Furthermore, since $\hat{S}_m$ couples to both $\hat{S}_{m+1}$ and $\hat{S}_{m-1}$, then R_m and T_m must also couple to R_{m+1}, R_{m-1} and T_{m+1}, T_{m-1}. Therefore, since the sum of the diffraction efficiencies of all waves must equal unity (Eq. (3.31)), this coupling effect can lead to

a rapid redistribution of power between the various propagating diffraction orders [13]. Since the guided waves couple to diffraction orders propagating in the cladding, they constantly leak out energy into the far field and are thereby attenuated over distance. For this reason, instead of referring to them as guided waves, they are more appropriately referred to as being leaky or quasi-guided modes, or guided-resonances [25].

Subwavelength gratings

The diffraction efficiencies of backward diffracted orders in the superstrate, and the forward diffracted orders in the substrate, are given by the following two equations, respectively [19]:

$$DE_{1m} = \mathrm{Re}\left[\frac{\mathbf{k}_{1m}\cdot\hat{\mathbf{z}}}{\mathbf{k}_{10}\cdot\hat{\mathbf{z}}}\right] R_m R_m^* \tag{3.58}$$

$$DE_{3m} = \mathrm{Re}\left[\frac{\mathbf{k}_{3m}\cdot\hat{\mathbf{z}}}{\mathbf{k}_{30}\cdot\hat{\mathbf{z}}}\right] T_m T_m^* \tag{3.59}$$

Substitution of Eqs. (3.52), (3.53) and (3.38), thus yields:

$$DE_{1m} = \mathrm{Re}\left[\sqrt{1-\left[\sin\theta' - \frac{m\lambda}{n_1\Lambda}\right]^2}\Big/\cos\theta'\right] R_m R_m^* \tag{3.60}$$

$$DE_{3m} = \mathrm{Re}\left[\sqrt{\frac{n_3^2}{n_1^2}-\left[\sin\theta' - \frac{m\lambda}{n_1\Lambda}\right]^2}\Big/\cos\theta'\right] T_m T_m^* \tag{3.61}$$

For the case of subwavelength gratings (i.e. $\Lambda < \lambda$), only the zeroth reflected and transmitted diffraction orders will propagate in the cladding as discussed previously, whereas the higher order waves can excite/constitute quasi-guided modes within the grating. For the case of normally incident light, $\theta' = 0°$, the propagation constants of the $m = \pm 1$ orders are

$$\beta_{\pm 1} = \mp\frac{\lambda}{\Lambda} \tag{3.62}$$

that is, two counter-propagating, but identical, quasi-guided modes, both of which couple to the $m = 0$ propagating diffracted orders and generate a standing wave pattern within the waveguide at resonance [89, 90]. Using RCWA, Wang & Magnusson showed that for subwavelength gratings and normal incidence, the diffraction efficiency of the reflected order can vary from 0% to 100% over a small wavelength range, as illustrated in Fig. 3.9(a).

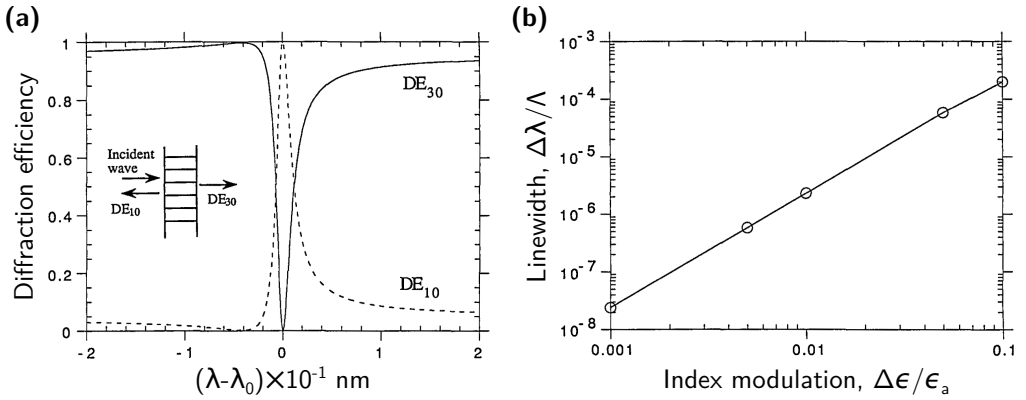

Figure 3.9: (a) Diffraction efficiencies for a subwavelength grating with only the zeroth diffracted orders propagating for the case of $\Lambda = t = 0.33$ μm, $\epsilon_1 = 1$, $\epsilon_3 = 2.161$, $\epsilon_a = 3$, normal incidence $\theta' = 0°$, $\Delta\epsilon/\epsilon_a = 0.05$, and a center wavelength of $\lambda_0 = 547$ nm. (b) The resonance linewidth as a function of grating modulation $\Delta\epsilon$. Both figures are adapted from Ref. [15].

The subwavelength grating thus exhibits sharp, resonant reflection with narrow linewidths, and a theoretical reflection efficiency of 100% at resonance. As Wang & Magnusson explain "physically, this is due to coupling of the externally propagating diffracted fields to the modes of the waveguide" [15], and is thus a Wood's anomaly of the resonance-type. This kind of rapid intensity variation in the externally propagating diffraction orders is referred to as a guided-mode resonance [17], and therefore such dielectric resonant grating waveguides have earned the name guided mode resonance filters. Since the resonant reflection is the result of coupling between two identical, counter-propagating quasi guided modes and the zeroth diffracted orders, it corresponds to a degenerate state. Breaking the symmetry by deviating θ' from zero will lift the degeneracy, and cause a split in the resonantly reflected peak. Wang & Magnusson also demonstrated that the linewidth of the resonance increases monotonously with increased grating modulation, and tends to zero as $\Delta\epsilon \to 0$, as shown in Fig. 3.9(b). Furthermore, they showed that the asymmetry of the resonance is a direct result of the asymmetric cladding conditions ($n_1 \neq n_3$), as well as the thickness of the waveguide core layer [17].

Although the results shown in Fig. 3.9(a) pertain to subwavelength gratings operating in the zero-order regime, such resonant reflection is also exhibited by grating waveguides which allow for higher order diffracted waves to propagate. However, in filtering and sensing application, the zero-order regime is typically preferred so that no energy is wasted in higher order propagating waves [89].

3.2.3 Slab waveguides with cores of periodically modulated thickness

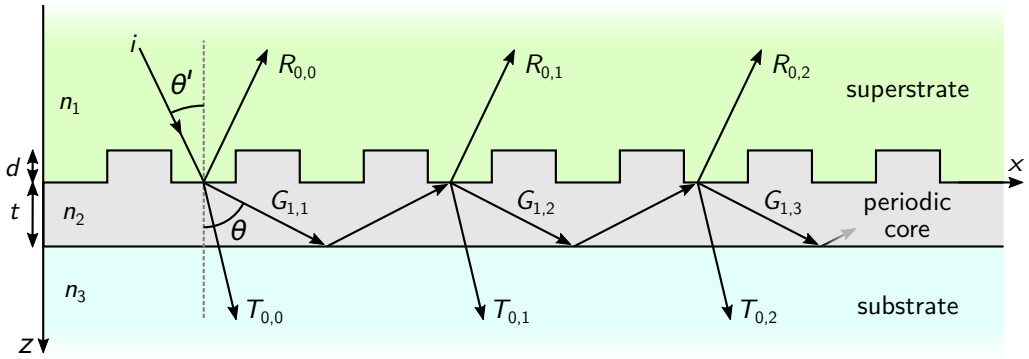

Figure 3.10: Schematic illustration of an asymmetric slab waveguide in which the thickness of the core varies periodically in the guiding direction. The figure is based on Fig. 1 in Ref. [24].

Let us now direct our attention to the following waveguide structure, where instead of the refractive index of the core being periodically modulated in the guiding direction, it is constant (n_2), but now the thickness of the core varies periodically. Figure 3.10 shows a schematic illustration of such a structure, wherein the lower material interface between the waveguide core and substrate (n_3) is flat, whereas the upper material interface between the core and superstrate (n_1) is periodically modulated by a distance d and period Λ. If $n_2 > n_1, n_3$, then such a structure is commonly referred to as a grating coupler when used for coupling out-of-plane light into guided modes within the waveguide. The following summarizes the approach and main results obtained by Rosenblatt, Sharon & Friesem [23,24] in analyzing such a grating coupler with a conceptually simple ray picture model for the case of TE-polarized light.

When a monochromatic plane wave is incident from the superstrate on the waveguide core at an angle of θ', the bulk of the light is transmitted via the zeroth transmitted diffraction order, but a small fraction is diffracted via the first diffraction order into the waveguide core. If the period of the grating is small enough, and thus the (internal) angle of diffraction is large enough (see Eq. (3.28)), the diffracted light can become trapped within the core by total internal reflection. Each time the guided light strikes the lower material interface and is reflected, it undergoes a phase change, whereas when it strikes the upper interface, a small part of it is diffracted out of the waveguide in both the forward and backward directions while the rest is

reflected inwards with a phase change due to both diffraction and reflection, and the cycle is repeated. Let us label the rays in this picture as $X_{m,n}$, where X indicates whether the ray is reflected (R), guided (G) or transmitted (T), m is the diffraction order, and n is an integer labeling the cycle. Each of the forward and backward diffracted rays, $T_{0,n}$ and $R_{0,n}$, are co-linear with the directly transmitted and reflected rays, $T_{0,0}$ and $R_{0,0}$, repectively. Each two transmitted rays $T_{0,n+1}$ and $T_{0,n}$ can be related to each other by:

$$T_{0,n+1} \propto T_{0,n} e^{i\Phi} \tag{3.63}$$

where Φ is the phase difference between $T_{0,n+1}$ and $T_{0,n}$ due to the additional path traversed by $T_{0,n+1}$, reflections and diffractions. It can be shown that:

$$\Phi = 2k_{2z}t + 2\phi_{1,2} + 2\phi_{2,3} - \pi \tag{3.64}$$

where t is the waveguide thickness, $\phi_{1,2}$ and $\phi_{2,3}$ are Fresnel phase shifts due to total internal reflection at the upper and lower interfaces, respectively, and k_{2z} is the z-component of the wave vector in the core, $k_{2z} = k_0 n_2 \cos\theta$, where $k_0 = 2\pi/\lambda$. For a ray to become guided within the waveguide, the following condition must additionally be satisfied:

$$2k_{2z}t + 2\phi_{1,2} + 2\phi_{2,3} = p2\pi \tag{3.65}$$

where p is an integer. Thus, when the internally diffracted ray is guided, combining Eqs. (3.64) and (3.65) yields that the phase difference between each two forward diffracted waves is

$$\Phi = (2p - 1)\pi \tag{3.66}$$

i.e. they are perfectly out of phase and interfere destructively in the transmitted direction. Moreover, and by the same token, since light undergoes a phase change of π when reflected from the surface of a higher refractive index than that of which it is travelling in, $R_{0,n+1}$ and $R_{0,n}$ will be in phase and interfere constructively. The total transmission through the structure can be obtained in a manner analogous to the theoretical analysis of transmission through a Fabry-Pérot etalon. For the case of a thin grating ($d \ll \lambda$) (i.e. small perturbation from an unmodulated slab waveguide), the total transmitted electric field

$$E = \sum_n T_{0,n} \tag{3.67}$$

can be shown to be

$$E \approxeq E_0 \left(1 - \frac{S\exp(i\Delta)}{1 - (1 - S)\exp(i\Delta)}\right) \tag{3.68}$$

where E_0 is the amplitude of the incident plane wave, Δ represents dephasing from the resonance condition in Eq. (3.65), e.g. due to varying the wavelength or angle of incidence, and S is a diffraction coefficient. S increases monotonously with refractive index contrast between the core and cladding as well as grating height d, and is furthermore dependent on grating duty cycle and waveguide thickness t. The resulting transmitted intensity ratio is therefore

$$\frac{T}{T_0} \approxeq \frac{\frac{1}{(1-S)}\sin^2\left(\frac{\Delta}{2}\right)}{\frac{S^2}{4(1-S)} + \sin^2\left(\frac{\Delta}{2}\right)} \tag{3.69}$$

where T is the transmitted intensity at or near resonance, and T_0 is the intensity far away from resonance. From this expression, it is clear that at resonance ($\Delta = 0$, i.e. when Eq. (3.65) is satisfied), the transmitted intensity becomes zero and no light is transmitted, i.e. it is fully reflected. Assuming small values of Δ and S, Eq. (3.69) becomes

$$\frac{T}{T_0} = \frac{\Delta^2}{S^2 + \Delta^2} \tag{3.70}$$

and thus the transmission spectrum has a Lorentzian line-shape with a linewidth of $2S$ at half maximum intensity. So far, a lossless system has been assumed, but allowing for loss due to scattering and absorption, Beer-Lambert's law gives that:

$$T_{0,n+1} \propto T_{0,n} e^{i\Phi} e^{-\alpha} \tag{3.71}$$

where $\alpha = \alpha' l/2$, where α' is the absorption coefficient of the waveguide core material, and l is the distance traversed by the light in the core during one cycle. As a result, this means that the dephasing must become complex, or $\Delta + i\alpha$. Substitution into Eq. (3.68) leads to a modified transmission of

$$\frac{T}{T_0} = \frac{\Delta^2 + \alpha^2}{\Delta^2 + (S + \alpha)^2} \tag{3.72}$$

Therefore, by including loss, the transmission no longer reaches zero at resonance ($\Delta = 0$), and furthermore, the linewidth is broadened to $2(S + \alpha)$.

In the above analysis, the equations represent steady state conditions, i.e. after a suitable amount of time has elapsed. When a plane wave with a wavelength and incident angle matching that of resonance initially impinges on the structure, most of the light will be transmitted via the zeroth transmitted diffraction order. However, at resonance, the light coupled into the

waveguide structure via the first diffraction order will accumulate [24], leading to strong field enhancement in the structure [89, 90], and eventually to complete destructive interference of light in the forward direction. In fact, finite-difference time-domain calculations of the power transmitted through such structures as a function of time [25] are characterized by an initial pulse corresponding to direct transmission, followed by its decay towards zero due to the outcoupling of the resonant light.

3.3 Discussion

In this chapter, it has been shown that by inducing a periodic perturbation in a dielectric slab waveguide structure, complete resonant reflection of incident light can occur at a particular wavelength, while the compliment of the spectrum is transmitted. This resonant behavior is due to the excitation of leaky, or quasi guided modes that are guided by the structure, and is thus known as a guided-mode resonance, and the device referred to as a guided mode resonance filter. As the quasi-guided modes propagate, they are continually decoupled out of the waveguide, and interfere with both the transmitted and reflected diffracted waves. At resonance, the decoupled light interferes destructively with the transmitted light, and constructively with the reflected light, leading to efficient resonant reflection. The wavelength at which resonance occurs depends on the materials of which the guided mode resonance filter is composted, as well as its geometry, such as core thickness and modulation period. The linewidth of the resonance is dictated by the rate of decoupling, or equivalently by the magnitude of the periodic perturbation, and the larger the rate of decoupling, the broader the linewidth. Hence, the linewidth correlates with e.g. waveguide core refractive index modulation amplitude, grating height, refractive index contrast between waveguide core and superstrate, etc. Subwavelength structures known as high-contrast gratings have utilized this property to realize ultra broadband dielectric mirrors [28], but for optical filtering and sensing applications, a narrow linewidth is generally desired. Although reflection efficiencies of up to 100% are predicted by theory, they are in practice diminished due to e.g. scattering and absorption losses, structural imperfections, as well as incident beam divergence and finite lateral device size [89].

Although the preceding discussion has been limited to transverse-electric polarized light, the same resonant behavior is also exhibited by transverse-magnetic polarized light, i.e. polarized perpendicular to the grating grooves instead of parallel to them. Due to transverse-electric and transverse-magnetic modes being governed by different mode conditions, the associated guided

mode resonances will inherently occur at different wavelengths, as well as generally having different linewidths.

Another method for describing the behavior of guided mode resonance filters is to treat them as photonic crystals, i.e. optical analogues of conventional solid-state crystals. This approach has the advantage of building on the established theory and mathematics of solid state structures in regards to electrons propagating in periodic potentials. Taking this approach, Fan & Joannopoulos [25] demonstrated that two kinds of guided waves can exist within such structures; guided modes which have infinite lifetimes and do not couple to the far field, and guided resonances with finite lifetimes, which do.[4] Furthermore, they showed how transmitted light through such structures is extinguished by the interference between the directly transmitted light and the de-coupled guided resonances, in qualitative agreement with results obtained by the approaches described here.

[4]The concepts of photon lifetimes and decoupling rates are alternate ways for describing the same physical process. The greater the rate of decoupling, the shorter the photon lifetime in a quasi guided mode becomes, and vice versa.

4 | Methods

This chapter gives an overview of the fabrication methods used to make guided mode resonance filters, and the experimental setups used for their optical characterization. The fabrication involves two separate stages: the fabrication of a nanopatterned master, followed by transferal of the pattern into a low refractive index polymer and coating with a high refractive index material. The resonance spectra can either be measured in a transmission configuration by placing a guided mode resonance filter sample between two orthogonally oriented linear polarizers, or in a reflection configuration.

4.1 Fabrication

Guided mode resonance filters can be fabricated using a variety of different lithography methods, such as electron beam lithography (EBL) [24,91], laser interference lithography (LIL) [61, 78, 92, 93], thermal nanoimprint lithography (also known as hot embossing) [34, 94], injection molding [95], and UV nanoreplication [53, 96], with further options including roll-to-roll nanoimprint lithography and deep UV stepping. Typically, a high refractive index dielectric is deposited onto a flat substrate, and after performing e.g. EBL or LIL on a resist, the resulting grating pattern is transferred into the high-index material via dry etching. Alternately, the high-index material can be deposited onto a periodically nanostructured low-refractive index substrate. Common choices for high refractive index materials include titanium dioxide, tantalum pentoxide, indium tin oxide, hafnium oxide and silicon nitride.

The disadvantage of using EBL for mass-fabrication is that it is both slow and expensive. It is an inherently serial writing method, and is limited to small writing fields (of the order of 1 mm^2) which can lead to stitching errors for larger structures [92]. In order to reduce both costs and fabrication time, EBL can instead be used to create a master or stamp, which is then used multiple times for patterning using e.g. thermal nanoimprint lithography or UV (ultra-violet) nanoreplication, thereby distributing the cost of the master

over a multitude of devices. In the case of thermal nanoimprint lithography, a polymer is sealed between a substrate and the patterned surface of a master, and a force of the order of 1-100 kN is applied by a piston while the system is heated above the glass transition temperature of the polymer. This sinks the master's structured protrusions into the polymer, and after cooling below the glass transition temperature, the high pressure is released and the master removed, resulting in a patterned polymer. The main disadvantage of thermal nanoimprint lithography is that since it involves a heating phase, an imprinting phase, and then a cool-down phase, it is quite slow. Furthermore, the forces involved in the imprinting phase can lead to a deterioration or fracturing of the master. As an alternative, UV nanoreplication can be used, given that the polymer in question can be cured by exposure to UV light. In this method, instead of applying heat and force, a solvent-free polymer is dispensed onto the master, covered with a transparent substrate, and cured using UV light. In addition to being considerably faster, this method involves far gentler treatment of the master, which leads to its increased longevity, and thus an over-all cost reduction. In this thesis, exclusive use was made of the UV nanoreplication method, and the entire fabrication process, from master to completed GMRF device, is discussed in the following.

4.1.1 Fabrication of master

The master, or stamp, is fabricated using an electron beam lithography process on silicon, as shown in Fig. 4.1. For masters containing grating areas with different geometrical parameters, such as period, duty cycle, periodicity (e.g. one-dimensional versus two-dimensional gratings), it is advantageous to define the master protrusion height by means of an oxide layer. The reason for this is that the etch rate of common reactive ion etching techniques depends on the etchable surface area in a given location, i.e. the area that is not etch-masked. The larger the area, the faster the reactive species are depleted from the etching plasma, which lowers the etching rate and renders the final etched depth dependent on pattern geometry. By creating a well-defined oxide layer, and performing a dry etch which is self-limiting when reaching the underlying silicon surface, a uniform protrusion height can be achieved irrespective of the grating geometry. Naturally, if the protrusion height is immaterial, the oxide layer can be omitted. Starting with a silicon wafer (a), usually with a 4 inch diameter and a crystal direction of <100>, it is cleaned and stripped of its native oxide layer, and then dry-oxidized in a high temperature furnace at around 1050 °C (b). The oxide layer thickness can be accurately controlled by the duration of the oxidation, with e.g. 1:35 hours resulting in an oxide thickness of 100 nm. Following this, the surface of

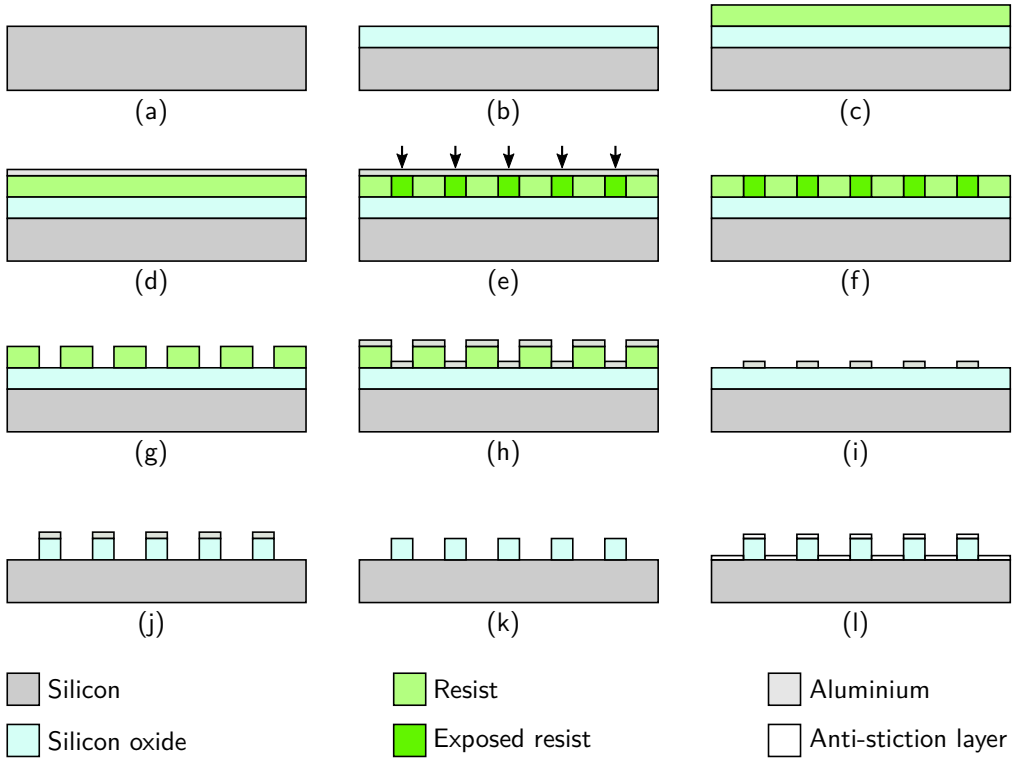

Figure 4.1: Fabrication of a master with oxide-defined protrusions using electron-beam lithography, a lift-off process, and self-limiting anisotropic dry etching.

the wafer is spun with an electron beam resist, followed by a baking-out of its solvent on a hotplate (c). Throughout this work, the positive resist ZEP520A (ZEON Chemicals) has been used[1]. In order to avoid charge build-up in the oxide during electron beam exposure, an approximately 15 nm thick charge carrying layer of aluminium is thermally evaporated onto the surface of the resist (d). For this step, electron beam metal evaporation should be avoided since the electron source produces X-rays and electrons which expose the resist. At this point, the structure is ready for pattern writing using the EBL system (JEOL JBX-9500, (e)). For a successful electron beam exposure, there are several consideration to be made. Primary electrons from the incident beam will return to the surface of the wafer at locations away from the beam's point of entry, with a maximum distance given by the substrate material's backscattering range, which for silicon is approximately 30

[1]ZEP520A is currently in the process of being phased out in many fabrication facilities across Europe due to its prohibitively high price and low availability. A commonly used replacement is CSAR (Allresist GmbH), which has a comparable clearing dose and similar chemical properties.

µm [97]. These primary electrons generate lower-energy secondary electrons by collisions which expose the resist. This results in a resist exposure away from the beam target, which is known as the proximity effect. Due to this, the clearing dose, i.e. the minimum dose required to fully expose the resist, is given for areas much larger than the backscattering range. Therefore, when writing nanostructures, a writing dose D must be chosen that is larger than that of the resist's clearing dose. When writing gratings, or other periodic nanostructure, each written grating line will experience an exposure from neighboring grating lines, the amount of which depends on the grating's duty cycle. In practice, it is common to perform dose-tests in which sample structures are written with varying doses in order to ascertain which one yields the best results. In order to estimate the pattern writing time t, the following equation can be used:

$$t = \frac{DA}{I} \tag{4.1}$$

where A is the pattern area, and I is the beam current. Thus for a $1\times$ mm^2 grating with a 25% duty cycle, written with a current of $I = 6$ nA in ZEP520A with dose of 225 µC/cm^2 (typical values), a writing time of $t = 1.6$ minutes can be expected. In addition to this, time for wafer loading, configuration and calibration of the EBL system, etc. is required, and usually takes around 45 minutes. The maximum current that can be used for writing is given by the following relation

$$\frac{I}{D\Delta x^2} < f_{\max} \tag{4.2}$$

where Δx is the beam step size, or shot pitch, and $f_{\max}$ is the maximum frequency at which the electron beam blanker can be operated ($f_{\max} = 100$ MHz for JEOL JBX-9500). Thus, if a given current and step size does not fulfill this relation, but a higher current is desired (e.g. to achieve acceptable writing times), a larger step size must be used, which reduces smoothness and resolution of the written structures.

After the electron beam writing, the aluminium charge carrying layer is chemically dissolved (f), and the exposed resist removed via an suitable developer (ZED-N50 for ZEP520A, (g)). In order to remove any residual resist at the bottom of the exposed regions, i.e. at the surface of the oxide, the wafer is briefly exposed to an oxygen/nitrogen plasma. Now, in order to transfer the written pattern into the underlying oxide, a lift-off process is performed. A layer of electron-beam evaporated aluminium is deposited onto the structure (h), and the unexposed resist chemically dissolved (i), leaving the deposited aluminium on the exposed regions of the wafer, ready

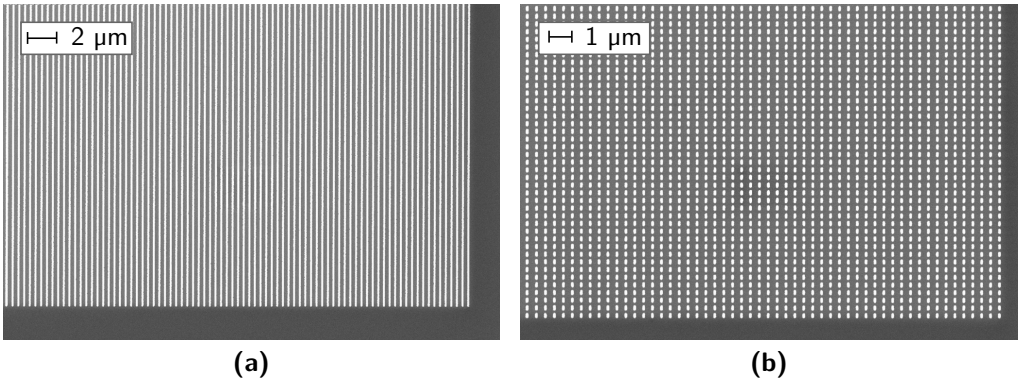

Figure 4.2: Scanning electron micrographs of silicon masters with 100 nm high silicon oxide protrusions. (a) 1D grating of $\Lambda = 386$ nm period and 25% duty cycle. (b) 2D grating with periods $\Lambda_1 = 386$ nm and $\Lambda_2 = 336$ nm, with corresponding duty cycles of 20% and 50%, respectively.

to serve as an etch mask. Any remaining organic material is burned off in a plasma asher, and the oxide is selectively and anisotropically etched using a reactive ion etch process based on a CF_4 and CHF_3 plasma, leaving the underlying silicon unaffected (j). After chemical removal of the aluminium etch mask (k), the silicon master with electron beam defined silicon oxide protrusions is coated with a single-molecule-thick anti-stiction layer of perfluorodecyltrichlorosilane (FDTS) via molecular vapor deposition (l), to yield the completed master.

Figure 4.2 show scanning electron micrographs of two silicon/silicon oxide master surfaces for the case of a linear (one-dimensional), and a biperiodic (two-dimensional) grating, both illustrating long range order and a low level of defects.

4.1.2 Device fabrication

Now that the master is complete, its nanostructured grating patterns can be transferred to a suitable polymer using UV nanoreplication, as shown in Fig. 4.3. The anti-stiction coated, nanostructured silicon master is placed face-up (a), and a small volume (~ 1 mL) of the solvent-free, low refractive index UV curable polymer Efiron PC-409 ($n = 1.40$ at 589.3 nm, SSCP Co., Ltd.) is dispensed over the structured area of the master (b). A (borosilicate) glass wafer, usually of the same dimensions as the master, is placed on top of the polymer, sealing it between the glass and the master. The joint effect of capillary forces, the weight of the glass wafer, and an optional small applied force, causes the polymer to spread out and form an even layer

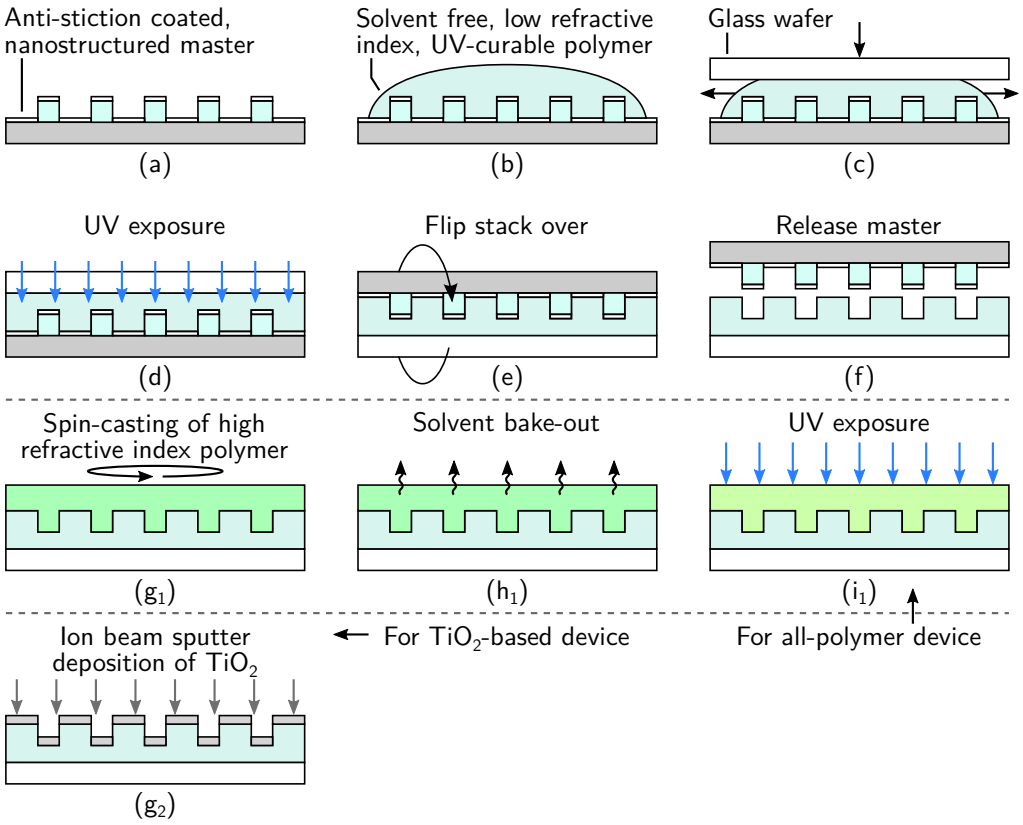

Figure 4.3: Fabrication of guided mode resonance filter devices using UV nanoreplication for the patterning of a low refractive index polymer, followed by coating with a suitable high refractive index material. The figure illustrates two approaches, either spin-casting with a high-index polymer, or ion beam sputter deposition of titanium dioxide.

(of the order of 30 μm) between the two wafers (c). The polymer is then cured by exposure to UV light through the glass (d), but since the polymerization process is photoactivated by the UV radiation, the polymer is naturally absorptive at these wavelengths. The intensity of the curing light thus decreases exponentially as it travels down through the polymer layer, in accordance with Beer-Lambert's law. Since the most critical features are at the bottom of the polymer, i.e. the interface between the master and the polymer, the exposure time must be long enough for the polymer to become cured throughout the entire layer ($\sim$ 15 minutes). The advantages of using glass over, say, plastic sheets or wafers, is that it both absorbs less UV light which is beneficial during curing, as well as offering a higher degree of mechanical stability. After curing, the stack is flipped over (e), and the master

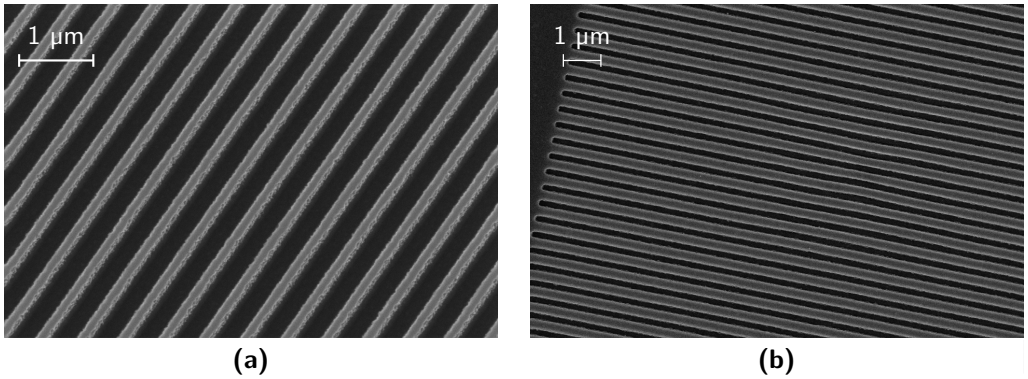

Figure 4.4: Scanning electron micrographs of a (a) silicon master and (b) its corresponding replication in the polymer Efiron PC-409.

is released by driving a wedge (e.g. a scalpel or razor blade) between the two wafers, leaving the now-nanostructured and cured polymer on the glass (f). Figure 4.4 shows a comparison of a silicon master and a corresponding UV nanoreplicated polymer surface, exhibiting the defect-free nature of the replication.

Now, depending on the nature of the high refractive index waveguide layer, the fabrication will proceed differently. If it is a polymer, such as the high-index polymer OrmoClear HI01 XP (micro resist technology GmbH) as discussed in Paper II, a solution of the polymer in a suitable solvent is spun onto the nanostructured polymer substrate (Fig. 4.3(g_1)), followed by a bake-out of the solvent (h_1) and UV curing (i_1). Oxygen in the ambient surrounding leads to a partial quenching of the polymerization of OrmoClear, leaving a thin layer of uncured polymer at the surface which must be manually rinsed away with the polymer solvent or e.g. isopropanol.

Devices based on titanium dioxide high refractive index layers are fabricated using ion beam sputter deposition (IBSD, Fig. 4.3(g_2)), with film thicknesses typically in the range $30 - 120$ nm. This is an inherently low temperature process, which is necessary in order to not destroy the nanostructured polymer surface by heating it above its glass transition temperature. Ion beam sputter deposition involves physically ejecting material from a target by a beam of high-energy ions, wherein ejected material either deposits directly onto a sample surface, or is mixed with e.g. oxygen to form metal oxides on the sample surface.

Figure 4.5 shows a cross-section of a completed GMRF device composed of Efiron PC-409 structured by UV nanoreplication and coated with 30 nm of titanium dioxide. Judging from the figure, there appears to be a degree of asymmetry in the grating protrusions. This may be due to drift during the

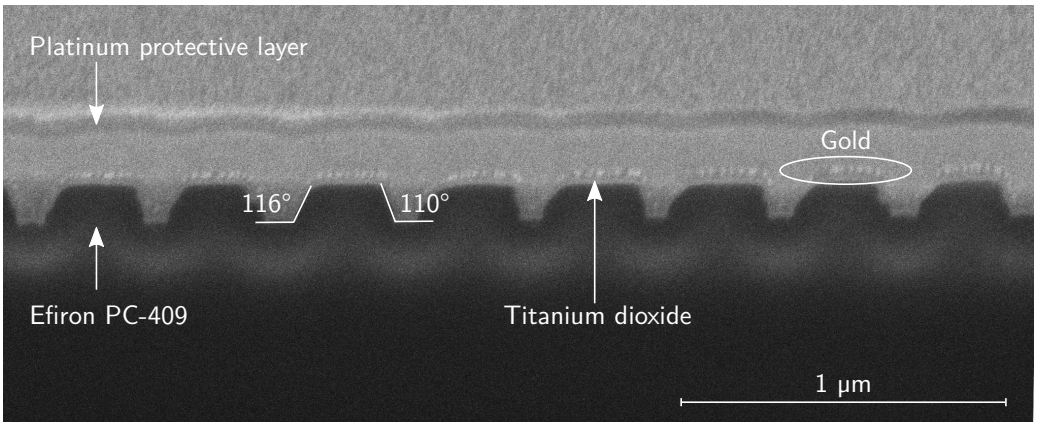

Figure 4.5: Scanning electron micrograph of the cross section of a nanoreplicated titanium dioxide-based guided mode resonance filter, cut with a focused ion-beam. In order to perform combined scanning electron imaging and ion-beam milling, the sample was coated with a layer of gold and a platinum protective layer, respectively.

measurement, but if it is not, it is though to be due to e.g. deformation of the polymer upon releasing the silicon master, or stress induced by shrinkage during curing. The measured sidewall slopes of the replicated polymer are comporable to those measured with atomic force microscopy on the original silicon master, or around 110°, although it must be borne in mind that due to tip convolution, this method is not ideal for measuring such features.

As stated earlier, the advantage of UV nanoreplication is that it's fast, inexpensive, and doesn't expose the master to high pressures or temperatures. This leads to long stamp lifetimes, with the ability to perform replications numbering in the hundreds (at least) without a degradation in the performance of the guided mode resonance filters. The disadvantage of the method however, is that it's only compatible with solvent-free[2] and UV curable polymers. Throughout this work, the polymer Efiron PC-409 was exclusively used as the substrate material. Apart from the high refractive index polymer OrmoClear HI01 XP, the high-index layer was invariably made from ion-beam sputtered titanium dioxide, which is discussed in more detail in the following.

[2]Strictly speaking, polymers with small amounts of solvent can also be used. We have experimented with reducing the viscocity of Efiron PC-409 by adding small amounts of solvent (around 10% by weight), in order to reduce the thickness of the resulting polymer GMRF substrate thickness. This has yielded promising results, but when the weight fraction becomes too large, the polymer will no longer be able to form a solid polymer matrix upon UV exposure.

Titanium dioxide

Titanium dioxide is a high refractive index, highly dispersive, birefringent dielectric material, and is a widely used substance as e.g. a paint pigment, food coloring, and as a UV blocker in sunscreen. Due to its high refractive index, it is also commonly used for making dielectric mirrors, also known as Bragg reflectors, which consist of a layer stack of periodically alternating refractive indices. When irradiated with UV light in the wavelength range 300-400 nm, it becomes photocatalytic, and breaks down organic molecules it is in contact with, an effect which has been used to realize self-cleaning surfaces [98]. Thus, for biological surface sensing using titanium dioxide-based guided mode resonance filters, this must be kept in mind if the illumination source emits light at these wavelengths, e.g. by taking steps to filter out or block all light below 400 nm. Titanium dioxide occurs naturally in several different crystal configurations, or polymorphs, such as rutile, anatase and brookite. Rutile is the most common form, and has the highest refractive index, highest birefringence, as well as being the most thermodynamically stable. Anatase is the second most common polymorph, followed by brookite, and both will convert to rutile when exposed to temperatures in excess of 750 °C. The crystal structure of the rutile and anatase unit cells are shown schematically in Fig. 4.6, with the anatase unit cell being the larger of the two.

Due to its birefringent nature, the refractive index of rutile and anatase depends on the polarization of light compared to the orientation of the crystal structure. When the light's polarization is perpendicular to the crystal's so-called optic axis, it will experience a refractive index of n_o (ordinary ray), and when polarized in parallel with the optic axis, it will experience a refractive

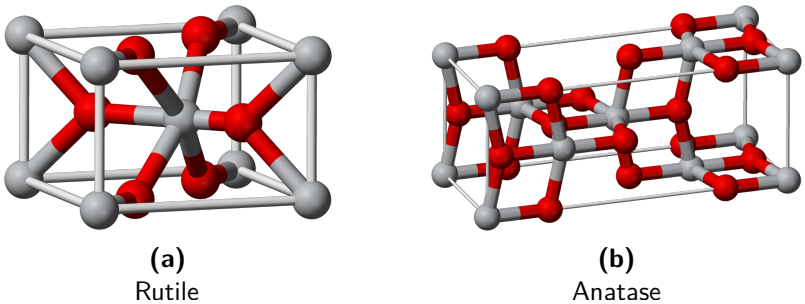

Figure 4.6: Ball-and-stick models of the unit cells of the two most common polymorphs of titanium dioxide, (a) rutile, and (b) anatase. Titanium atoms are shown as gray, and oxygen atoms as red. Figures are by Ben Mills, and licensed under Public Domain via Wikimedia Commons.

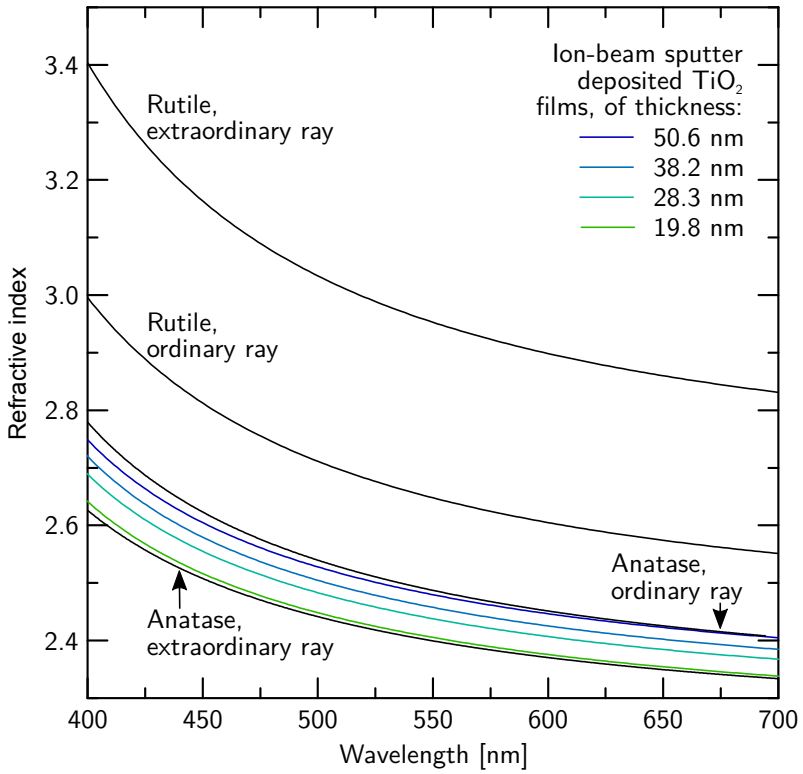

Figure 4.7: Measured refractive index dispersion of ion-beam sputter deposited titanium dioxide, compared to the refractive index of rutile and anatase, from literature [99, 100].

index of n_e (extraordinary ray). Thus, when light has polarization components along both these directions, it will experience a directional refractive index, and exhibit double-refraction. Figure 4.7 shows the bulk refractive index of rutile and anatase for both ordinary ray and extraordinary ray light, illustrating the materials' large dispersion and birefringence (i.e. $n_e - n_o$). These data are compared to that of several titanium dioxide films with thicknesses ranging between 19.8 and 50.6 nm, made by ion-beam sputter deposition on silicon wafers. The refractive index dispersion and thicknesses of these IBSD films were obtained using variable angle spectroscopic ellipsometry (VASE) and fitting to the Tauc-Lorentz oscillator model [101, 102], and it was found that rotating the film compared to the ellipsometry beam did not influence the obtained results. The refractive indices of the IBSD films exhibit a degree of thickness dependence, or at the very least process-run dependence, and lie between that of ordinary ray and extraordinary ray anatase, with the thinner films corresponding to extraordinary ray anatase, and the thicker

films to ordinary ray anatase. Based on this information alone, it is however premature to make any conclusions regarding the crystal structure of the IBSD titanium dioxide films. However, what can be concluded from this, is that there is a process dependence of the refractive index, due to e.g. film thickness, titanium target condition, impurities or contaminants from other processes etc. It is therefore clear that if a particular application of a guided mode resonance filter requires accurate knowledge of the refractive index (such as is the case in Papers I & III), the refractive index of the film must be measured in-situ, or possibly using a deposited film from an immediately subsequent deposition run.

Variable angle spectroscopic ellipsometry is the preferred method for simultaneously obtaining the thickness and refractive index dispersion of titanium dioxide films, but only yields accurate results for layer thicknesses of up to 2 μm. Since the combined layer thickness of the GMRF devices used here exceeds this limit, the properties of a titanium dioxide film cannot be obtained directly from a fabricated device, and must be obtained by other means. One such method is to attach a small chip of polished silicon to the polymer away from the nanostructured areas, deposit TiO_2 simultaneously on the two, and use the chip to measure the titanium dioxide properties with VASE.

As a final remark, it's worth noting that titanium dioxide films are generally never directly structured using e.g. plasma etching in order to create guided mode resonance filter devices, as is the case with e.g. tantalum pentoxide, indium tin oxide [78] and silicon nitride [93] films. Rather, they are usually deposited onto pre-structured substrates [53], as is the case in the present work. This is presumably not on account of its resistance to etching, as several papers have been published detailing etch processes of titanium dioxide thin films, as discussed in Ref. [103].

4.2 Optical characterization

In this work, two different experimental setups were built in order to measure the resonance spectra of guided mode resonance filters. In the first, the resonance spectra are measured in a transmission configuration by placing guided mode resonance filters between two orthogonally oriented linear polarizers. In the second, the resonance spectra are measured in reflection. Each method has its merits, as will discussed in the following.

4.2.1 Transmission setup

As explained in section 3.3, depending on whether the incident light is polarized perpendicular or parallel to the grating direction of a guided mode resonance filter, either transverse-electric (TE) or transverse-magnetic (TM) quasi guided modes will be excited within the structure. Each of these modes will give rise to its own resonant reflection, but since TE and TM modes are governed by different mode conditions, the resonant reflection associated with each mode inherently occurs at different wavelengths. Thus, guided mode resonance filters essentially behave as wavelength selective polarizers. Recalling the classic experiment often illustrated to undergraduate students, when two polarizers are oriented orthogonally with respect to each other (i.e. they are crossed), no light is transmitted through them. However, placing a third polarizer between the two at an angle with respect to their polarization axes, light will be transmitted, illustrating the vectorial nature of electric fields. Placing a guided mode resonance filter between two crossed polarizers has the same effect, but only for light in the resonance bands, thereby enabling guided mode resonances to be measured in transmission. This method has been used extensively by Y. Nazirizadeh et al. [61, 62, 78].

An experimental setup based on this principle is shown in Fig. 4.8(a). In this setup, broadband light is guided from its source, a xenon lamp (Ocean Optics HPX-2000), via an optical fiber, and then collimated with a fiber collimator (A), before being polarized with a linear polarizer (B) at an angle of $\phi = 45°$ with respect to the grating direction. In order to limit the angles of incidence and to control illumination spot size, a variable aperture (C) is placed adjacent to the sample surface. The GMRF sample (D) is mounted on a combined 3-axis translation and goniometer stage and positioned such that the broadband light is normally incident on the sample surface. In both the TE and TM resonance bands, the GMRF reflects a component of the light leading to an effective rotation in polarization, which in turn enables partial transmission through the second polarizer (E, $\phi = -45°$), while the rest of the spectrum is blocked. A condenser lens (F) focuses the transmitted light into an optical fiber which leads it to a spectrometer for analysis (Jaz, Ocean Optics). Figure 4.8(b) illustrates the polarization and intensity I of the light between each of the optical components for the cases when the light is off-resonance, and when it is in the TE and TM resonance bands. Figure 4.8(c) furthermore shows the relative intensity of light as a function of wavelength λ around one of the resonances before and after it passes through the second polarizer (E), illustrating how the light off-resonance is filtered out, resulting in a measured spectrum characterized by a peak at the resonance wavelength.

The advantage of this setup is that it requires relatively few and inexpen-

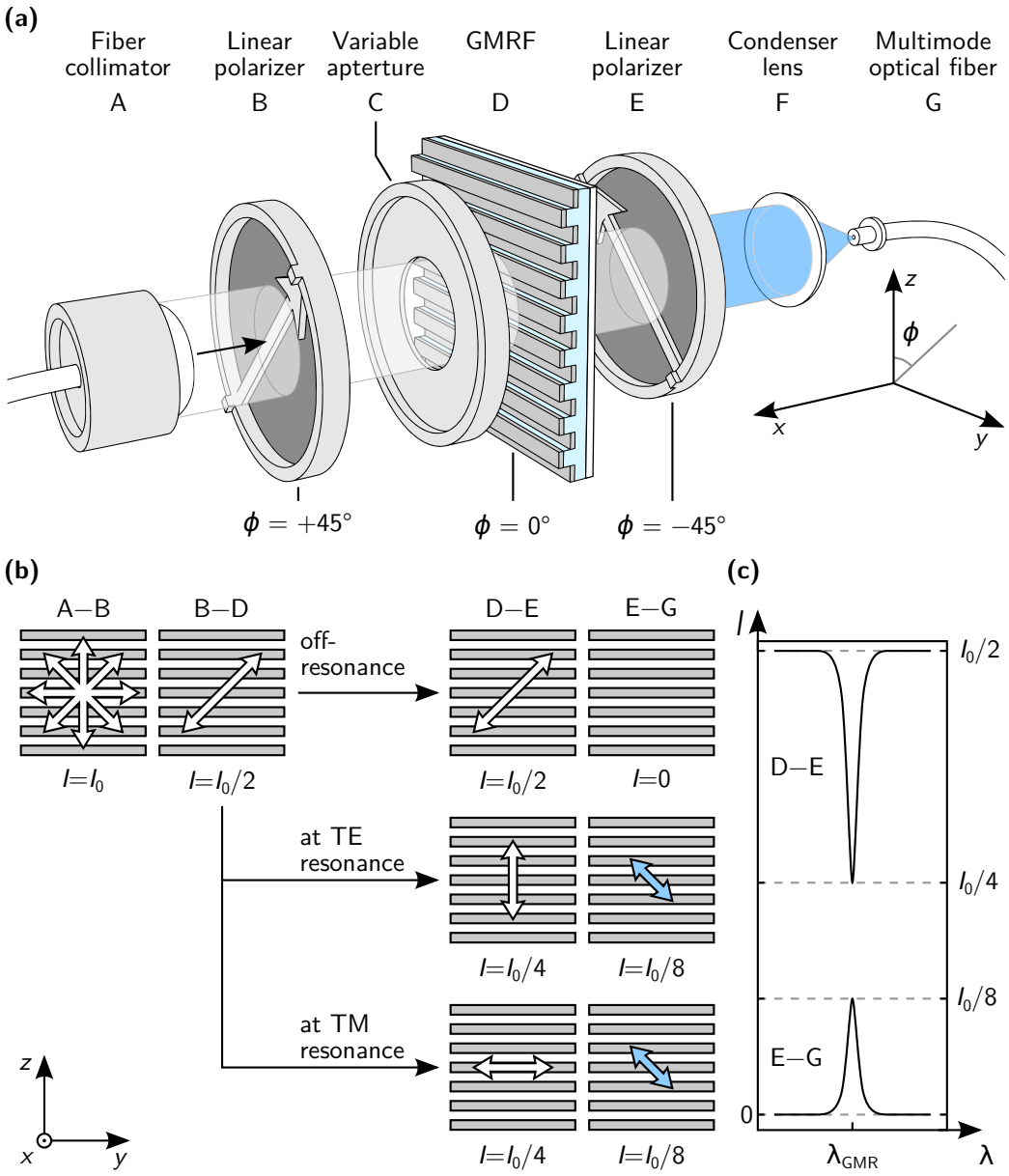

Figure 4.8: (a) Experimental setup for measuring the resonance spectra of guided mode resonance filters in transmission by placing them at an angle of $\phi = 45°$ between two orthogonally oriented linear polarizers. (b) A flowchart illustrating the polarization and relative intensity of light between each of the optical components. The horizontal gray bars denote the grating lines. (c) The intensity of light I as a function of wavelength λ around one of the resonances before and after passing through the second polarizer (E).

sive components, and thus can be made to be very compact at a low cost. The primary disadvantage of this method is however the fact that it cannot selectively measure resonances associated with either TE or TM polarized quasi guided modes; both must inherently be measured simultaneously. Usually, the TE modes have lower quality factors and will thus appear brighter in the transmission measurement [62], which may drown out the TM signals which have higher quality factors, and thus appear darker. For refractive index sensing applications, using the TM associated resonances for peak-tracking is often desirable as they usually have smaller linewidths yet higher refractive index sensitivities, so their being washed-out a bright TE resonance is unfavorable. This is e.g. illustrated in Fig. 1.3(a).

4.2.2 Reflection setup

The resonance spectra of TE and TM modes can be measured independently in reflection using the experimental setup illustrated in Fig. 4.9. Here, broadband light is fed to the setup via a multimode optical fiber and collimated with a fiber collimator. An image of the fiber tip is then focused and reflected into the image plane of a microscope objective by a lens and a 50:50 beamsplitter, respectively. This causes the light to emerge collimated from the other side of the objective and illuminate the guided mode resonance filter at normal incidence, exciting both TE and TM polarized quasi guided modes. The GMRF sample is placed on a motorized, computer-controlled, transmission microscopy scanning stage, with a mounting bracket adapted to hold full 4 inch sized wafers. The reflected light travels backwards through the objective and beamsplitter where it encounters a microscope tube lens which focuses it simultaneously onto the entrance slit of an imaging spectrometer (Princeton Instruments Acton SP2750) and a camera sensor (Thorlabs DCC3240C), via a polarizing beamsplitter. Inside the spectrometer, the light is diffracted by a grating attached to the side of a triangular revolvable turret, and projected onto a CCD camera (Princeton Instruments Pixis 100). Each of the three sides of the turret contains a grating of 150, 600, and 1800 lines/mm, corresponding to a resolution of 12, 43 and 176 pm/pixel on the camera, respectively, and the most appropriate grating is selected by rotating the turret. The camera is further connected to a computer, which records the spectrum. The spectrometer is routinely calibrated in the visible and near infra-red regimes with respect to a helium and neon-argon calibration source. The polarizing beamsplitter reflects s-polarized light to the spectrometer, while p-polarized light passes through it to the camera sensor, where it is captured, transmitted to the computer and used for visual inspection of the guided mode resonance filter sample as well as positioning. When the GMRF

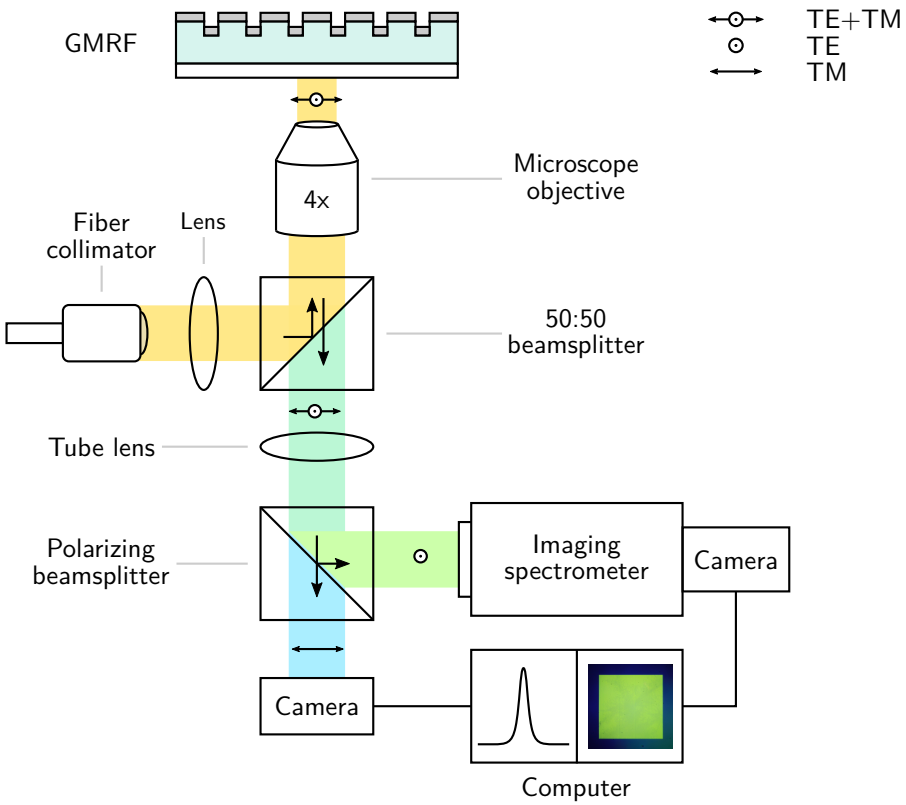

Figure 4.9: Experimental setup for selectively measuring resonance spectra of guided mode resonance filters associated with a specific polarization, in reflection.

is oriented as shown here, resonant reflections associated with TE-polarized quasi guided modes correspond to an s-polarization and are thus reflected to the spectrometer, while resonant reflections associated with TM-polarized guided modes correspond to a p-polarization and are transmitted towards the camera. This thus allows for the selective measurement of TE associated resonances, while simultaneously eliminating the TM resonances' contribution to the acquired signal noise. Conversely, in order to measure TM-polarized resonantly reflected light with the spectrometer instead, the GMRF sample can be rotated by 90°, in which case the TE-polarized resonantly reflected light will be directed to the camera. For measuring resonances associated with both polarizations simultaneously, the rotation angle of the GMRF can be set at e.g. 45°. The setup has a selection of three different light sources: 1) a high-brightness, spectrally smooth, broadband laser-driven light source (Energetiq EQ-99XFC), 2) a stabilized tungsten-halogen light source (Thorlabs SLS201/M), and 3) a high power light emitting diode with a nominal

emission wavelength of 565 nm (Thorlabs M565L3).

The advantage of this setup is that it is robust, and can selectively measure resonant spectra associated with a given polarization. However, compared to the transmission setup, is it rather more involved, as it e.g. makes use of two beamsplitters and the simultaneous focusing of light onto both the spectrometer and camera. It is thus both more expensive, and requires a greater degree of optical alignment and a more meticulous placement of the lenses. In order to reduce the degrees of freedom of the system and thereby simplifying the alignment, the entire optical path was built with an optomechanical cage system, making it self-aligning to an extent.

In an earlier generation of this setup, instead of using a polarizing beamsplitter to selectively redirect resonant light associated with a particular polarization to the spectrometer, a linear polarizer was placed immediately after the broadband light source, and rotated so that quasi guided modes of the desired polarization were excited. Then, in place of the polarizing beamsplitter, a 90:10 beamsplitter was used to redirect the majority of the light to the spectrometer, while a smaller fraction was directed to the camera for positioning. The advantage of the setup as depicted in Fig. 4.9, is that none of the resonant light of interest is lost for positioning and sample inspection since the light corresponding to the unwanted polarization is used for that purpose instead, leading to an improved signal-to-noise ratio. Furthermore, linear polarizers tend to be rather absorptive, further reducing the intensity of the ultimately acquired signal.

Fabry-Pérot interference

Due to the fact that the guided mode resonance filters are composed of several planar dielectric layers, it is inevitable that a certain degree of Fabry-Pérot (FP) interference will arise in both transmission and reflection, and become overlaid on the acquired resonance spectra. For the case of normally incident light, the free spectral range (FSR) of Fabry-Pérot interference fringes, i.e. the wavelength spacing between two consecutive interference fringes, or peaks, is given by the following

$$\Delta\lambda_{\mathrm{FP}} = \frac{\lambda^2}{2nl + \lambda} \tag{4.3}$$

where n is the refractive index of a planar layer of thickness l. As described earlier, the GMRF devices used in this thesis are composed from a nanostructured low refractive index polymer, coated by either a titanium dioxide or an OrmoClear HI01 XP high refractive index layer, and supported by a glass wafer. The following table gives an overview of typical thicknesses of each

of these layers, and the resulting Fabry-Pérot free spectral range at $\lambda = 550$ nm as given by Eq. (4.3).

Material	n	l	$\Delta\lambda_{\mathrm{FP}}$
Glass	1.5	0.5 mm	0.2 nm
Efiron PC-409	1.4	30 µm	3.6 nm
TiO_2	2.45	60 nm	360 nm
OrmoClear HI01 XP	1.6	200 nm	254 nm

Based on this, for measuring guided mode resonance signals with linewidths of the order of 10 nm, it is clear that only Fabry-Pérot interference due to the glass wafer and the Efiron PC-409 polymer substrate may give rise to undesirable interference effects. Figure 4.10(a) shows a typical GMRF spectrum acquired in reflection, characterized by a dense interference signal overlaid on the resonance spectrum. On account of the signal's periodicity, it is clear that it is due to the glass wafer. With reference to Eq. (4.3), the only way to mitigate this issue, is to alter the optical thickness l by some means. The FSR could potentially be expanded by using considerably thinner glass, but it would be too fragile to be of use. Therefore, the interference fringes must be removed by compressing the FSR below the resolution of the spectrometer system by increasing l. Glass wafers of thicknesses up to 2 mm are compatible with the cleanroom processing wafer-holders, but even then, the FSR is larger than the resolution of the spectrometer system.

In order to solve this issue, a 5 mm thick PMMA plastic block was laser-cut into a circular disk with the same diameter as the glass support wafer. By placing it beneath the GMRF sample, and adding a small amount of a refractive index matching liquid between the two (Fig. 4.10(b)), the Fabry-Pérot fringes could be completely removed from the acquired reflection signals, as shown in Fig. 4.10(a). PMMA was chosen for this purpose on account of it having a similar refractive index as the glass support wafers ($n = 1.49$ at 550 nm). The best results are obtained when using refractive index matching liquids with indices between that of the glass and the PMMA. However, since such liquids are usually oil-based, and can therefore be hard to clean off, glycerol can be used instead ($n = 1.47$ at 550 nm), at the cost of less efficient removal of the Fabry-Pérot signal.

Naturally, the Efiron PC-409 substrate polymer layer also leads to its own Fabry-Pérot signal which is overlaid on the acquired resonance spectra. Due to the nature of the fabrication, the polymer's thickness is determined by its viscosity, i.e. how easily it flows between the master and glass. Its thickness could in principle be increased during fabrication by e.g. the use of spacers, but this would come at a cost of thicker samples, and thus greater material costs and longer curing times. Moreover, the thickness would need to be

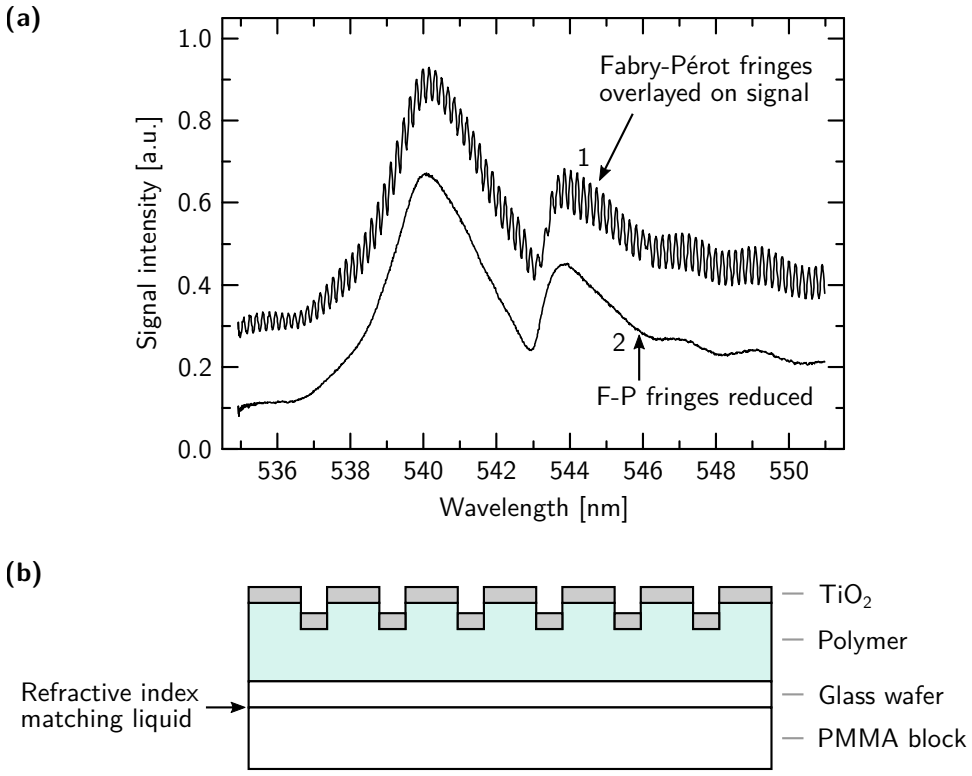

Figure 4.10: (a) 1. A measured guided mode resonance spectrum overlaid with Fabry-Pérot interference due to the glass support wafer. 2. Removal of the Fabry-Pérot interference signal by increasing the optical path of the glass by way of a thick plastic block, connected to the glass via an index matching liquid, as shown in (b).

increased considerably in order to effectively remove the interference. Thus, the only remaining option is to make the polymer layer thinner, and expand the free spectral range of the interference associated with it such that it no longer has an effect on measurements. Efiron PC-409 is soluble in butanone (methyl ethyl ketone), and it was found that by adding a small amount of this solvent (around 10% by weight), its viscosity could be substantially reduced while remaining curable under UV light, allowing for considerably thinner films to be made which no longer exhibit undesirable interference effects.

5 | Papers

5.1 Summary of Paper I

This paper presents an analytical model for predicting the resonance wavelengths of guided mode resonance filters in a straight-forward manner. For the purpose of understanding and design, the resonance spectra of guided mode resonance filters are typically calculated using rigorous couple wave analysis, or software suites based on finite-difference time-domain simulations, which often require costly license fees and long calculation times. In the presented analytical model, guided mode resonance filters are modeled as slab waveguides in which the propagation constant β must obey the following condition

$$\beta = \frac{2\pi}{\Lambda} \pm k_0 n_1 \sin\theta \tag{5.1}$$

where Λ is the grating period, k_0 is the wave number of light in free space, n_1 is the refractive index of the medium in which the incident light propagates, and θ is its angle of incidence on the device, measured with respect to its surface normal. Figure 5.1(a) illustrates this concept for a three-layer guided mode resonance filter structure, with a high-index layer thickness t and refractive index n_2, supported by a nanostructured substrate (n_3), for the case of normally incident light. By solving the waveguide's transverse-electric or transverse-magnetic mode condition together with the above condition, for k_0, the resonance wavelength is obtained via $\lambda_{\mathrm{R}} = 2\pi/k_0$. There can of course be multiple solutions for λ_{R}, depending on how many modes are supported by the waveguide.

The model is experimentally verified for the case of transverse-electric polarized modes and normal incidence, using guided mode resonance filter samples composed of a nanostructured polymer covered with a titanium dioxide high refractive index layer. By measuring the resonance wavelengths as a function of grating period and refractive index on top of the high-index layer (henceforth known as the superstrate, n_1), the model is shown to be capable of predicting the absolute resonance wavelengths to a sub-nanometer

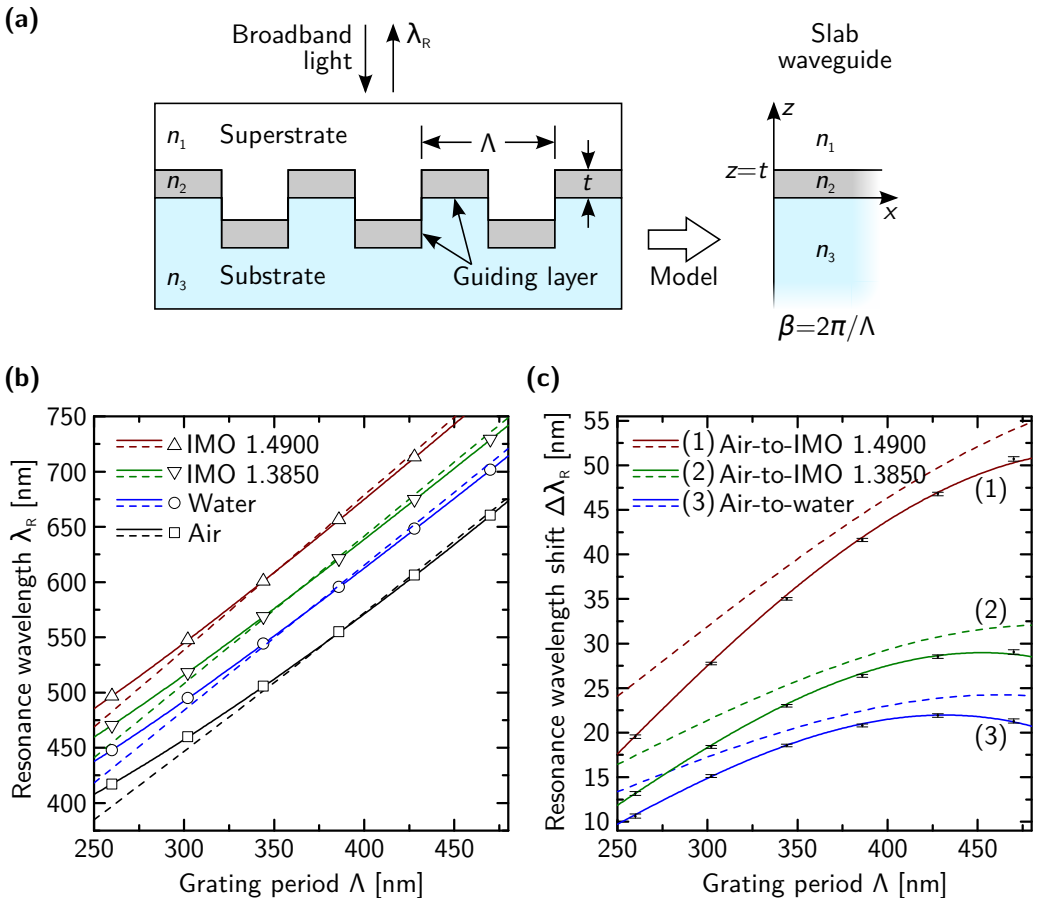

Figure 5.1: (a) Schematic diagram of the guided mode resonance filter in question and how it is modeled as a slab waveguide with a constraint placed upon the propagation constant β. (b) The location of the guided mode resonances λ_R for a $t = 28$ nm thick TiO_2 guiding layer on a polymer substrate with a periodic surface height modulation as a function of grating period for several different superstrate materials. The solid lines denote model results where material dispersion is included, the dashed lines model results when dispersion is ignored, and the points denote measured resonance wavelengths. Each of the curve groups in ascending order have been shifted by 0, 20, 40 and 60 nm, respectively, for clarity. (c) The resonance shift $\Delta\lambda_R$ due to the replacement of air as a superstrate with three different liquids (water and two index-matching oils).

accuracy, as well as resonance wavelength shifts due to changes in superstrate index to an accuracy of within 0.45 nm across the visible wavelength regime, as shown in Fig. 5.1(b) and (c)

Since the resonance wavelength λ_R is of course not known in advance of the calculation, the refractive indices of the materials comprising the guided

mode resonance filter at this wavelength are not known either. Thus, refractive index dispersion was taken into account using an iterative approach. Starting with an initial guess wavelength $\lambda_{i=0}$, the refractive indices of the materials comprising the structure are interpolated from measured dispersion data at this starting wavelength. From there, a new resonance wavelength λ_{i+1} is calculated, and this process is repeated until the calculated wavelength converges on a value within a given tolerance ϵ, such that $\lambda_{i+1} - \lambda_i < \epsilon$, at which point the resonance wavelength becomes $\lambda_R = \lambda_f$, the final wavelength. Of course, if the materials' refractive indices can be expressed in terms of an analytical expression, such an iterative approach is not needed. The refractive index dispersion of titanium dioxide is most accurately described using a Tauc-Lorentz oscillator model, and its analytical expression in terms of wavelength is quite complex. Many commercially available ellipsometry systems allow for fitting of ellipsometric data to the Tauc-Lorentz model, but are unfortunately not transparent enough in relating the obtained results to the analytical expression they use internally, but rather give the dispersion in a numerical format. Hence, it can often be more convenient to simply use the numerical data, and e.g. perform iteration as described here.

Further discussion

The primary disadvantage of the presented model is that it does not yield any information regarding the spectral shape of the resonance, which is beyond its scope. However, its advantage is that it is conceptually simple, easily implementable, computationally cheap, and can account for material dispersion, even without an analytical expression to describe it. For applications such as biosensor optimization, where refractive index changes close to the sensor surface as opposed to changes in the superstrate bulk refractive index are to be detected, the model can be extended to, e.g., a four layer waveguide [71], in a straight-forward manner with an additional layer atop the waveguide core representing the biofilm or analyte to be detected. Furthermore, by adapting the model to calculate the resonance wavelength as a function of superstrate refractive index and high-index layer thickness, the layer thickness which gives the optimum device sensitivity for a given superstrate refractive index can be automatically found. Figure 5.2 shows the results of such a calculation for the case of an Efiron PC-409 (SSCP Co., Ltd) polymer substrate with a titanium dioxide high-index guiding layer. Here, the device sensitivity, i.e. the rate at which the resonance wavelength changes with changing superstrate refractive index, is shown as a function of high-index layer thickness for several superstrate refractive indices, for both the fundamental TE mode (a) and TM mode (b). As the figure illustrates,

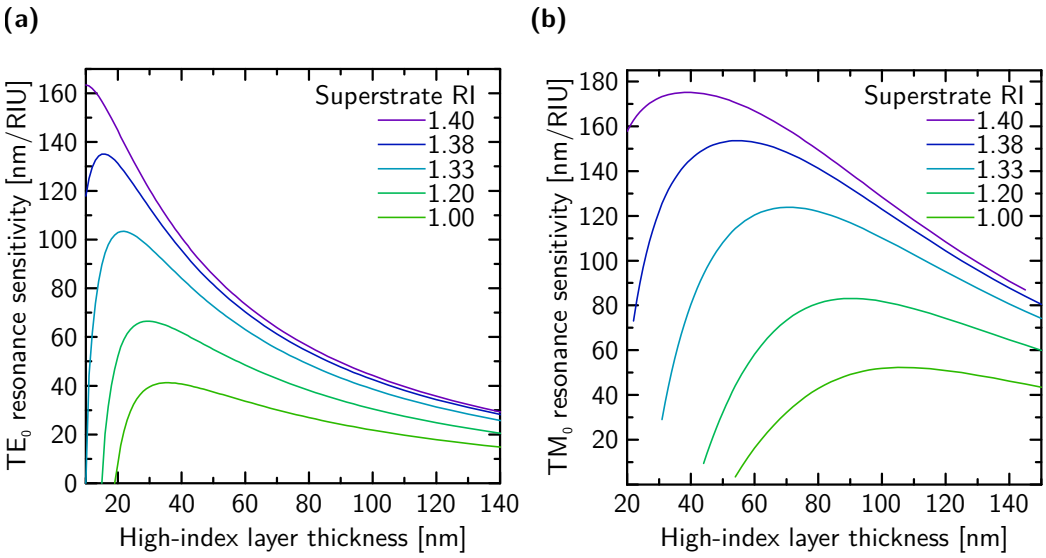

Figure 5.2: The resonance wavelength sensitivity as a function of high-index layer thickness for a guided mode resonance filter composed of an Efiron-PC-409 nanostructured polymer substrate with grating period $\Lambda = 384$ nm, covered with a titanium dioxide high refractive index layer for the case of (a) the fundamental transverse-electric and (b) the fundamental transverse-magnetic quasi guided modes, respectively.

for a given superstrate refractive index, there is a particular high-index layer thickness that yields the optimum device sensitivity. Paper II discusses this optimization process in more detail for the case of an all-polymer guided mode resonance filter.

A further advantage of this model is that it contains an explicit variable for the resonance wavelength, as opposed to e.g. rigorous coupled wave analysis, which does not. Thus, measurements of the resonance wavelength can be used in conjunction with the model to calculate a particular parameter of interest. This concept is made use of in Paper III, where measurements of resonance wavelengths as a function of grating period are used to accurately measure the refractive index dispersion of liquids.

5.2 Summary of Paper II

Guided mode resonance filters are typically fabricated by the deposition of a high refractive index dielectric onto a either a previously nanopatterned substrate of a lower refractive index, or a flat substrate, and then performing patterning directly on the high-index layer. Among the high refractive index

materials used for these purposes are titanium dioxide, tantalum pentoxide, hafnium oxide, indium tin oxide and silicon nitride, all of which require the use of a vacuum deposition process, such as ion beam sputter deposition, plasma enhanced chemical vapor deposition, etc. In addition to the cost overhead of running and maintaining such deposition equipment, vacuum deposition processes are in general quite slow. Thus, if the high refractive index layer could consist of a spinnable polymer, it would bring down the cost per device, thus rendering them more suitable for low-cost, single-use/disposable sensing applications.

This paper presents just such an all-polymer guided mode resonance filter refractive index sensor. It is composed of a nanostructured low-refractive index polymer substrate ($n = 1.4$ at 589 nm), and a high-refractive index polymer layer ($n = 1.6$ at 589 nm) which fills the grating grooves and serves as the waveguide layer. The surface of the high-index layer further constitutes the sensor surface. Figure 5.3(a) shows a schematic illustration of the device and its operation. The low-index substrate is comprised of the UV-curable, solvent-free polymer Efiron PC-409, whereas the high refractive index waveguide layer is made from an inorganic-organic hybrid polymer modified with ZrO_2-based nanoparticles (OrmoClear HI01 XP, micro resist technology GmbH). In order to understand the general behavior of the sensor for the purpose of guiding device fabrication, its sensitivity as a function of high-index layer thickness was calculated using the model presented in Paper I. This yields that for sensing refractive indices around that of water, the optimum high-index layer thickness is of the order of 100 nm, and then drops off monotonously with increasing thickness.

The all-polymer device is fabricated by UV nanoreplication and spin-casting, and its structure characterized using atomic force microscopy and scanning electron microscopy. The polymer sensor is then experimentally characterized, and shown to exhibit sub-nanometer resonance linewidths, with two examples of acquired resonance spectra shown in Fig. 5.3(b). To fully describe the performance of a resonant refractive index sensor, two parameters must be provided: the device sensitivity when exposed to a given refractive index, s, and the resolution of the sensor R, which is the smallest spectral shift in the resonant signal that can be accurately detected [64]. The ratio between the two is known as the detection limit, or the smallest refractive index change the sensor can measure (see section 2.2.2 for further details).

In order to experimentally quantify the sensitivity of the device, the peak resonance wavelength shift was measured as a function of refractive index on the sensor surface, n. These data are fitted to model results which provide a continuous theoretical curve describing the shift, the slope of which yields

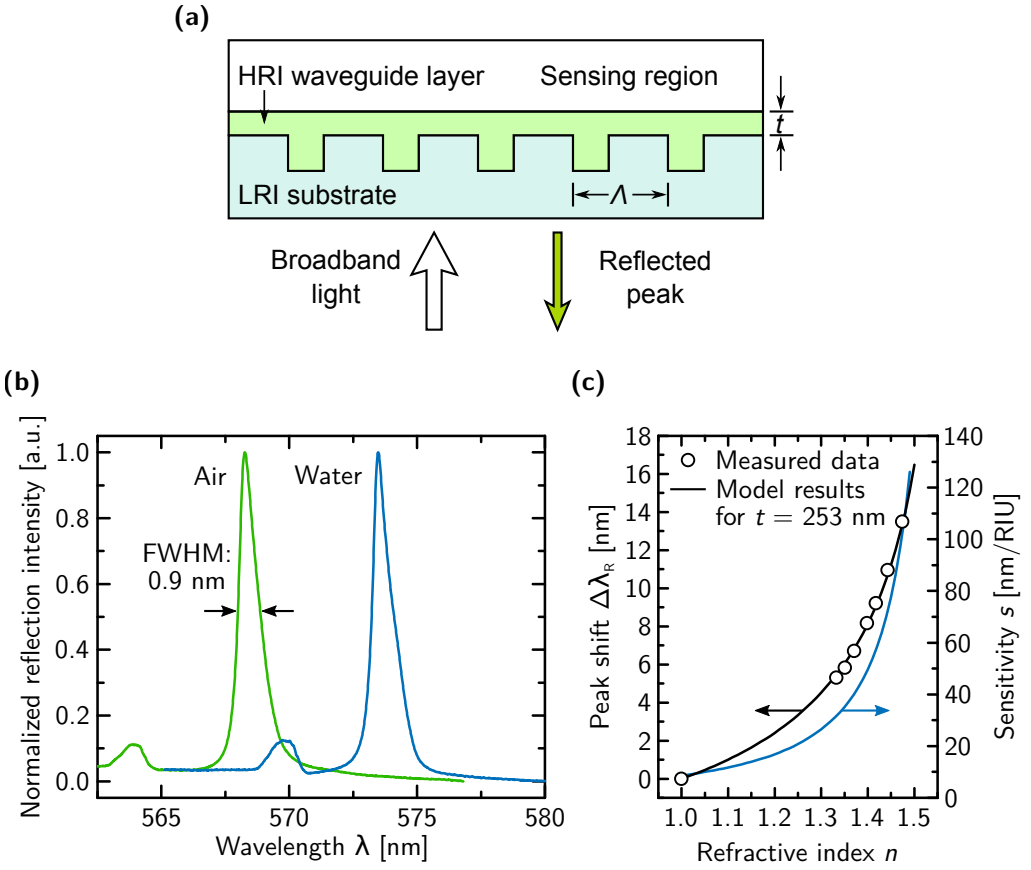

Figure 5.3: (a) Schematic illustration of the all-polymer guided mode resonance filter sensor, and its operation. (b) Examples of acquired resonance spectra associated with transverse-electric polarized quasi guided modes for the cases of air and deionized water. (c) Measured peak wavelength shift $\Delta\lambda_R$ as a function of refractive index in the sensing region n, compared to simulation results (black, solid line). The sensitivity of the device s as a function of n, obtained from the slope of $\Delta\lambda_R(n)$ is further shown on the right axis.

the sensitivity of the device as a function of sensing region refractive index, as shown in Fig. 5.3(c). From this, it can be seen that when sensing materials with refractive indices around that of water, the device sensitivity is $s = 31$ nm/RIU, and when sensing media with refractive indices around that of $n = 1.38$, corresponding to water solutions containing cells, proteins etc, the sensitivity is $s = 43$ nm/RIU. The device's sensitivity is around a factor of 3-4 times lower than that of its titanium dioxide counterparts, but makes up for it by having a 3-4 times smaller resonance linewidth.

The resolution of the sensor is commonly defined as being three standard

deviations of the measured peak wavelength of the resonance signal, $R = 3\sigma$. Thus, in order to measure the sensor resolution, 100 measurements of the resonance spectrum were recorded while the sensor surface was exposed to water, and for each recorded spectrum, its center wavelength was automatically determined with a center of mass calculation. The standard deviation of these center wavelength datapoints yielded a measured sensor resolution of $R = 0.14$ pm, and thus a detection limit of 4.5×10^{-6} RIU when sensing media with refractive indices around that of water. For biological sensing applications with refractive indices around $n = 1.38$ RIU, the detection limit can be expected to be even lower, or 3.2×10^{-6} RIU.

Further discussion

Throughout the bulk of this thesis work, guided mode resonance filters based on titanium dioxide high-index layers have been used. These devices were fabricated using ion beam sputter deposition, which is in general quite expensive, and very slow. Upon the first deposition run, the titanium target requires a 20 minute heating process, after which the sample can be transferred into the deposition chamber from the load-lock. After a gas-flow stabilization sequence is concluded, the deposition may begin, with a typical deposition rate of 2 nm per minute. Thus, the entire deposition process of a high-index titanium dioxide layer on a single wafer takes between 30 and 60 minutes, depending on the thickness. In contrast, the processing of an all-polymer guided mode resonance filter requires a 1 minute spinning, followed by a 5-minute solvent-bake out and 10 minutes of UV curing, which can easily be parallelized so that multiple samples are processed simultaneously. Thus, making the guided mode resonance filters entirely from UV nanoreplication and polymer spin-casting has the potential to reduce their production costs significantly. This would make them better-suited for high-throughput industrial production, and therefore ideal for single-use refractive index sensing applications.

5.3 Summary of Paper III

Although the refractive index is one of the fundamental properties describing how light interacts with matter, relatively few methods exist to measure its wavelength dependence, known as dispersion. The state-of-the-art for measuring refractive index dispersion of liquids is the so-called Newton-Fraunhofer method of minimum deviation, originally developed over two centuries ago. In this method, monochromatic light is directed through a

prism-shaped cell filled with a sample liquid at an angle of incidence such that the deflection caused by the prism is minimized. By measuring the deflection angle, the refractive index of the liquid at that particular wavelength can be calculated using an analytical expression. By using light of well defined wavelengths, such as lamps with atomic emission lines or laser sources, the refractive index dispersion of the liquid can be obtained. The Newton-Fraunhofer method has an achievable accuracy of $\pm 10^{-5}$ RIU [104], and is practically limited by the thermo-optic coefficient of the liquid and the degree to which the liquid can be thermally stabilized. Furthermore, for high-precision measurements, the effects of the air surrounding the prism and the prism cell material must be taken into account.

Another widely used tool for measuring refractive indices is the Abbe refractometer, which has traditionally only had the capability of measuring refractive indices at a single wavelength, namely the Fraunhofer D-line (589.3 nm). More recently, Abbe refractometers have been developed that can measure at several wavelengths by the use of interference filters, but these wavelengths are few and far between, typically only 450 nm, 589 nm, and 680 nm in the visible wavelength regime. Currently, the measurement accuracy of the state-of-the-art commercially available Abbe refractometers[1] is $\pm 2 \times 10^{-4}$ RIU. Other methods for measuring dispersion have been proposed, e.g. based on white light interferometry [105] and fiber Raman lasers [106], but these methods are either incompatible with liquid materials, or have only been demonstrated to yield the relative dispersion profile of a liquid, but not its absolute refractive index values.

In this paper, a method is presented for measuring the absolute refractive index dispersion of liquids using an array of guided mode resonance filters of varying periods. The advantage of this method compared to e.g. the Newton-Fraunhofer method is that it is far more compact, and requires three orders of magnitude smaller volumes of liquid for analysis. This method can measure the refractive index at an arbitrary number of wavelengths simply by adjusting the number of distinct periods in the array, and is well-suited for optofluidic lab-on-a-chip applications. The guided mode resonance filter array is composed of a nanostructured low-refractive index polymer substrate, coated with a high-index layer of thickness t. Sample liquids to be measured are dispensed onto the surface of the high-index layer.

When a guided mode resonance filter resonates at a particular wavelength λ_{R}, the resonant light is effectively experiencing the refractive indices of the materials comprising the device and sample liquid at that particular wavelength, as illustrated by Fig. 5.4(a). Thus, clearly, the resonance wavelength

[1] Atago Multi-wavelength Abbe refractometer, model DR-M4

contains information regarding the sample's refractive index at that particular wavelength. In the paper, the following analytical expression for the sample refractive index as a function of resonance wavelength of transverse-electric polarized modes is derived, based on the model presented in Paper I:

$$n_1(\lambda_{\mathrm{R}}) = \frac{1}{k_0}\sqrt{\frac{4\pi^2}{\Lambda^2} - \left(\frac{h\tan(ht) - p}{1 + p\tan(ht)/h}\right)^2} \tag{5.2}$$

where

$$q = [\beta^2 - n_1^2 k_0^2]^{1/2} \tag{5.3}$$
$$h = [n_2^2 k_0^2 - \beta^2]^{1/2} \tag{5.4}$$
$$p = [\beta^2 - n_3^2 k_0^2]^{1/2} \tag{5.5}$$

and $k_0 = \lambda_{\mathrm{R}}/2\pi$, $\beta = 2\pi/\Lambda$, and n_2, n_3 are the refractive indices of the high-index layer and substrate, respectively, at the resonance wavelength. Furthermore, utilizing the fact the resonance wavelength can be tuned by the grating period Λ, an array of guided mode resonance filters can be established so that the resonances span the visible wavelength regime. Thus, by measuring the resonance wavelengths of the guided mode resonance filters as a function of period and using the above expression, the refractive index dispersion of the sample liquid can in principle be obtained.

For the purpose of experimentally demonstrating this method, several guided mode resonance filters of varying periods were fabricated using ion beam sputter deposition of titanium dioxide on a nanostructured low-index polymer substrate. The resonant reflection from each of these was measured as a function of period for several different superstrate liquids, including purified water. In all deposited films, a degree of thickness variation can be expected, and as it turns out, the refractive index as yielded by Eq. (5.2) is highly sensitive to the high-index thickness. Therefore, using the measured resonance wavelengths for purified water, a calibration curve of thickness t versus period Λ was generated, shown in Fig. 5.4(b). Using this calibration curve and the measured resonance wavelengths as a function of period, the refractive index dispersion for the remaining liquids was obtained using Eq. (5.2). Example results for the case of a microscope immersion oil are shown in Fig. 5.4(c), compared to reference data from the manufacturer. The paper shows that there is clear agreement between the dispersion results obtained by the presented method, and reference data.

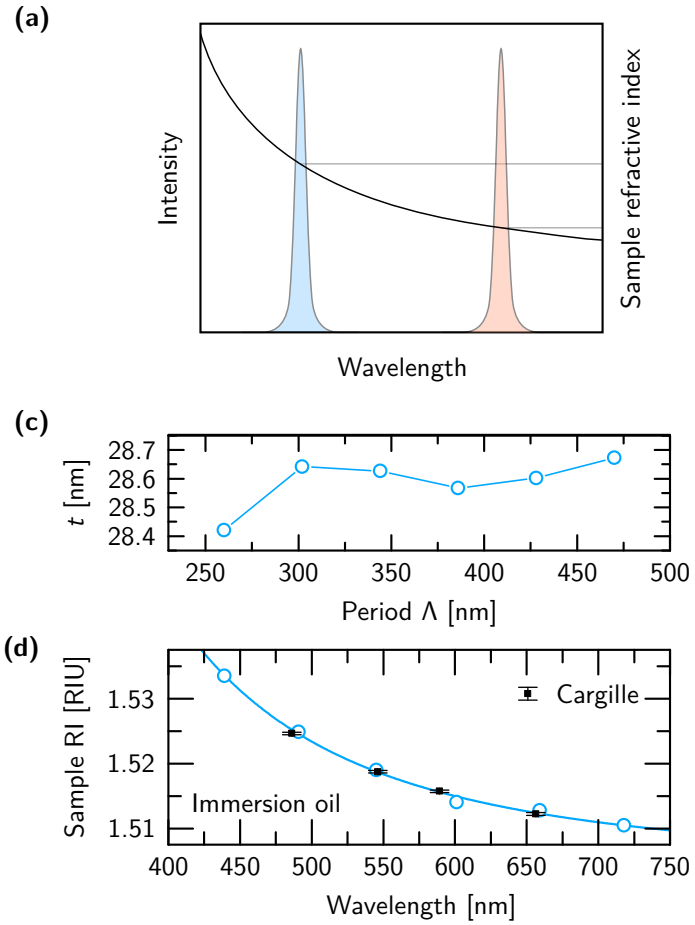

Figure 5.4: (a) An illustration demonstrating how an optical resonance effectively probes the refractive index of a sample liquid at the resonance wavelength. (b) A calibration curve of high-index layer thickness t versus grating period Λ, which is necessary to obtain accurate dispersion results using this method. (c) An example of an acquired dispersion profile using the presented method for the case of a microscope immersion oil. The obtained data are compared to reference values given by the manufacturer.

Further discussion

Although the presented method has yet to be shown to achieve the same level of accuracy as e.g. the Newton-Fraunhofer method, it has several advantages over existing methods for measuring refractive index dispersion. As noted earlier, it requires very little sample liquid to operate, with the possibility for further reduction by implementing a microfluidic system to bring the liquids to the guided mode resonance filters. This small volume require-

ment can be an advantage if the liquid in question is expensive to synthesize. Furthermore, the thermo-optic coefficient of common liquids such as water, ethanol, and glycerol are in the range $1 \times 10^{-4} - 5 \times 10^{-4}$ RIU, illustrating the need for temperature stabilization, and the smaller the volume is, the quicker it can be stabilized. The number of wavelengths that approaches such as the Newton-Fraunhofer method can measure at is limited by the light source used. In contrast, the presented method can measure at an arbitrary number of wavelengths, depending on the number of distinct periods in the array. Another feature of this method which lends itself well to rapid dispersion measurements is its ability to measure at multiple wavelengths simultaneously by illuminating the entire array and measuring all the individual resonance wavelengths at once with a spectrometer. The presented method requires that the dispersion of the materials from which the guided mode resonance filter array is composed is known, as well as an initial calibration step with respect to a liquid of known dispersion, but this may be easily automated using a commonly available liquid such as purified water.

5.4 Paper I

Absolute analytical prediction of photonic crystal guided mode resonance wavelengths

Absolute analytical prediction of photonic crystal guided mode resonance wavelengths

Pétur Gordon Hermannsson,[1] Christoph Vannahme,[1] Cameron L.C. Smith,[1] and Anders Kristensen[1, a)]
Department of Micro- and Nanotechnology, Technical University of Denmark, Ørsteds Plads, Building 345E, DK-2800 Kgs. Lyngby, Denmark

(Dated: 30 June 2015)

A class of photonic crystal resonant reflectors known as guided mode resonant filters are optical structures that are widely used in the field of refractive index sensing, particularly in biosensing. For the purposes of understanding and design, their behavior has traditionally been modeled numerically with methods such as rigorous coupled wave analysis. Here it is demonstrated how the absolute resonance wavelengths of such structures can be predicted by analytically modeling them as slab waveguides in which the propagation constant is determined by a phase matching condition. The model is experimentally verified to be capable of predicting the absolute resonance wavelengths to an accuracy of within 0.75 nm, as well as resonance wavelength shifts due to changes in cladding index within an accuracy of 0.45 nm across the visible wavelength regime in the case where material dispersion is taken into account. Futhermore, it is demonstrated that the model is valid beyond the limit of low grating modulation, for periodically discontinuous waveguide layers, high refractive index contrasts and highly dispersive media.

Guided mode resonance filters (GMRFs) are a class of photonic crystal resonant reflectors that exhibit perfect resonant reflection of arbitrarily narrow wavelength bands for certain polarizations of out-of-plane incident light, while allowing the compliment of the spectrum to be transmitted. This effect was initially described theoretically for grating waveguides in which the refractive index of the core varies periodically in the guiding direction[1–3], but occurs similarly in waveguide structures where the thickness of the core varies periodically[4,5]. Numerous applications for GMRF structures have been proposed and demonstrated, such as laser cavity mirrors[2,3], wave plates[6], angle tunable filters[7], and photonic crystal enhanced microscopy[8]. The resonantly reflected wavelength band is typically highly sensitive to refractive index changes in the cladding regions, making GMRFs ideal for optical[9,10] or voltage-tunable filters[11]. Furthermore, this sensitivity, combined with the fact that these structures can be quickly and inexpensively fabricated from biocompatible materials, has lead to their widespread adoption in various environmental[12] and biological sensing applications[13–16].

When a GMRF is illuminated with polarized broadband light, part of the light is transmitted while part of it is coupled into waveguide modes. Due to the presence of the grating, these modes are continually de-coupled out of the waveguide as they propagate, and are thus referred to as being leaky. At a certain resonance wavelength λ_{GMR}, complete destructive interference occurs between the de-coupled light and the directly transmitted light, leading to resonant reflection[4]. In GMRFs in which the grating period is sufficiently small, resonant reflection with a 100% reflection efficiency can occur[3]. Depending on whether the incident light is polarized perpendicular or in parallel to the grating direction, leaky transverse electric (TE) or transverse magnetic (TM) waveguide modes will be excited. Since TE and TM modes are governed by different mode conditions, resonant reflection associated with each mode inherently occurs at different wavelengths, enabling GMRFs to be used as wavelength-selective polarizers[2].

In this paper an analytical model for predicting the absolute resonance wavelengths of GMRFs is presented and experimentally verified against a nanoreplicated, polymer-based structure. When material dispersion is taken into account, the method is shown to predict the absolute resonance wavelengths to an accuracy of within 0.75 nm, and resonance wavelength shifts due to refractive index changes in the cladding to within 0.45 nm, across the entire visible wavelength regime. The concept of this model has previously been advanced for the limit of low grating modulation[1,3], but is shown here to be valid beyond this limit for GMRFs with periodically discontinuous waveguide layers, high refractive index contrasts and highly dispersive media.

The particular GMRF structure of interest is shown schematically in Fig. 1a. It is a three layer dielectric grating waveguide composed of an optically infinite substrate of refractive index n_1 whose surface height is periodically modulated with a period of Λ, supporting a guiding layer (n_2) of constant thickness t which in turn is covered by a superstrate material (n_3) that fills the grating grooves. The guiding layer may potentially be discontinuous, such that its thickness t is smaller than the grating height modulation h.

This system is modeled as a three layer dielectric slab waveguide where the propagation constant β must fulfill the following phase matching condition for coupling light incident at an angle of θ into a guided mode[5]:

$$\beta = K \pm k_0 n_1 \sin\theta \tag{1}$$

where $K = 2\pi/\Lambda$ and $k_0 = 2\pi/\lambda$. Fig. 1b illustrates this

a)anders.kristensen@nanotech.dtu.dk

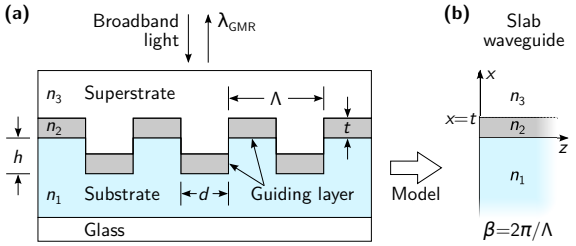

FIG. 1. (a) Schematic diagram of the GMRF, and (b) how it is modeled as a slab waveguide with a constraint placed upon the propagation constant β.

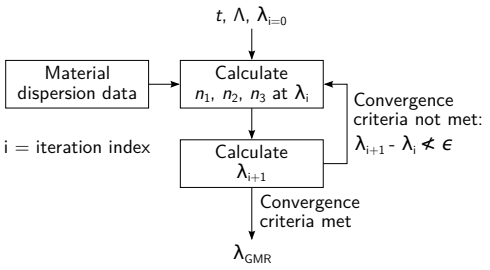

FIG. 2. The iterative approach used for calculating the guided mode resonance wavelengths λ_{GMR}, using measured material dispersion data.

concept for the case of normal incidence. Even though the principle applies to both TE and TM modes, here the discussion will be limited to TE modes only, for the sake of brevity. For TE guided modes in an asymmetric slab waveguide, the following mode condition must apply[17]:

$$\tan p_2 t = \frac{p_1 + p_3}{p_2 - p_1 p_3 / p_2} \tag{2}$$

where $p_j = \sqrt{(-1)^{j+1}\left(\beta^2 - n_j^2 k_0^2\right)}$ and j denotes layer index. In the case where material dispersion is ignored, calculating the resonance wavelength λ_{GMR} using this model is straight forward. For a given structure, Λ, t, and n_{1-3} are known constants, and eq. 2 can be solved numerically for k_0, yielding the resonance wavelength via $\lambda_{\mathrm{GMR}} = 2\pi/k_0$. If the wavelength dependence of the refractive indices can be accurately expressed by an analytical function of λ, material dispersion may be accounted for by setting $n_j \to n_j(\lambda)$. Alternatively, if such a function is unavailable or it is more convenient to use sets of measured refractive index and wavelength pairs (e.g. obtained by ellipsometry, etc.) an iterative approach such as the one illustrated in Fig. 2 is more suitable. Starting with an initial guess wavelength $\lambda_{\mathrm{i}=0}$, the refractive indices n_{1-3} are calculated from the dispersion data at this starting wavelength using interpolation. From there, a new resonance wavelength $\lambda_{\mathrm{i}+1}$ is calculated as before, and this process repeated until the calculated wavelength has converged on a value within a given tolerance ϵ, such that $\lambda_{\mathrm{i}+1} - \lambda_{\mathrm{i}} < \epsilon$, at which point the GMR wavelength becomes $\lambda_{\mathrm{GMR}} = \lambda_{\mathrm{f}}$, the final wavelength. The present work makes exclusive use of the iterative method.

For the purpose of verifying the model, GMRF samples consisting of a low refractive index polymer substrate (Efiron PC-409, SSCP Co., Ltd) and a $t = 28$ nm thick titanium dioxide guiding layer were fabricated using nanoreplication[13]. The grating fields were $1{\times}1$ mm^2 in size, each with a period in the range $\Lambda = (260 - 470)$ nm, a duty cycle of $d/\Lambda = 25\%$ and a grating protrusion height of $h = 100$ nm. Note that the GMRF samples thus had a discontinuous guiding layer, as $t < h$. The dispersion profiles of each of the materials and the guiding layer thickness were obtained using spectroscopic ellipsometry. The fabrication and material characterization are discussed in more detail in the supplementary material[18].

Utilizing the fact that GMRFs essentially behave as wavelength-selective polarizers, the resonance spectra of the fabricated GMRF samples were measured in transmission by placing them between two crossed polarizers[15], as shown in Fig. 3a. In this setup, only light in the resonance bands is transmitted, while the remainder of the spectrum is blocked. Here, broadband light is guided from its source, a Xenon lamp (Ocean Optics HPX-2000) via an optical fiber, and then collimated with a fiber collimator (A), before being polarized with a linear polarizer (B) at an angle of $\phi = 45°$ w.r.t. the sample grating direction. In order to limit the angles of incidence, an aperture (C) is placed adjacent to the sample surface. The sample (D) is mounted on a combined 3-axis translation and goniometer stage and positioned such that the broadband light is normally incident on the GMRF surface, $\theta = 0°$. In the resonance bands, the GMRF reflects a component of the light leading to an effective rotation in polarization, which in turn enables partial transmission through the second polarizer (E, $\phi = -45°$), while the rest of the spectrum is blocked. A lens (F) focuses the transmitted light into an optical fiber which leads it to a spectrometer for analysis (Jaz, Ocean Optics). Fig. 3b illustrates the polarization and intensity I of the light between each of the optical components for the cases where light is at the TE resonance wavelength and when it is not. Fig. 3c shows the light intensity as a function of wavelength before and after it passes through the second polarizer (E) and illustrates how the light off-resonance is filtered out, resulting in a measured spectrum characterized by a peak at the resonance wavelength.

Resonance spectra were acquired for each grating period Λ for four different superstrate materials of known refractive index dispersion: air, deionized water at 20°C, and the index matching oils Cargille AAA 1.3850 and A 1.4900 (Cargille Labs). Several of the aquired spectra are shown in Fig. 4. It is worth noting that despite the discontinuous nature of the guiding layer, the devices under study still support guided mode resonant reflection. In the case of an air superstrate, the guiding layer thick-

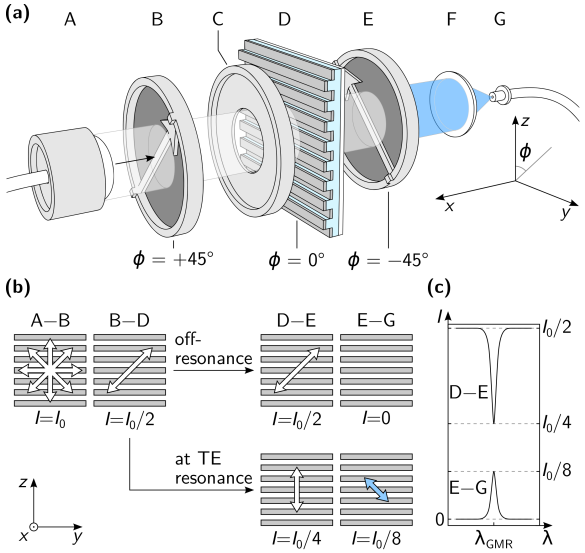

FIG. 3. (a) Experimental setup for measuring the resonance wavelengths of GMRFs in transmission. Here, broadband light is collimated (A) and polarized (B) at an angle $\phi = +45°$ w.r.t. the grating direction, then passes through an aperture (C) and strikes the GMRF (D) at normal incidence. Non-resonant light is blocked by a second polarizer (E) oriented orthogonally w.r.t. the first, $\phi = -45°$, and a lens (F) focuses the remaining light into a fiber (G) where it is guided to a spectrometer. (b) A flowchart illustrating the polarization and relative intensity of light between each of the optical components. The horizontal gray lines denote the grating lines. (c) The intensity of light I as a function of wavelength λ before and after passing through the second polarizer (E).

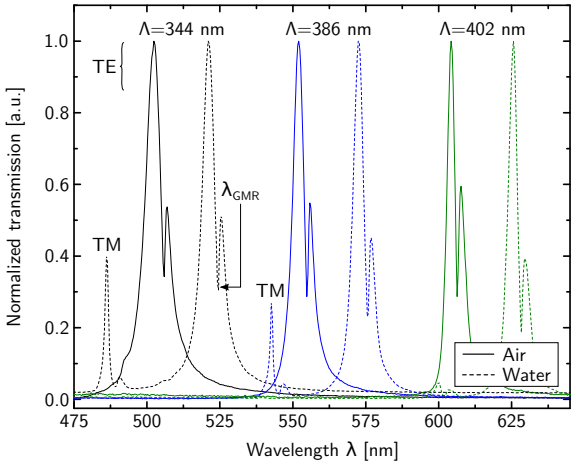

FIG. 4. Normalized transmission spectra obtained in transmission for GMRFs composed of a polymer substrate with a periodic surface height modulation supporting a $t = 28$ nm thick TiO_2 guiding layer with either air (solid) or deionized water at 20°C (dashed) as the superstrate for three different grating periods Λ.

ness is below cut-off for TM modes, and only resonance peaks due to TE leaky modes are observed. However, with a water superstrate, the more symmetric cladding conditions allow for TM modes to exist, and both TE and TM associated resonance peaks are observed, separated in wavelength. Furthermore, even though normally incident broadband light should theoretically result in a single resonance peak for each mode, in practice due to e.g. the angle of incidence deviating from normal, imperfections or asymmetries in the grating structure and non-plane-wave incident light, the peak is split at the resonance wavelength λ_{GMR}, characterized by a notch or dip[19]. For each of the measured resonance peaks a Lorentzian curve was fitted to the split notch in order to obtain the wavelength of the notch minima, and thereby the resonance wavelength λ_{GMR}.

Simulating the experimental conditions above, the presented model was used to calculate the resonance wavelength λ_{GMR} due to TE modes excited at normal incidence $\theta = 0°$ as a function of grating period Λ. This was performed for each of the four superstrates listed above, taking the dispersion of all materials into account. The model calculations used the experimentally acquired dispersion profiles for the polymer and guiding layer materials and the known dispersion profile for deionized water[20] at 20°C, whereas the two index matching oils were treated as Cauchy liquids with the relevant coefficients provided by the manufacturer[18]. The calculations were repeated for the case where dispersion is ignored, with all refractive indices fixed at their respective values at $\lambda = 550$ nm. Furthermore, the resonance wavelength shift $\Delta\lambda_{GMR}$ that occurs when replacing air as a superstrate with each of the three liquids was calculated for the same two cases.

The model results are compared to the experimentally obtained values in Fig. 5. Here, the error bars denote the standard deviation of the sum of the following sources of uncertainty: Lorentz fitting of split notches, spectrometer uncertainty, and half a free spectral range of Fabry-Perot fringes which were overlayed onto the measured resonance spectra owing to the presence of the glass wafer supporting the GMRF samples. The uncertainty of the spectrometer was characterized over the entire visible spectrum by comparison to a known calibration source; a mercury-argon lamp.

In the case where material dispersion is accounted for, the model is able to accurately predict the absolute resonance wavelengths to within 0.75 nm over the entire visible spectrum for all periods and superstrate materials, with a mean difference between model and experiment of 0.22 nm. Similarly, wavelength shifts due to changes in superstrate refractive index are predicted to within 0.43 nm of the measured values, with an average difference of 0.18 nm. In the case where material dispersion is ignored, the discrepancy between model and experiment is as high as 19.9 nm for absolute resonance wavelengths and 6.1 nm for resonance shifts, highlighting the importance of not disregarding the effects of refractive index dispersion in the context of simulating optical structures.

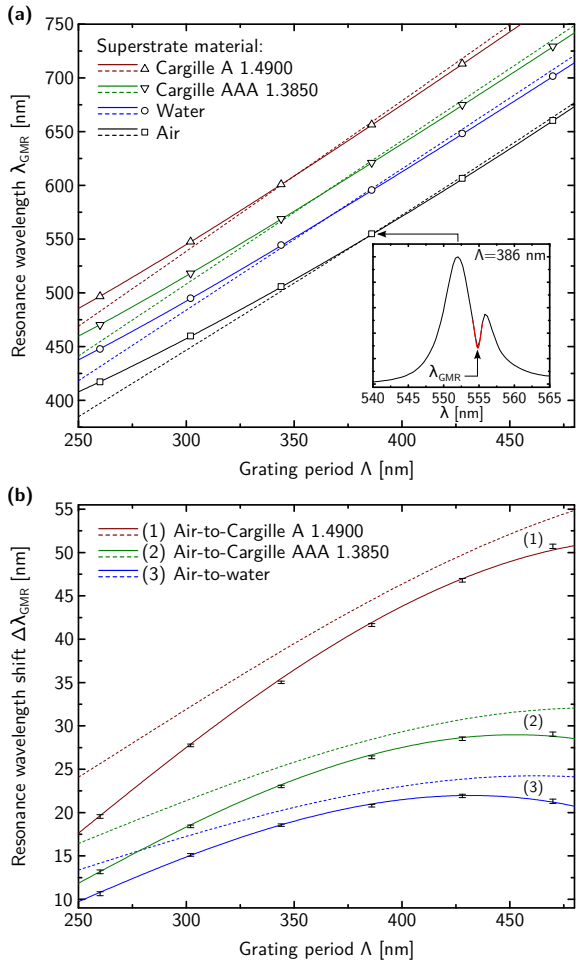

FIG. 5. (a) The location of the guided mode resonances λ_{GMR} for a $t = 28$ nm thick TiO_2 guiding layer on a polymer substrate with a periodic surface height modulation for several different superstrate materials as a function of grating period. The solid lines denote model results where material dispersion is included, the dashed lines model results when dispersion is ignored, and the points denote measured resonance wavelengths. The inset shows a single measured resonance peak with the split notch fitted with a Lorentzian curve and the λ_{GMR} highlighted. Each of the curve groups in ascending order have been shifted by 0, 20, 40 and 60 nm, respectively, for clarity. (b) The resonance shift $\Delta\lambda_{\mathrm{GMR}}$ due to the replacement of air as a superstrate with each of the three liquids.

In summary, an analytical model capable of accurately predicting the absolute resonance wavelengths of guided mode resonance filters and the resonance shifts due to changes in superstrate refractive index has been demonstrated. The model is shown to be accurate beyond the limit of low grating modulation for GMRFs with periodically discontinuous waveguide layers, high refractive index contrasts and highly dispersive media. Despite only yielding the resonance wavelength and not the spectral shape of the resonance, this method has the advantage over methods such as rigorous coupled wave analysis, etc. in that it is conceptually simple and can be simply adapted to include the effects of material dispersion for enhanced accuracy. Furthermore, it is computationally cheap and easily implementable. It is thus a convenient engineering tool for structural design, especially when the resonance location is paramount, e.g. in wavelength selective laser cavity mirrors, or sensitivity optimization in e.g. sensor development. For applications such as biosensor optimization, where refractive index changes close to the sensor surface as opposed to changes in the superstrate bulk refractive index are to be detected, the model can be extended to e.g. a four layer waveguide[21], in a straight-forward manner with an additional layer atop the waveguide core representing the biofilm or analyte to be detected.

ACKNOWLEDGMENTS

P.G.H. acknowledges support from the Strategic Research Center PolyNano (10-092322). C.V. and C.L.C.S. acknowledge support from the Danish Research Council for Technology and Production Sciences (Grant Nos. 12-126676 and 12-126601).

[1] S. S. Wang, R. Magnusson, J. S. Bagby, and M. G. Moharam, J. Opt. Soc. Am. A **7**, 1470 (1990).
[2] R. Magnusson and S. S. Wang, Appl. Phys. Lett. **61**, 1022 (1992).
[3] S. S. Wang and R. Magnusson, Appl. Opt. **32**, 2606 (1993).
[4] D. Rosenblatt, A. Sharon, and A. A. Friesem, IEEE J. Quantum Electron. **33**, 2038 (1997).
[5] A. Sharon, D. Rosenblatt, and A. A. Friesem, J. Opt. Soc. Am. A **14**, 2985 (1997).
[6] R. Magnusson, M. Shokooh-Saremi, and E. G. Johnson, Opt. Lett. **35**, 2472 (2010).
[7] M. J. Uddin and R. Magnusson, IEEE Photon. Technol. Lett. **24**, 1552 (2012).
[8] Y. Zhuo, H. Hu, W. Chen, M. Lu, L. Tian, H. Yu, K. D. Long, E. Chow, W. P. King, S. Singamaneni, and B. T. Cunningham, Analyst **139**, 1007 (2014).
[9] D. W. Dobbs and B. T. Cunningham, Appl. Opt. **45**, 7286 (2006).
[10] F. Yang, G. Yen, G. Rasigade, J. A. Soares, and B. T. Cunningham, Appl. Phys. Lett. **92**, 091115 (2008).
[11] F. Yang, G. Yen, and B. T. Cunningham, Appl. Phys. Lett. **90**, 261109 (2007).
[12] K. J. Lee, D. Wawro, P. S. Priambodo, and R. Magnusson, IEEE Sensors J. **7**, 409 (2007).
[13] B. T. Cunningham, B. Lin, J. Qiu, P. Li, J. Pepper, and B. Hugh, Sensor. Actuat. B-Chem. **85**, 219 (2002).
[14] B. T. Cunningham, J. Qiu, P. Li, and B. Lin, Sensor. Actuat. B-Chem. **87**, 365 (2002).
[15] Y. Nazirizadeh, U. Bog, S. Sekula, T. Mappes, U. Lemmer, and M. Gerken, Opt. Express **18**, 19120 (2010).
[16] C. Ge, M. Lu, S. George, T. A. Flood Jr., C. Wagner, J. Zheng, A. Pokhriyal, J. G. Eden, P. J. Hergenrother, and B. T. Cunningham, Lab Chip **13**, 1247 (2013).
[17] A. Yariv and P. Yeh, *Photonics, 6th ed.* (Oxford University Press, New York, Oxford, 2006) p. 848.
[18] See supplementary material at [URL will be inserted by AIP] for fabrication, material characterization and material properties.
[19] R. Magnusson, S. S. Wang, T. D. Black, and A. Sohn, IEEE Trans. Antennas Propag. **42**, 567 (1994).
[20] M. Daimon and A. Masumura, Appl. Opt. **46**, 3811 (2007).
[21] C. Vannahme, C. L. C. Smith, M. B. Christiansen, and A. Kristensen, Appl. Phys. Lett. **101**, 151123 (2012).

Absolute analytical prediction of photonic crystal guided mode resonance wavelengths - Supplementary material

Pétur Gordon Hermannsson, Christoph Vannahme, Cameron L.C. Smith, and Anders Kristensen[a)]
Department of Micro- and Nanotechnology, Technical University of Denmark, Ørsteds Plads, Building 345E, DK-2800 Kgs. Lyngby, Denmark

SUPPLEMENTARY MATERIAL

For the purpose of verifying the model, GMRF structures were fabricated using UV nanoreplication[1]. An anti-stiction coated silicon master was fabricated using standard electron beam lithography techniques, and contained several 1×1 mm^2 grating fields with six periods equispaced in the range 260-470 nm, each with a duty cycle of $d/\Lambda = 25\%$ and a grating protrusion height of $h = 100$ nm. A droplet of UV curable, solvent free, low refractive index polymer (Efiron PC-409, SSCP Co., Ltd) was dispensed onto the structured area of the master and covered with a glass wafer. The weight of the glass wafer along with capillary forces cause the polymer to spread out and distribute evenly between the master and glass wafer with a thickness of roughly 100 µm. After UV curing the polymer through the glass wafer, the master was removed, and the structured polymer surface covered with an ion-beam sputter deposited layer of titanium dioxide (Ionfab 300, Oxford Instruments).

The refractive index dispersion and thickness of the TiO_2 guiding layer was determined by variable angle spectroscopic ellipsometry (VASE, J.A. Woollam Co., Inc.) performed on a TiO_2 layer deposited onto a reflective silicon wafer in a process identical to the one described above. By fitting to a Tauc-Lorentz oscillator model[2], a film thickness of $t = 28$ nm was obtained, along with the dispersion profile shown in Fig. S1a. Note that the GMRF sample thus has a discontinuous guiding layer, as $t < h$. The dispersion of the polymer was measured analogously, however, since the viscosity of the polymer leads to film thicknesses greater than that which can be handled accurately by VASE, it was thinned in a compatible solvent (2-Butanone, Sigma-Aldrich Corp.) at a ratio of 1:5 before spinning it onto a silicon wafer wafer. The solvent was then subsequently removed via baking on a 100°C hotplate for 10 min and the polymer finally UV cured as before. This process resulted in a thin enough film to be measured by VASE, in which it was modeled as a Cauchy material, yielding the dispersion profile shown in Fig. S1b. The refractive index dispersion profiles of all the materials used in this work are shown in Fig. S1c.

In the experimental verification of the model, two index matching oils were used, and treated as Cauchy materials in the model calculations. The relevant Cauchy coefficients for these two materials are given in Table S1.

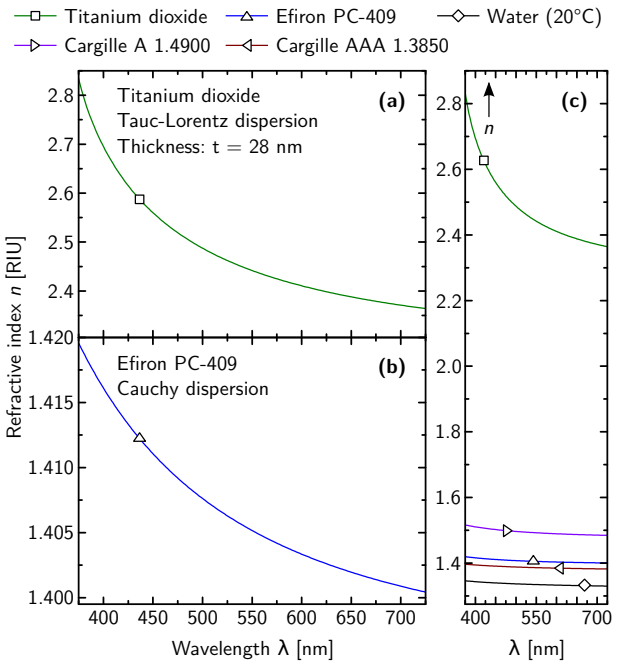

FIG. S1. The refractive index dispersion of (a) the titanium dioxide guiding layer and (b) the substrate polymer Efiron PC-409, as determined by variable angle spectroscopic ellipsometry. Panel (c) shows the dispersion of all the relevant materials on a single axis.

TABLE S1. Cauchy coefficients for the index matching oils used.

Material	A	B [nm^2]	C [nm^4]
AAA 1.3850	1.376592	2988.353	-23980360
A 1.4900	1.474492	5059.424	113226800

REFERENCES

[1] B. T. Cunningham, B. Lin, J. Qiu, P. Li, J. Pepper, and B. Hugh, Sensor. Actuat. B-Chem. **85**, 219 (2002).
[2] G. E. Jellison and F. A. Modine, Appl. Phys. Lett. **69**, 2137 (1996).

[a)] anders.kristensen@nanotech.dtu.dk

5.5 Paper II

All-polymer photonic crystal slab sensor

All-polymer photonic crystal slab sensor

Pétur G. Hermannsson,[1] Kristian T. Sørensen,[1] Christoph Vannahme,[1] Cameron L.C. Smith,[1] Jan J. Klein,[2] Maria-Melanie Russew,[2] Gabi Grützner,[2] and Anders Kristensen[1,*]

[1]*Department of Micro- and Nanotechnology, Technical University of Denmark, Ørsteds Plads, Building 345E, DK-2800 Kgs. Lyngby, Denmark*
[2]*micro resist technology GmbH, Köpenicker Straße 325, DE-12555 Berlin, Germany*
[*]*anders.kristensen@nanotech.dtu.dk*

www.nanotech.dtu.dk/ak

Abstract: An all-polymer photonic crystal slab sensor is presented, and shown to exhibit narrow resonant reflection with a FWHM of less than 1 nm and a sensitivity of 31 nm/RIU when sensing media with refractive indices around that of water. This results in a detection limit of 4.5×10^{-6} RIU when measured in conjunction with a spectrometer of 12 pm/pixel resolution. The device is a two-layer structure, composed of a low refractive index polymer with a periodically modulated surface height, covered with a smooth upper-surface high refractive index inorganic-organic hybrid polymer modified with ZrO_2-based nanoparticles. Furthermore, it is fabricated using inexpensive vacuum-less techniques involving only UV nanoreplication and polymer spin-casting, and is thus well suited for single-use biological and refractive index sensing applications.

OCIS codes: (130.5296) Photonic crystal waveguides; (130.5440) Polarization-selective devices; (050.6624) Subwavelength structures; (130.6010) Sensors; (220.0220) Optical design and fabrication.

References and links

1. S. S. Wang and R. Magnusson, "Theory and applications of guided-mode resonance filters," Appl. Opt. **32**, 2606–2613 (1993).
2. R. Magnusson, M. Shokooh-Saremi, and E. G. Johnson, "Guided-mode resonant wave plates," Opt. Lett. **35**, 2472–2474 (2010).
3. D. W. Dobbs and B. T. Cunningham, "Optically tunable guided-mode resonance filter," Appl. Opt. **45**, 7286–7293 (2006).
4. F. Yang, G. Yen, and B. T. Cunningham, "Voltage-tuned resonant reflectance optical filter for visible wavelengths fabricated by nanoreplica molding," Appl. Phys. Lett. **90**, 261109 (2007).
5. F. Yang, G. Yen, G. Rasigade, J. A. Soares, and B. T. Cunningham, "Optically tuned resonant optical reflectance filter," Appl. Phys. Lett. **92**, 091115 (2008).
6. M. J. Uddin and R. Magnusson, "Efficient guided-mode-resonant tunable color filters," IEEE Photonics Technol. Lett. **24**, 1552–1554 (2012).
7. M. J. Uddin, T. Khaleque, and R. Magnusson, "Guided-mode resonant polarization-controlled tunable color filters." Opt. Express **22**, 12307–15 (2014).
8. C. F. R. Mateus, M. C. Y. Huang, Y. Deng, A. R. Neureuther, and C. J. Chang-Hasnain, "Ultrabroadband mirror using low-index cladded subwavelength grating," IEEE Photonics Technol. Lett. **16**, 518–520 (2004).
9. K. J. Lee, D. Wawro, P. S. Priambodo, and R. Magnusson, "Agarose-gel based guided-mode resonance humidity sensor," IEEE Sens. J. **7**, 409–414 (2007).
10. I. W. Jung, B. Park, J. Provine, R. T. Howe, and O. Solgaard, "Monolithic silicon photonic crystal slab fiber tip sensor," in "IEEE/LEOS International Conference on Optical MEMS and Nanophotonics," (2009), pp. 19–20.

11. B. T. Cunningham, B. Lin, J. Qiu, P. Li, J. Pepper, and B. Hugh, "A plastic colorimetric resonant optical biosensor for multiparallel detection of label-free biochemical interactions," Sensors Actuators B Chem. **85**, 219–226 (2002).
12. Y. Nazirizadeh, U. Bog, S. Sekula, T. Mappes, U. Lemmer, and M. Gerken, "Low-cost label-free biosensors using photonic crystals embedded between crossed polarizers," Opt. Express **18**, 19120–19128 (2010).
13. O. Levi, M. M. Lee, J. Zhang, V. Lousse, S. R. J. Brueck, S. Fan, and J. S. Harris, "Sensitivity analysis of a photonic crystal structure for index-of-refraction sensing," Nanoscale Imaging, Spectrosc. Sensing, Actuation Biomed. Appl. IV **6447**, P4470 (2007).
14. L. L. Chan, S. L. Gosangari, K. L. Watkin, and B. T. Cunningham, "A label-free photonic crystal biosensor imaging method for detection of cancer cell cytotoxicity and proliferation," Apoptosis **12**, 1061–1068 (2007).
15. S. Kaja, J. D. Hilgenberg, J. L. Collins, A. A. Shah, D. Wawro, S. Zimmerman, R. Magnusson, and P. Koulen, "Detection of novel biomarkers for ovarian cancer with an optical nanotechnology detection system enabling label-free diagnostics," J. Biomed. Opt. **17**, 081412–1 (2012).
16. W. Chen, K. D. Long, M. Lu, V. Chaudhery, H. Yu, J. S. Choi, J. Polans, Y. Zhuo, B. A. C. Harley, and B. T. Cunningham, "Photonic crystal enhanced microscopy for imaging of live cell adhesion," Analyst **138**, 5886–5894 (2013).
17. Y. Nazirizadeh, J. Reverey, U. Geyer, U. Lemmer, C. Selhuber-Unkel, and M. Gerken, "Material-based three-dimensional imaging with nanostructured surfaces," Appl. Phys. Lett. **102**, 011116 (2013).
18. S. Fan and J. D. Joannopoulos, "Analysis of guided resonances in photonic crystal slabs," Phys. Rev. B **65**, 235112 (2002).
19. T. Khaleque, M. J. Uddin, and R. Magnusson, "Design and fabrication of broadband guided-mode resonant reflectors in TE polarization." Opt. Express **22**, 12349–58 (2014).
20. C. Ge, M. Lu, S. George, T. A. Flood Jr., C. Wagner, J. Zheng, A. Pokhriyal, J. G. Eden, P. J. Hergenrother, and B. T. Cunningham, "External cavity laser biosensor," Lab Chip **13**, 1247–1256 (2013).
21. S. S. Wang, R. Magnusson, J. S. Bagby, and M. G. Moharam, "Guided-mode resonances in planar dielectric-layer diffraction gratings," J. Opt. Soc. Am. A **7**, 1470–1474 (1990).
22. D. Rosenblatt, A. Sharon, and A. A. Friesem, "Resonant grating waveguide structures," IEEE J. Quantum Electron. **33**, 2038–2059 (1997).
23. Y. Nazirizadeh, U. Lemmer, and M. Gerken, "Experimental quality factor determination of guided-mode resonances in photonic crystal slabs," Appl. Phys. Lett. **93**, 261110 (2008).
24. A. Yariv and P. Yeh, *Photonics: Optical Electronics in Modern Communications, 6th edition* (Oxford University Press, 2006).
25. A. Sharon, D. Rosenblatt, and A. A. Friesem, "Resonant grating–waveguide structures for visible and near-infrared radiation," J. Opt. Soc. Am. A **14**, 2985–2993 (1997).
26. T. Khaleque, H. G. Svavarsson, and R. Magnusson, "Fabrication of resonant patterns using thermal nano-imprint lithography for thin-film photovoltaic applications," Opt. Express **21**, A631–641 (2013).
27. Y. Nazirizadeh, F. von Oertzen, K. Plewa, N. Barié, P.-J. Jakobs, M. Guttmann, H. Leiste, and M. Gerken, "Sensitivity optimization of injection-molded photonic crystal slabs for biosensing applications," Opt. Mater. Express **3**, 556–565 (2013).
28. Y. Zhuo, H. Hu, W. Chen, M. Lu, L. Tian, H. Yu, K. D. Long, E. Chow, W. P. King, S. Singamaneni, and B. T. Cunningham, "Single nanoparticle detection using photonic crystal enhanced microscopy," Analyst **139**, 1007–1015 (2014).
29. P. G. Hermannsson, C. Vannahme, C. L. C. Smith, and A. Kristensen, "Absolute analytical prediction of photonic crystal guided mode resonance wavelengths," Appl. Phys. Lett. **105**, 071103 (2014).
30. T. Tamir and S. Peng, "Analysis and design of grating couplers," Appl. Phys. **14**, 235–254 (1977).
31. I. M. White and X. Fan, "On the performance quantification of resonant refractive index sensors," Opt. Express **16**, 1020–1028 (2008).

1. Introduction

Optical resonant gratings based on guided mode resonance (GMR) have proven to be a versatile tool within the field of applied optics. In addition to providing means for novel optical elements, such as wavelength selective mirrors, polarizers [1], waveplates [2], tunable filters [3–7] and ultrabroadband mirrors [8], such resonant gratings have increasingly found their way into a myriad of different sensing applications, such as chemical and environmental sensing [9, 10], label-free biosensing [11–13], cancer screening [14, 15], photonic crystal enhanced microscopy [16] and three dimensional imaging [17]. These resonant gratings, referred to here as photonic crystal slabs (PCS) [18], but also known as guided mode resonance filters or reflectors [1, 19] and photonic crystal resonant reflectors [20] in the literature, are essentially slab waveguides

in which the high refractive index waveguide core is in some way periodically modulated, such as by refractive index or thickness, and surrounded by cladding media of lower refractive indices [1, 18]. The periodically modulated waveguide core is able to sustain quasi-guided or leaky waveguide modes, which couple to the far field [21]. When under the illumination of out-of-plane incident light, these quasi-guided modes can be excited within the core. However, due the periodic nature of the core, the light in these modes is continually de-coupled out of the structure where it interferes with both the transmitted and reflected light. At a certain resonance wavelength, the de-coupled light interferes destructively with the transmitted light, resulting in highly efficient resonant reflection for a given wavelength interval [22]. The linewidth, i.e. quality factor, of the reflected interval depends on the rate of de-coupling (lifetime) of the quasi-guided mode, with lower rates of de-coupling (longer lifetimes) leading to narrower linewidths [18, 23, 24]. When the period of the modulation is smaller than the wavelength of the incident light, reflection efficiencies of up to 100% are predicted by theory, but due to factors such as material absorption and fabrication imperfections, the reflection efficiency is reduced. The incident light can excite both transverse-electric (TE) and transverse-magnetic (TM) modes, depending on whether the polarization is perpendicular to or parallel to the grating direction, respectively. Analogously to unmodulated slab waveguides, the intensity of the quasi-guided modes reaches maximum within the waveguide core, and decays exponentially into the cladding regions. Any change in refractive index that occurs in the cladding leads to a change in the guided mode, which manifests itself as a wavelength shift of the resonantly reflected interval. As an example, in label-free biosensing, analytes are immobilized at the waveguide surface, and the evanescent field of the waveguide mode can be used to selectively probe the change in refractive index which occurs on immobilization.

PCSs are commonly fabricated by patterning a low refractive index substrate material by either direct photo- or electron beam lithography [7, 25], or by replication, such as nanoimprint lithography [26], nanoreplication [11] or injection molding [27]. This is then typically followed by the deposition of a layer of a high refractive index material, such as titanium dioxide [28], tantalum pentaoxide [17] or silicon nitride [7, 11], all of which require a vacuum-deposition process.

In this paper, an all-polymer PCS sensor fabricated in a vacuum-less process using UV nanoreplication and polymer spin-casting is presented, which exhibits sharp resonant reflection with a low detection limit and a flat sensing surface. Due to the inexpensive fabrication cost of this PCS sensor, it is highly suitable for high throughput industrial production, and thus ideal for single-use biological and refractive index sensing applications.

2. Device and concept

The polymer PCS investigated here is shown schematically in Fig. 1. It comprises a low refractive index polymer (n_L, LRI) with a periodic surface height modulation of t_g, period $\Lambda = 384$ nm, protrusion duty cycle d, and is covered with a high refractive index polymer (n_H, HRI) which fills the grooves and serves as the waveguide layer. The surface of the HRI layer is at a distance t_f from the LRI polymer and is exposed to a superstrate of bulk refractive index n, referred to here as the sensing region. When illuminated from below with broadband light at normal incidence, the PCS sensor will reflect a narrow wavelength peak corresponding to the refractive index of the medium in the sensing region.

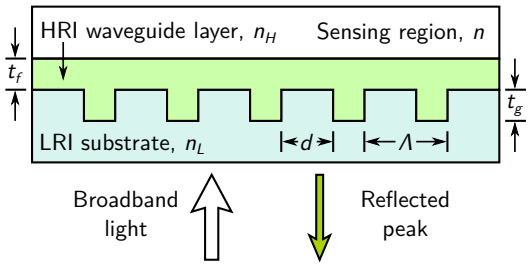

Fig. 1. A schematic illustration of the polymer photonic crystal slab sensor. The device is composed of a low refractive index polymer with a periodically modulated surface height, covered with a layer of the high refractive index polymer OrmoClear® HI01 XP, which in turn is exposed to a sensing region with a bulk refractive index of n.

The peak wavelengths of the resonant reflections can be calculated using an iterative computational model, in which the PCS is modeled as a slab waveguide with an effective core thickness t, where the propagation constant is set to the second order Bragg condition [29]:

$$\beta = 2\pi/\Lambda \tag{1}$$

For TE-polarized guided modes in an asymmetric dielectric slab waveguide, the following mode condition must be satisfied [24]:

$$\tan(ht) = \frac{p+q}{h(1-pq/h^2)} \tag{2}$$

where

$$h = \sqrt{n_H^2 k_0^2 - \beta^2}, \qquad q = \sqrt{\beta^2 - n^2 k_0^2}, \qquad p = \sqrt{\beta^2 - n_L^2 k_0^2}. \tag{3}$$

By solving Eq. (1)-(3) for k_0, the resonance wavelength λ_R can then be obtained via $\lambda_R = 2\pi/k_0$. In order to obtain the most accurate results, this approach requires that the dispersion of the materials comprising the PCS be taken into account, using e.g. an iterative approach as discussed in Ref. [29]. The dispersion profiles of the LRI and HRI polymers were thus measured using variable angle spectroscopic ellipsometry, the results of which are shown in Fig. 2(a). Using this data and the model described above, the resonance wavelength λ_R of reflected peaks associated with TE-polarized modes was calculated as a function of refractive index in the sensing region n and waveguide layer thickness t. For each given effective thickness t, the resonance shift with respect to air $(n = 1)$ was calculated as a function of n via

$$\Delta\lambda_R(n,t) = \left[\lambda_R(n) - \lambda_R(n=1)\right]_t \tag{4}$$

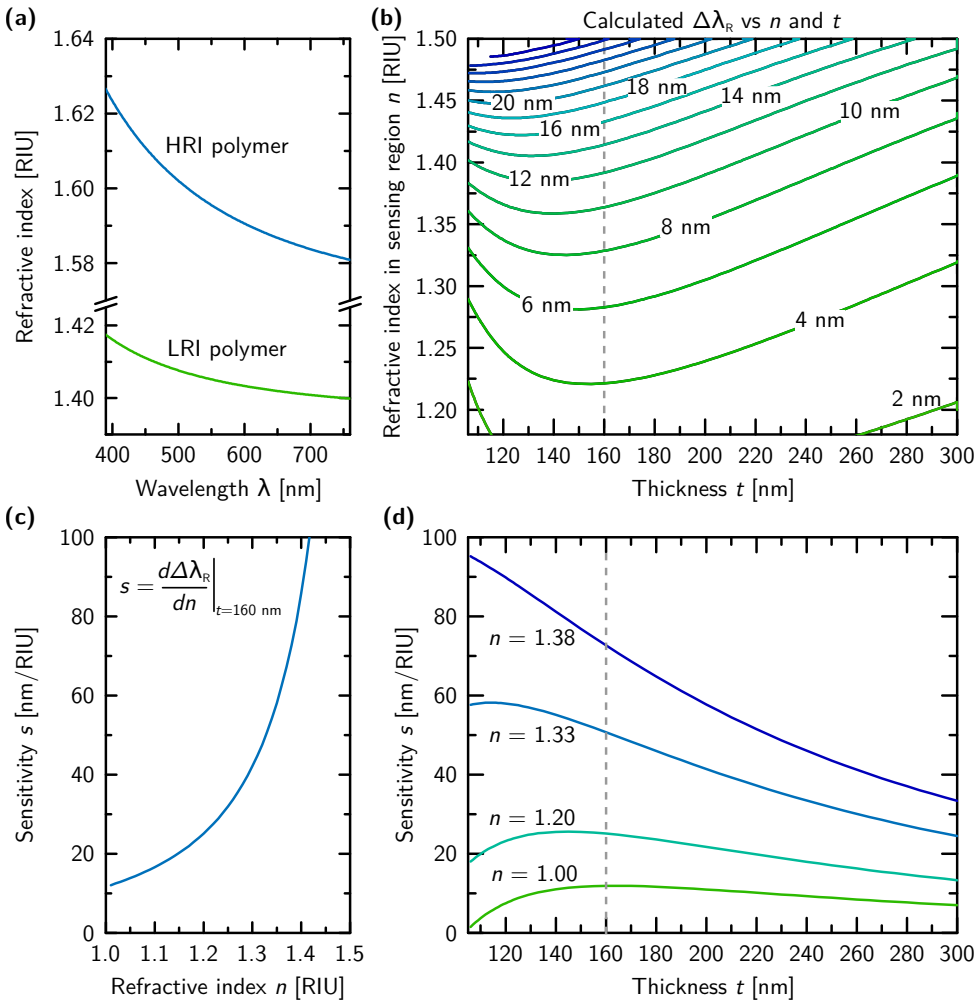

Fig. 2. (a) The refractive index dispersion of the two polymers from which the PCS sensor is made: Efiron PC-409 (LRI), and OrmoClear® HI01 XP (HRI). (b) The calculated resonance peak shift associated with TE-polarized guided modes as a function of effective waveguide thickness t and sensing region refractive index n. (c) An example of a calculated resonance peak sensitivity for the case of $t = 160$ nm, obtained along the dashed line in panel (b). (d) The calculated sensitivity of resonance peaks associated with TE-polarized modes for four different refractive indices n in the PCS sensing region.

The results are shown in Fig. 2(b). From this data, the sensitivity of the device, as defined by

$$s = \left. \frac{d\Delta\lambda_{\mathrm{R}}}{dn} \right|_{t} \tag{5}$$

was calculated as a function of refractive index in the sensing region n. Figure 2(c) shows an example of this for the case of $t = 160$ nm, obtained along the dashed line in Fig. 2(b). Figure 2(d) shows the calculated sensitivity as a function of t for four different sensing region refractive indices. When exposed to air ($n = 1.0$), the minimum effective waveguide layer thickness capable of sustaining a guided mode and thus exhibiting resonant reflection is $t = 106$ nm. For the case of water ($n = 1.33$) the minimum thickness is $t = 64$ nm, and the sensitivity takes a maximum of $s = 58$ nm/RIU at a thickness of $t = 114$ nm. The sensitivity curve for water is quite tolerant to changes in effective waveguide thickness, varying only by a factor of two in the interval $t = (100 - 250)$ nm. Refractive indices between $n = 1.33$ and $n = 1.38$ are of particular interest, as most biosensing takes place in this refractive index range, typically in aqueous solutions containing cells, proteins, etc. Here, the presence of biological agents or the occurrence of biological events is typically associated with very small changes in refractive index, highlighting the importance of understanding how the sensitivity of PCS sensors varies with refractive index n and how it can be optimized by tuning the waveguide layer thickness t.

Since the thickness of the HRI layer in the PCS sensor varies periodically in the guiding direction, it cannot be described directly by the model's effective thickness parameter t, which is constant. However, t can be estimated by the grating's modulation height t_g and film thickness t_f via $t = at_f + b(t_f + t_g)$, where $a, b \in]0,1[$ are constants that depend on the geometry and duty cycle of the grating. For example, for a perfect binary grating with a protrusion duty cycle d, $a = d$ and $b = (1 - d)$. In general, $t > t_f$, and thus measurements will correspond to the model for values of t greater than t_f. However, as a tool to guide the fabrication of the polymer PCS sensor, it is clear from the simulation results in Fig. 2(d) that the sensor exhibits optimum sensitivity for aqueous and biological sensing applications for film thicknesses t_f of the order of 100 nm, and then drops off monotonously with increasing thickness.

3. Device fabrication and characterization

The polymer PCS sensor was fabricated by UV nanoreplication and polymer spin-casting, as shown in Fig. 3. A silicon master was patterned by electron beam lithography and contained a 2×2 mm one-dimensional, linear grating area with a period of $\Lambda = 384$ nm and a protrusion duty cycle of 25%. The master was anti-stiction coated with a thin layer of perfluorodecyltrichlorosilane (FDTS) using molecular vapor deposition. Placing the master face-up, a droplet of UV curable, low refractive index (LRI, 1.40 RIU at 589 nm), solvent-free polymer (Efiron PC-409, SSCP Co., Ltd.) was dispensed onto the structured area of the master. A borosilicate glass wafer was placed on top of the LRI polymer, sealing it between the master and the glass, where the joint effect of the weight of the glass and capillary forces caused the LRI polymer to spread out and form an even ~ 30 μm layer. After curing the LRI polymer with ultra-violet (UV) light through the glass, the stack was flipped over and the silicon master separated from the LRI polymer, leaving it on the glass. A solution of a high refractive index (HRI, 1.59 RIU at 589 nm) inorganic-organic hybrid polymer modified with ZrO_2-based nanoparticles (OrmoClear® HI01 XP, micro resist technology GmbH) in the polymer thinner ma-T 1050 (25% weight fraction) was prepared and spun onto the cured LRI surface at 2000 RPM, followed by a 10 minute bake-out at 100°C and 10 minutes of UV curing. Due to oxygen in the ambient atmosphere leading to partial quenching of the polymerization of the HRI polymer, a layer of uncured polymer at the surface was rinsed off with isopropanol. In order to estimate the HRI polymer thickness t_f, a silicon wafer was spun with the same HRI

polymer solution and processed identically, yielding a value of $t_f = 180$ nm as ascertained by ellipsometry and profilometry.

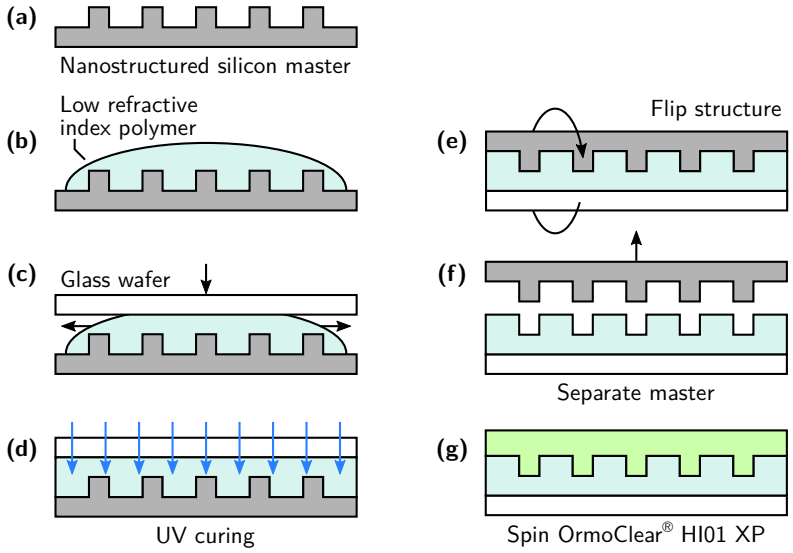

Fig. 3. Fabrication of the polymer PCS sensor. (a) Nanostructured silicon master. (b) Dispensing of a low refractive index UV curable polymer onto the master. (c) Sealing of the polymer between the master and a glass wafer. (d) UV curing of the polymer. (e) Flipping over of the stack. (f) Separation and removal of the master. (g) Spinning of the high refractive index polymer OrmoClear® HI01 XP. Not shown: bake-out, UV curing of the high refractive index polymer, and removal of inhibition layer.

The topography of the LRI and HRI polymer surfaces were measured with atomic force microscopy (AFM) using a high aspect ratio tip, i.e. after the silicon master removal and after the spin-coating steps, respectively. Figure 4(a) shows a 3D surface scan of the nanoreplicated LRI polymer, and Fig. 4(b) shows the AFM scan profiles for both LRI and HRI polymer surfaces, as averaged over 30 parallel line scans. The side-walls of the LRI layer grating protrusions are not perfectly vertical, and are furthermore less vertical than the grating protrusions of the silicon master. This is thought to be a result of the nanoreplication process itself, either due to relaxation of the cured polymer, or due to deformation of the polymer upon release of the silicon master. However, the trapezoidal shape of the grating protrusions is not believed to negatively impact the performance of the sensor. On the contrary, it has been shown that guided modes in grating waveguides with trapezoidal protrusion shapes generally exhibit lower de-coupling rates than those in square ones [30], and thus exhibit higher resonance quality factors. It is also worth noting that the surface of the HRI polymer does not conform to the grating topography, but rather is flat. This may be a considerable advantage in biological sensing of surface-immobilized analytes, as it excludes any influence of the surface topography on the analyte. Finally, Fig. 4(c) shows a scanning electron micrograph of the nanoreplicated LRI polymer, obtained before the application of the HRI polymer.

The PCS sensor was fabricated from these two particular polymers primarily on account of their suitable refractive indices and chemical properties. UV nanoreplication requires the use of a solvent-free and UV curable polymer, and for the current application, the polymer must furthermore have a low refractive index. Efiron PC-409 satisfies each of these criteria. OrmoClear® HI01 XP was chosen for the waveguide layer due to its high refractive index and

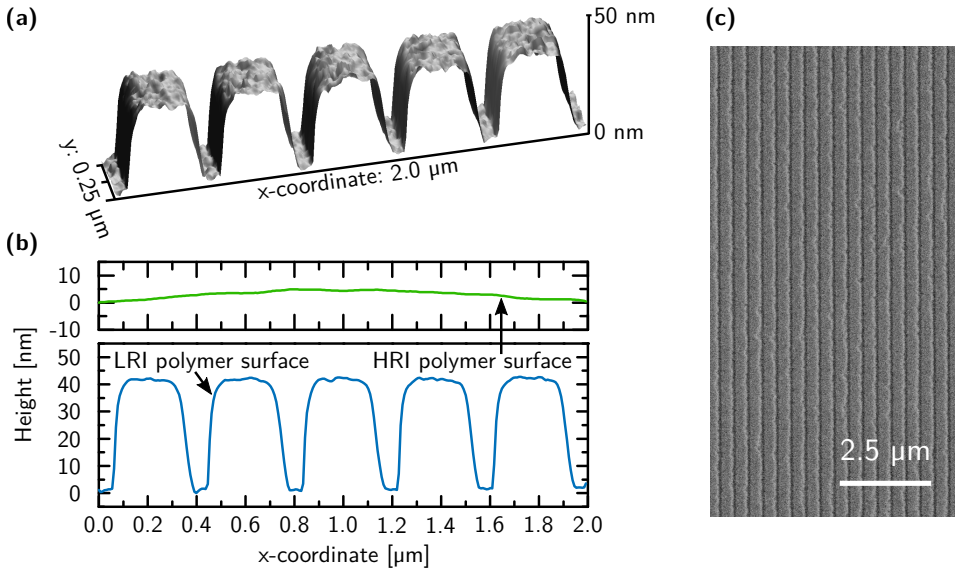

Fig. 4. Characterization of the polymer PCS sensor. (a) A 3D AFM scan of the surface of the low refractive index polymer after the removal of the silicon master. (b) AFM traces of the low refractive index polymer surface and the surface of the high refractive index polymer. Both are averaged over 30 parallel line scans. (c) Scanning electron micrograph of the nanostructured low refractive index polymer surface.

simple processing in terms of diluting and spinning into thin films. Furthermore, it is highly transparent in the visible regime and mechanically rigid after curing.

The silicon master is highly durable when used in UV nanoreplication. In contrast to conventional nanoimprint lithography, the master is neither subjected to high temperatures nor high pressures. Furthermore, the stamp is only exposed to a solvent-free polymer, which does not cause the anti-stiction coating to deteriorate. The authors of the present work have performed over 90 nanoreplications with a single master without degradation in the quality factor of the resonantly reflected wavelength peak.

4. Experimental measurements and results

The reflected spectra from the fabricated PCS sensor were measured by illumination at normal incidence from the back-side, using the experimental setup shown in Fig. 5. Light from a high-brightness, broadband laser-driven light source (Energetiq EQ-99XFC) is fed to the setup via an optical fiber, collimated with a fiber collimator, and then focused with a lens and reflected into a microscope objective by a beamsplitter. The light then emerges collimated from the other side of the objective and illuminates the PCS sensor at normal incidence. The reflected light travels backwards through the objective and beamsplitter and is then simultaneously focused by a microscope tube lens onto the slit of an imaging spectrometer and a camera (CCD A) via a polarizing beamsplitter. The polarizing beamsplitter reflects *s*-polarized light to the spectrometer, while *p*-polarized light passes through it to the camera, where it is captured, transmitted to a computer and used for visual inspection of the PCS sensor and sample positioning. Therefore, when the PCS is oriented as shown here, resonant reflections associated with TE-polarized guided modes correspond to an *s*-polarization and are thus

reflected to the spectrometer, while resonant reflections associated with TM-polarized guided modes correspond to a p-polarization and are transmitted towards the camera. Conversely, in order to measure TM-polarized resonantly reflected light with the spectrometer instead, the PCS can be rotated by 90°, in which case the TE-polarized resonantly reflected light will be directed to the camera. The imaging spectrometer contains a diffraction grating with 1800 lines/mm and projects the input spectrum onto a second camera (CCD B) with a resolution of 12 pm/pixel. The camera is further connected to a computer, where the spectrum is acquired and analyzed.

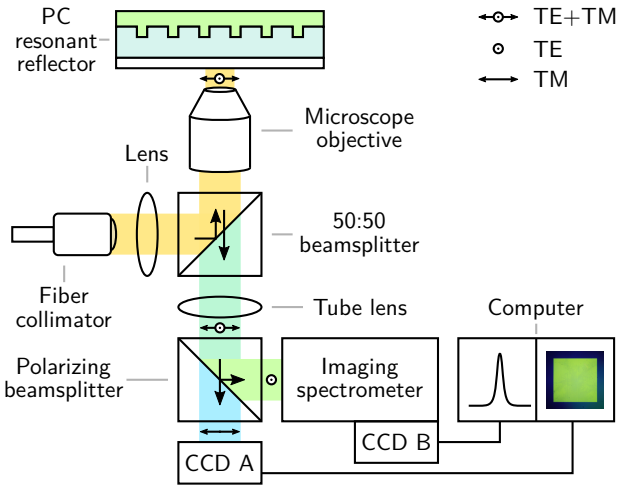

Fig. 5. Experimental setup for measuring resonantly reflected light from the polymer PCS sensor. The structure may exhibit resonant reflection associated with both TM and TE-polarized guided modes. The TM-polarized reflected light is directed to a camera (CCD A) where it is used for visual inspection and sample positioning, whereas the TE-polarized reflected light is directed to an imaging spectrometer and projected onto a second camera for spectral analysis (CCD B).

Using this setup, the reflected TE-polarized resonance peak from the fabricated PCS sensor was measured as a function of refractive index in the sensing region, corresponding to air, deionized water, glycerol, and several dilutions of glycerol in water with weight fractions ranging between 15% and 80%. Figure 6(a) shows an example of two measured spectra, corresponding to the cases of air and deionized water. The resonance peaks are characterized by very narrow, asymmetric peaks with a full width at half maximum intensity (FWHM) of less than 0.9 nm. This narrow resonant linewidth is a direct result of the relatively low refractive index contrast between the substrate and the waveguide layer as well the low grating perturbation [18], both of which lead to long quasi guided mode lifetimes. At shorter wavelengths with respect to the primary reflected peak, a low-intensity secondary peak is visible. However, for the purpose of tracking refractive index changes in the sensing region, this secondary peak is not of concern. Similarly, the TM-polarized reflection was measured, but was found to be barely discernible from the background noise, and is thus not discussed further. Figure 6(b) shows the measured resonance peak wavelength shift with respect to air as a function of refractive index in the sensing region, compared to the model results for the case of $t = 253$ nm (c.f. Fig. 2(b)). The results show clear agreement with the model. Figure 6(b) further shows the sensitivity of the device as a function of refractive index in the sensing region n, calculated using Eq. (5). At a refractive index of $n = 1.33$, the sensitivity of the device is obtained to be $s = 31$ nm/RIU, increasing quickly to $s = 43$ nm/RIU for $n = 1.38$ RIU.

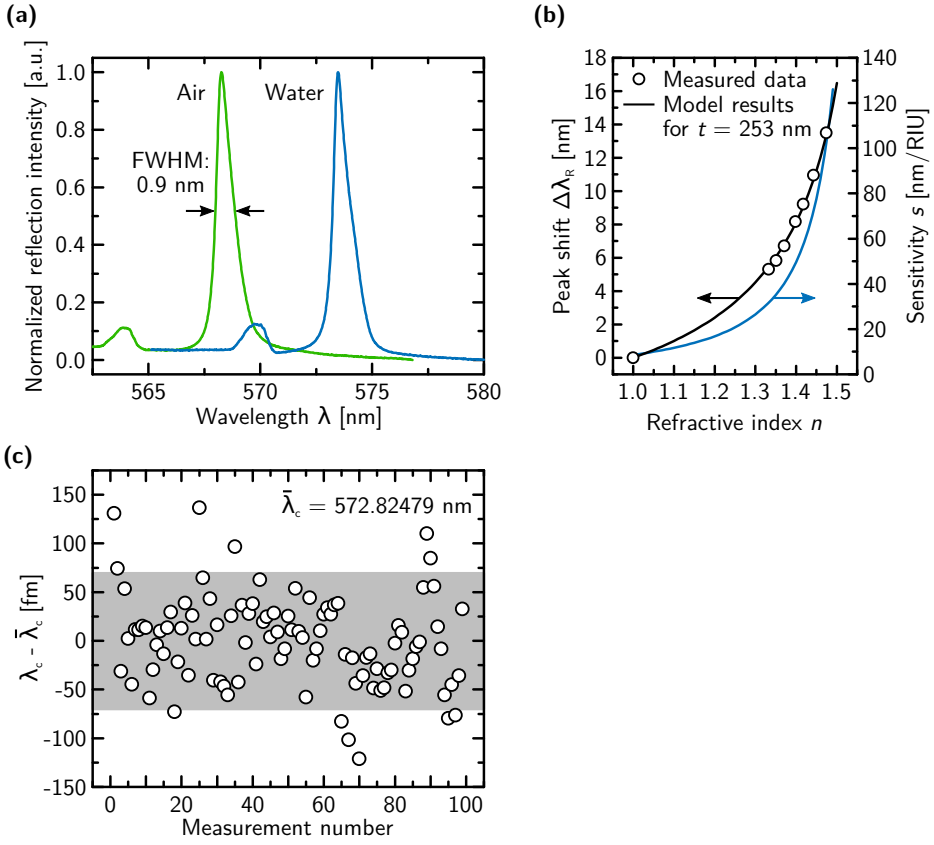

Fig. 6. (a) Acquired resonance spectra of TE polarized reflected light from the polymer PCS sensor when covered with air and deionized water. (b) Measured peak wavelength shift $\Delta\lambda_R$ as a function of refractive index in the sensing region n, compared to simulation results for the case of $t = 253$ nm. The sensitivity of the device s as a function of n, obtained from the slope of $\Delta\lambda_R(n)$ is further shown on the right axis. (c) A series of 100 measurements of the center wavelength λ_c, shown relative to the mean $\bar{\lambda}_c$. The gray area represents three standard deviations of λ_c.

It should be noted that while the presented PCS sensor exhibits a sensitivity lower than those of silicon nitride and titanium dioxide-based structures, this parameter alone does not fully describe the performance of the sensor as it ignores the importance of the resonance linewidth. Instead, the device's performance is better described by its detection limit, which quantifies the smallest refractive index change that the sensor can measure [31]:

$$\mathrm{DL} = \frac{3\sigma}{s} \tag{6}$$

where σ is the standard deviation of the resonance peak wavelength obtained from measurements and is dependent on the linewidth. Therefore, with deionized water in the sensing region, a series of 100 measurements of the TE-polarized reflected peak were acquired, each with an integration time of 100 ms. For each measurement, the center wavelength λ_c was determined using a center of mass calculation:

$$\lambda_c = \frac{\sum_{i=n}^{m} \lambda_i I_i}{\sum_{i=n}^{m} I_i} \tag{7}$$

where I_i is the measured intensity at a wavelength of λ_i in spectral position i, and the integers n and m are chosen such that the calculation encompasses the primary peak only. The results are shown in Fig. 6(c), and the standard deviation of λ_c was determined to be $\sigma = 4.6 \times 10^{-5}$ nm. This yields a detection limit of 4.5×10^{-6} RIU for the polymer PCS sensor when sensing materials with refractive indices around that of water. For biological sensing applications with refractive indices around $n = 1.38$ RIU, the detection limit can be expected to be even lower, or 3.2×10^{-6} RIU.

5. Summary and discussion

An all-polymer photonic crystal slab sensor fabricated by inexpensive vacuum-less techniques involving only UV nanoreplication and polymer spinning has been presented. The structure is shown to exhibit sharp resonant TE-polarized reflection with a FWHM of less than 0.9 nm, a sensitivity of 31 nm/RIU and a detection limit of 4.5×10^{-6} RIU, for sensing materials with refractive indices close to that of water. The sensitivity of the device could in principle be optimized by spinning a thinner layer of the high refractive index waveguide material. This should lead to a higher sensitivity, but possibly also a broadening of the resonance peak, so layer thickness optimization must be carefully considered in order to improve the detection limit. In any case, such a polymer PCS sensor is well-suited for high-throughput industrial production due to the fabrication methods and materials involved, and is therefore ideal for single-use biological and other refractive index sensing applications.

Acknowledgments

The authors acknowledge funding from the European Commission under the Seventh Framework Programme (FP7/2007–2013) under grant agreements number 278204 (Cellomatic), and from the Strategic Research Center PolyNano (10-092322) funded by The Danish Council for Strategic Research. C.V. and C.L.C.S. acknowledge support from the Danish Research Council for Technology and Production Sciences (Grant Nos. 12-126676 and 12-126601.)

5.6 Paper III

Refractive index dispersion sensing using an array of photonic crystal resonant reflectors

Refractive index dispersion sensing using an array of photonic crystal resonant reflectors

Pétur G. Hermannsson,[1] Christoph Vannahme,[1] Cameron L.C. Smith,[1] Kristian T. Sørensen,[1] and Anders Kristensen[1, a)]

Department of Micro- and Nanotechnology, Technical University of Denmark, Ørsteds Plads, Building 345E, DK-2800 Kgs. Lyngby, Denmark

(Dated: 14 September 2015)

Refractive index sensing plays a key role in various environmental and biological sensing applications. Here, a method is presented for measuring the absolute refractive index dispersion of liquids using an array of photonic crystal resonant reflectors of varying periods. It is shown that by covering the array with a sample liquid and measuring the resonance wavelength associated with transverse electric polarized quasi guided modes as a function of period, the refractive index dispersion of the liquid can be accurately obtained using an analytical expression. This method is compact, can perform measurements at arbitrary number of wavelengths, and requires only a minute sample volume. The ability to sense a material's dispersion profile offers an added dimension of information that may be of benefit to optofluidic lab-on-a-chip applications.

In the preceding decades, various miniaturized optical refractive index (RI) sensors based on e.g. surface plasmon resonance, ring resonators, optical fibers, and photonic crystals have been demonstrated[1], whose key advantage is the minimal amount of sample material required for analysis. In these sensors, a change in RI of the analyte material is registered via a change in the transduced output signal, however, the absolute value of the RI is typically not arrived at. Furthermore, the RI of the sample is only probed at a single wavelength, thereby neglecting the potentially valuable information involved in RI dispersion. In this paper, a method for measuring the absolute RI dispersion of liquids using an array of photonic crystal resonant reflectors (PCRR) of varying periods is presented, which has traditionally required the use of the Newton-Fraunhofer method of minimum deviation[2]. The presented method is compact in nature, can perform measurements at an arbitrary number of wavelengths, requires only a minute sample volume, and is thus well-suited for optofluidic lab-on-a-chip applications.

PCRRs, also known as guided-mode resonance filters or reflectors[3], and photonic crystal slabs[4], are optical structures capable of efficiently reflecting a given wavelength interval of out-of-plane incident light. These structures are composed of a periodically modulated high RI dielectric waveguide layer clad in media of lower refractive indices. When illuminated with broad-band light, guided resonances are excited within the waveguide layer, which are quasi-guided modes with finite lifetimes that couple to the far field[4,5]. The modes are continually decoupled out of the waveguide and interfere with both the transmitted and reflected parts of the incident light. At a certain resonance condition, destructive interference occurs between the de-coupled light and the transmitted light, leading to efficient resonant reflection, the linewidth of which is inversely proportional to the resonance lifetime. Depending on whether the incident light is polarized perpendicular or parallel to the grating direction, either transverse-electric (TE) or transverse-magnetic (TM) quasi guided modes will be excited, respectively, and each mode will give rise to resonant reflection[5]. Numerous applications of PCRRs have been suggested and demonstrated[6–9], as well as having made strong inroads into the fields of biological sensing[10,11] and surface imaging[12,13].

Fig. 1(a) shows a schematic illustration of a single PCRR used for the purpose of RI dispersion sensing. It is a three layer dielectric structure composed of a periodically modulated high RI layer (n_2), supported by a polymer substrate (n_3) and covered with a liquid superstrate (n_1), the RI dispersion of which is to be measured. The period of the modulation is Λ, and the thickness of the high RI layer is t.

It has been shown previously that the resonance wavelengths of resonant reflections exhibited by PCRRs can be accurately predicted by modeling the devices as a dielectric slab waveguides in which the propagation constant β is determined by a phase-matching condition[14,15], which, for the case of normally incident light is given by

$$\beta = \frac{2\pi}{\Lambda} \tag{1}$$

and is often referred to as the second-order Bragg condition. For the case of TE-polarized modes in a slab waveguide, the following mode condition must be fulfilled[16]

$$\tan(ht) = \frac{p+q}{h-pq/h} \tag{2}$$

where

$$q = \left[\beta^2 - n_1^2 k_0^2\right]^{1/2} \tag{3}$$

$$h = \left[n_2^2 k_0^2 - \beta^2\right]^{1/2} \tag{4}$$

$$p = \left[\beta^2 - n_3^2 k_0^2\right]^{1/2} \tag{5}$$

a)anders.kristensen@nanotech.dtu.dk; www.nanotech.dtu.dk/ak

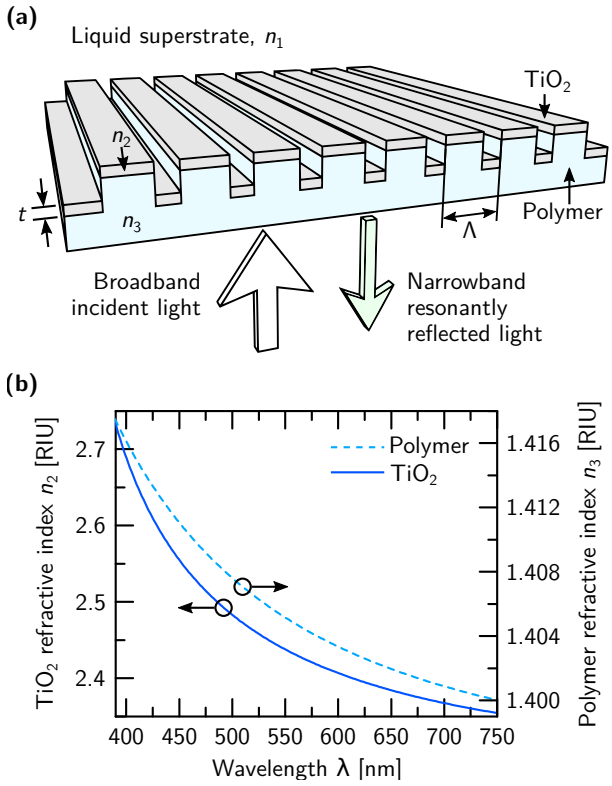

FIG. 1. (a) Schematic illustration of a photonic crystal resonant reflector and its operation. (b) The RI dispersion profiles of the two materials comprising the PCRRs investigated here.

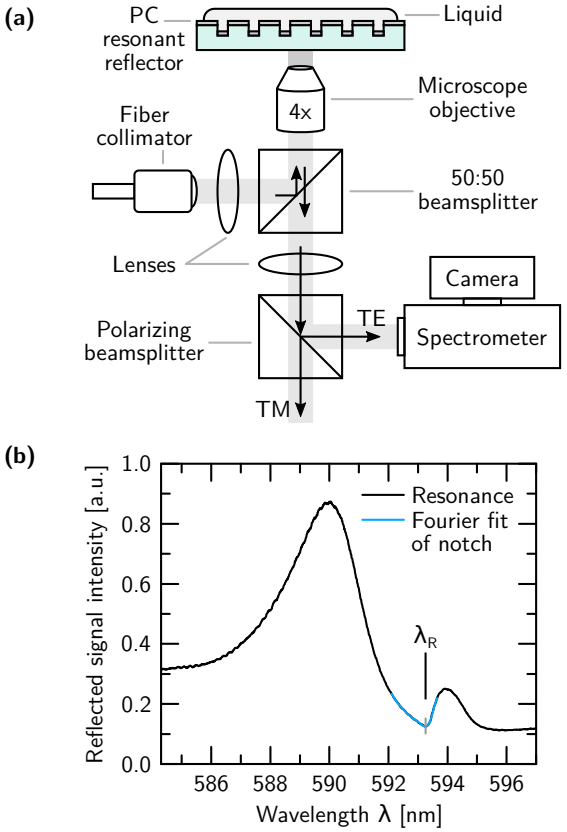

FIG. 2. (a) The experimental setup used for measuring the wavelength spectra of resonantly reflected light associated with TE-polarized quasi guided modes. (b) An example of such an acquired spectrum for the case of $\Lambda = 386$ nm and a glycerol liquid superstrate.

and by solving Eq. (1) and (2) for k_0, the resonance wavelength λ_R can be obtained via $\lambda_R = 2\pi/k_0$. Conversely, Eq. (1) through (3) can be combined to yield the RI of the superstrate in terms of the resonance wavelength as follows

$$n_1(\lambda_R) = \frac{1}{k_0}\sqrt{\frac{4\pi^2}{\Lambda^2} - \left(\frac{h\tan(ht) - p}{1 + p\tan(ht)/h}\right)^2} \qquad (6)$$

where $k_0 = 2\pi/\lambda_R$, and h, p are functions of λ_R. When a PCRR exhibits resonant reflection at a given wavelength λ_R, the light is effectively experiencing the refractive indices of the materials comprising the device and superstrate at that particular wavelength. Thus, if the refractive indices $n_{2,3}$ at this wavelength are known, as well as the structural parameters Λ and t, the RI of the superstrate n_1 *at* λ_R can be calculated using Eq. (6). Utilizing the fact that λ_R is a monotonously increasing function of the grating period Λ,[15] an array of PCRRs with varying grating periods Λ can thus be established such that the resonances span the visible optical regime. By measuring the resonance wavelength exhibited by each PCRR and calculating the corresponding values of $n_1(\lambda_R)$, the RI dispersion of the superstrate can hence be obtained.

For this purpose, an array of PCRRs with grating periods equispaced in the range $\Lambda = (260 - 470)$ nm was fabricated using UV nanoreplication (see Ref. 15 for details). The PCRRs were composed of a low RI polymer substrate (Efiron PC-409, SSCP Co., Ltd) with a surface height modulation of 100 nm and a protrusion duty cycle of 75%, covered with a $t \approx 28$ nm thick layer of ion-beam deposited titanium dioxide. The RI dispersion profiles of the polymer and TiO_2 were obtained by fitting variable angle spectroscopic ellipsometry data to a Cauchy and Tauc-Lorentz oscillator model[17], respectively (Fig. 1(b)).

The wavelength spectra of the resonant reflections associated with TE-polarized quasi guided modes were measured for each of the PCRRs in the fabricated array for several superstrate liquids by illumination at normal incidence from the back-side, using the setup shown in Fig. 2(a). Here, light from a spectrally smooth and broadband light source (Energetiq EQ-99XFC) is fed to the setup via a multimode optical fiber and collimated with a fiber collimator. An image of the fiber tip is then focused and reflected into the image plane of a microscope objective by a lens and 50:50 beamsplitter, respectively. This causes the light to emerge collimated from the other side of the objective and illuminate the PCRR at normal incidence. The reflected light travels back-

wards through the objective and beamsplitter until it encounters a polarizing beamsplitter, where light associated with the TE-polarized modes is reflected to a spectrometer (PI Acton SP2750), and light associated with TM-polarized modes is transmitted. This allows for selective measurement of TE resonances, and eliminates the TM resonances' contribution to the acquired signal noise. The spectrometer contains a diffraction grating with 1800 lines/mm and projects the input spectrum onto a CCD camera (PI Pixis 100) with a resolution of 12 pm/pixel. The camera is further connected to a computer, which records the spectrum. The spectrometer was calibrated in advance with respect to a helium and neon-argon calibration source. An example of an acquired resonance spectrum is shown in Fig. 2(b). The resonance spectra are characterized by a pair of intensity peaks separated by a dip, or notch. The peaks and notch correspond to the edges of two anticrossing photonic bands and the band gap between them, respectively[18]. The wavelength minimum of the notch corresponds to the resonance wavelength λ_R in the model. The notch is a consistent, narrow and clear spectral feature, and is thus advantageous for measuring the resonance wavelength.

Reflected resonance spectra were acquired as a function of period Λ for four different superstrate liquids: purified water, a RI matching oil (AAA 1.3850, Cargille Labs), glycerol (Sigma-Aldrich), and a microscope immersion oil (Type LDF, Cargille Labs). Upon spectral acquisition, the temperatures of the liquids as determined by a thermocouple were as follows: 21 °C in the case of the two oils, 20 °C in the case of water due to evaporative cooling, and 23.5 °C in the case of glycerol due to optical heating. For each measurement, the notch was fitted with a four-term Fourier series (10 fitting parameters), from which the wavelength at the intensity minimum was obtained to yield the resonance wavelength λ_R, as illustrated in Fig. 2(b).

The purpose of the purified water was to serve as a reference liquid to which the PCRR array could be calibrated, and was selected for this function on account of its RI dispersion being accurately known across the entire visible wavelength regime at various temperatures. Using the experimentally obtained resonance wavelengths λ_R as a function of period Λ for the case of purified water, the RI values as yielded by Eq. (6) were fitted via the thickness parameter t to the known RI dispersion of water[19] at 20°C to an accuracy of within 10^{-6} RIU, as shown in Fig. 3(a). Here, the values used for $n_{2,3}(\lambda_R)$ were obtained from the dispersion data in Fig. 1(b) via interpolation. This resulted in a calibration curve of thickness t v.s. period Λ, shown in Fig. 3(b), with the obtained thicknesses all being in the range $28.4 - 28.7$ nm.

The calibration curve, the dispersion data in Fig. 1(b) and Eq. (6) were then used in conjunction with the experimentally obtained resonance wavelengths λ_R for the three remaining liquids in order to calculate their respective dispersion curves, shown in Fig. 4. The results for each material were then fitted to a Cauchy curve of the form $A+B\lambda^{-2}+C\lambda^{-4}$. In the case of the index matching oil and immersion oil, the obtained dispersion curves are compared to data provided by the manufacturer, whereas in the case of the glycerol, the results are compared to

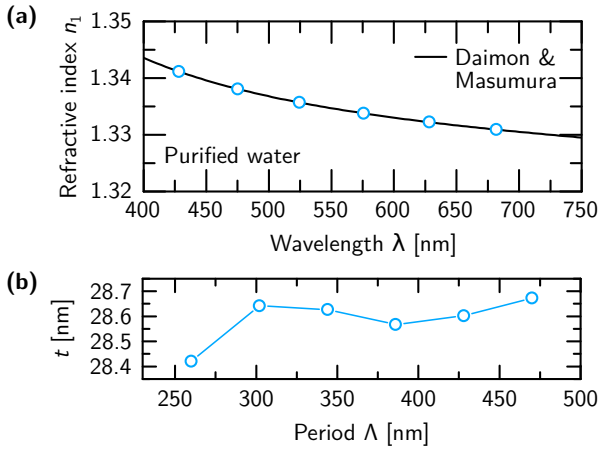

FIG. 3. (a) Datapoints obtained from measurements and Eq. (6), fitted to the dispersion curve of purified water at 20°C as reported by Daimon & Masumura[19]. (b) The resulting calibration curve of thickness t v.s. period Λ.

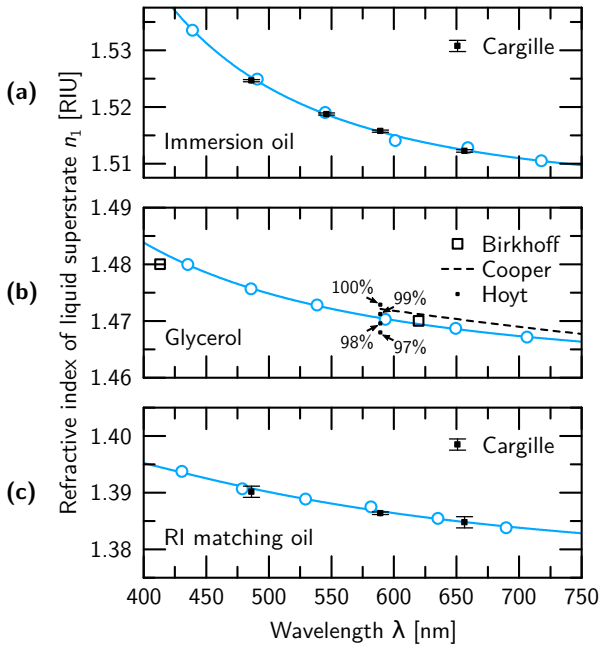

FIG. 4. The obtained dispersion curves using the presented method for the case of three different superstrate liquids: (a) Immersion oil, (b) glycerol, and (c) a RI matching oil. Open circles and solid lines denote datapoints obtained using this method and a corresponding Cauchy-fit, respectively. Other datapoints denote reference values from either material manufacturers (Cargille Labs) or literature (Birkhoff[20], Cooper[21], and Hoyt[22]). The data from Hoyt shows the refractive indices of four different purities of glycerol in terms of water content.

literature-published data. The results show clear agreement between the RI dispersion curves obtained by this method and the reference data, both in terms of the dispersion profile, and in terms of absolute RI values.

In the case of the two oils, the manufacturer's datapoints fall on the obtained Cauchy curve within error, apart from two: the first immersion oil datapoint, and the second RI matching oil datapoint, which are off by 4×10^{-4} RIU and 2×10^{-4} RIU, respectively. In the case of glycerol, the dispersion as reported by Cooper runs in parallel to the obtained dispersion curve, but at higher values. However, as shown by Hoyt[22], the RI of glycerol is quite sensitive to its purity in terms of water content, with Cooper's results corresponding to a purity of $\sim 99.5\%$, and the ones obtained with the present method being consistent with a purity of 98-99%. The purity of the glycerol used here was initially 99% when purchased, but is likely to have become reduced before use, due to e.g. handling, refrigeration, and atmospheric contact, which would account for the difference. Finally, the obtained data agree generally with that of Birkhoff et al., although they only gave their data with two significant digits.

The state-of-the-art method for measuring the RI dispersion of liquids is, and has been since its inception two centuries ago, the Newton-Fraunhofer method of minimum deviation. Here, light is directed through a prism-shaped cell filled with a sample liquid at an angle of incidence such that the deflection caused by the prism is minimized, and by measuring the deflection angle, the refractive index of the liquid can be calculated. This method has an achievable precision of 1×10^{-5} RIU[23], which is practically limited by the thermo-optic coefficient of the liquid and the degree to which the liquid can be thermally stabilized. For high-precision measurements, the RI dispersion of the air surrounding the prism and the prism cell material must be taken into account. The method presented in this work requires only a small amount of sample liquid (100 μL) compared to that required for the method of minimum deviation (~ 70 mL), with a potential for further reduction by the implementing of a microfluidic system to bring the liquid to the PCRR array. As temperature plays a key role in the RI measurements of liquids, this may be beneficial for rapid dispersion measurements, since a much smaller volume must be thermally stabilized. The method can further be extended to measure at an arbitrary number of wavelengths, simply by increasing the number of distinct periods in the array. Since the optical resonance has no overlap with the ambient surroundings, there is no need for correcting the obtained results for the RI of air. Furthermore, this method is compact in nature, and is thus well suited for lab-on-a-chip applications, or other use-cases where space is scarce.

In conclusion, a method for measuring the refractive index dispersion of liquids using an array of photonic crystal resonant reflectors is presented. The method is demonstrated for the case of three different liquids, and found to be in agreement with reference values, both in terms of absolute refractive index values and in terms of the dispersion profile. The method requires that the dispersion of the materials from which the PCRR array is composed be known, as well as an initial calibration step with respect to a liquid of known dispersion, but this step may be easily automated using a commonly available liquid such as purified water. In any case, measuring dispersion as opposed to refractive indices at single wavelengths yields an additional dimension of information about the process being monitored, and offers the capability for monitoring multiple processes simultaneously. Further applications for dispersion sensing may also lie in rapid liquid identification and distinguishing between liquids which, e.g. may have the same RI at a particular wavelength but different dispersion profiles.

ACKNOWLEDGMENTS

The authors acknowledge funding from the European Commission under the Seventh Framework Programme under grant agreement no. 278204 (Cellomatic) and from the Strategic Research Center PolyNano (10-092322). C.V. and C.L.C.S. acknowledge support from the Danish Research Council for Technology and Production Sciences (Grant Nos. 12-126676 and 12-126601).

[1] X. Fan, I. M. White, S. I. Shopova, H. Zhu, J. D. Suter, and Y. Sun, Anal. Chim. Acta **620**, 8 (2008).
[2] S. Krey, D. Off, and A. Ruprecht, **8992**, 89920D (2014).
[3] S. S. Wang, R. Magnusson, J. S. Bagby, and M. G. Moharam, J. Opt. Soc. Am. A **7**, 1470 (1990).
[4] S. Fan and J. D. Joannopoulos, Phys. Rev. B **65**, 235112 (2002).
[5] R. Magnusson and S. S. Wang, Appl. Phys. Lett. **61**, 1022 (1992).
[6] S. S. Wang and R. Magnusson, Appl. Opt. **32**, 2606 (1993).
[7] C. F. R. Mateus, M. C. Y. Huang, Y. Deng, A. R. Neureuther, and C. J. Chang-Hasnain, IEEE Photonics Technol. Lett. **16**, 518 (2004).
[8] D. W. Dobbs and B. T. Cunningham, Appl. Opt. **45**, 7286 (2006).
[9] Y. Ding and R. Magnusson, Opt. Express **12**, 5661 (2004).
[10] B. T. Cunningham, P. Li, B. Lin, and J. Pepper, Sensors Actuators B Chem. **81**, 316 (2002).
[11] Y. Nazirizadeh, U. Bog, S. Sekula, T. Mappes, U. Lemmer, and M. Gerken, Opt. Express **18**, 19120 (2010).
[12] Y. Nazirizadeh, J. Reverey, U. Geyer, U. Lemmer, C. Selhuber-Unkel, and M. Gerken, Appl. Phys. Lett. **102**, 011116 (2013).
[13] W. Chen, K. D. Long, M. Lu, V. Chaudhery, H. Yu, J. S. Choi, J. Polans, Y. Zhuo, B. A. C. Harley, and B. T. Cunningham, Analyst **138**, 5886 (2013).
[14] C. Vannahme, C. L. C. Smith, M. B. Christiansen, and A. Kristensen, Appl. Phys. Lett. **101**, 151123 (2012).
[15] P. G. Hermannsson, C. Vannahme, C. L. C. Smith, and A. Kristensen, Appl. Phys. Lett. **105**, 071103 (2014).
[16] A. Yariv and P. Yeh, *Photonics: Optical Electronics in Modern Communications, 6th ed.* (Oxford University Press, 2006) p. 848.
[17] G. E. Jellison and F. A. Modine, Appl. Phys. Lett. **69**, 2137 (1996).
[18] G. A. Turnbull, P. Andrew, M. J. Jory, W. L. Barnes, and I. D. W. Samuel, Physical Review B **64**, 125122 (2001).
[19] M. Daimon and A. Masumura, Appl. Opt. **46**, 3811 (2007).
[20] R. D. Birkhoff, L. R. Painter, and J. M. Heller, J. Chem. Phys. **69**, 4185 (1978).
[21] P. R. Cooper, Appl. Opt. **22**, 3070 (1983).
[22] L. F. Hoyt, Ind. Eng. Chem. **26**, 329 (1934).

[23]The National Metrology Institute of Germany, private communication (2015).

6 | Summary and outlook

6.1 Summary

In summary, this thesis describes the design and use of guided mode resonance filters for refractive index sensing applications. The guided mode resonance filter devices consist of a nanostructured low refractive index polymer, covered with a high-index waveguide core layer, either of titanium dioxide or a high refractive index polymer. They are fabricated using UV nanoreplication, in which a master with electron-beam defined grating protrusions is used to pattern the surface of the low-index polymer. The resonance spectra of such guided mode resonance filters can be measured in either reflection or in transmission, and experimental setups for each case are detailed. The thesis contains three journal articles. The first describes an analytical model for calculating the resonance wavelengths of guided mode resonance filters in which material dispersion is taken into account via an iterative approach. The model is verified with comparison to experimental results measured in transmission. The second paper describes the design, fabrication and characterization of an all-polymer guided mode resonance filter sensor, and it is shown to exhibit high resonance quality factors and a low detection limit. Such an all-polymer device is expected to be advantageous in low-cost, single-use/disposable sensing applications. In the third paper, a novel method is presented for measuring the refractive index dispersion of liquids using an array of guided mode resonance filters of varying periods. The advantage of this method is that it uses only a fraction of the liquid that other methods require and can measure at an arbitrary number of wavelengths simply by increasing the number of distinct periods in the array.

6.2 Outlook

In addition to the work detailed in this thesis, a patent application has been filed (European Patent Office, appl. no. 14164354.4, April 11, 2014). The

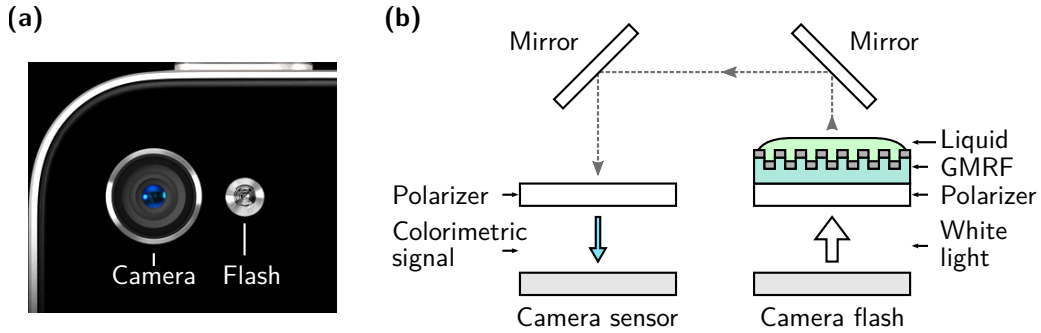

Figure 6.1: (a) The rear facing camera assembly of a smartphone, consisting of a white light flash and camera sensor. (b) A method for colorimetrically measuring the refractive index of a liquid using a guided mode resonance filter combined with a smartphone camera and flash.

application describes a method and system for colorimetrically measuring the refractive index of a liquid using a guided mode resonance filter combined with a smartphone or similar. In one embodiment, the camera flash of a smartphone is used as a broadband illumination source, and the camera used for colorimetric sensor readout, as shown in Fig. 6.1. Linear polarizers are placed above both flash and camera sensor, and the white light emitted by the flash is polarized before passing through a guided mode resonance filter covered with a sample liquid. The refractive index of the liquid uniquely influences the resonant response of the device, and leads to an effective polarization rotation in the resonance band. The transmitted light is then redirected towards the second polarizer e.g. by use of mirrors, which blocks the non-resonant light and produces a colorimetric signal that is captured by the camera sensor. Alternatively, the light may be redirected towards the camera by use of optical fibers, etc. Since the spacing between the camera and flash varies between smartphone models, the instrument can be implemented such that the horizontal distance between the two mirrors and corresponding optical components is adjustable.

Hand-held refractive index sensors are widely used in a variety of industries. In food production, they are used for measuring sugar, alcohol, or the salt content of water. In the field of medical diagnostics and sports medicine, they are used for urine analysis, and in the automotive industry, they are used for gauging the condition of oils, and the amount of antifreeze in coolants, etc. The commercial leader in the field of hand-held refractometers (Atago) sells a specially tailored refractometer for each of these applications. Each of these application-specific refractometers could potentially be replaced by a single smartphone-based refractometer system, taking advantage of the wide-

spread ownership of smartphones. Such a refractometer system would meet the needs of each application by an application-specific calibration curve as part of a computer program running on the smartphone. An added benefit of using such a computerized network-enabled device is that measurements can be rapidly compared to previously obtained results stored locally, or historical results obtained and shared by others, stored remotely. This could e.g. be advantageous in the field of wine-making for selecting the optimum time for harvest.

Research involving guided mode resonance filters continues to progress at a steady pace, and scientists are continually coming up with novel and exciting uses for them. This is at least in part due to the fact that they can be made from a wide variety of materials in a number of geometrical configurations, and thus their operation is dependent on a large parameter space. Due to their ability to support narrow, polarization dependent resonant reflection that is sensitive to refractive index changes within the region overlapped by the optical resonance, they have made strong inroads into the field of label free biological sensing[1] and two-dimensional surface imaging.

In two-dimensional surface imaging, the optical density of a sample at the surface of the high-index layer of a guided mode resonance filter leads to a spatially-dependent shift in the reflected resonance peak wavelength. By use of an imaging spectrometer and stage scanning, a two dimensional image may be generated from the peak wavelengths. Two dimensional imaging without the use of moving parts has been demonstrated using distributed feedback laser sensors in which the lateral spatial coordinate is obtained by the use of gratings of multiple periods, and the vertical spatial coordinate from image spectrometer readout [79]. This same approach could be taken using passive guided mode resonance filter structures. The spatial resolution in the lateral coordinate is limited by the quality factor of the resonance, so the guided mode resonance filters should be designed accordingly.

The thermo-optic tuning of the resonance of a guided mode resonance filter composed of amorphous silicon has been demonstrated at telecommunication wavelengths by means of resistive heating [46]. Such tuning has not been demonstrated in the visible regime, but could potentially be realized with the use of a periodic indium tin oxide waveguide core layer in a polymer cladding. Indium tin oxide has been shown to exhibit a positive thermo-optic response (i.e. refractive index increases with temperature) of the order of 10^{-4} K^{-1} [107], whereas polymers generally have negative thermo-optic

[1]Currently, there are at least two commercial companies that are developing biological sensing technology based on guided mode resonance filters: Resonant Sensors Incorporated, and byosens GmbH.

responses of the same order of magnitude. Since indium tin oxide is conductive, a current can be passed through it laterally, leading to resistive heating in the waveguide core region. Since the core and the cladding have opposite thermo-optic responses, the quasi guided mode would become more confined, potentially leading to meaningful resonance tuning for acceptable temperatures. Furthermore, the non-uniform temperature profile will lead to a non-uniform refractive index profile in the polymer regions, further disturbing the mode and altering its resonance. A similar effect could potentially be realized without the use of electrodes by integrating an absorbing dye into the polymer. By illuminating the structure with a laser source corresponding to the absorption peak of the dye, the structure could be optically heated to produce a change in resonance. Such an approach would be advantageous in e.g. optical switching applications.

Bibliography

[1] D. Rittenhouse, "An optical problem, proposed by Mr. Hopkinson, and solved by Mr. Rittenhouse," Transactions of the American Philosophical Society **2**, 201–6 (1786).

[2] R. W. Wood, "On a remarkable case of uneven distribution of light in a diffraction grating spectrum," Proceedings of the Physical Society of London **18**, 269–75 (1902).

[3] L. Rayleigh, "On the dynamical theory of gratings," Proceedings of the Royal Society of London **79**, 399–416 (1907).

[4] U. Fano, "The theory of anomalous diffraction gratings and of quasi-stationary waves on metallic surfaces (Sommerfeld's waves)," Journal of the Optical Society of America **31**, 213–22 (1941).

[5] D. Maystre, "Theory of Wood's Anomalies," in "Plasmonics, from basics to advanced topics," , S. Enoch and N. Bonod, eds. (Springer, 2012), pp. 39–83.

[6] C. H. Palmer, "Diffraction grating anomalies. II. coarse gratings," Journal of the Optical Society of America **46**, 50–53 (1956).

[7] A. Hessel and A. A. Oliner, "A new theory of Wood's anomalies on optical gratings," Applied Optics **4**, 1275–97 (1965).

[8] M. Neviere, P. Vincent, R. Petit, and M. Cadilhac, "Systematic study of resonances of holographic thin film couplers," Optics Communications **9**, 48–53 (1973).

[9] M. Neviere, R. Petit, and M. Cadilhac, "About the theory of optical grating coupler-waveguide systems," Optics Communications **8**, 113–17 (1973).

[10] L. Mashev and E. Popov, "Zero order anomaly of dielectric coated gratings," Optics Communications **55**, 377–80 (1985).

[11] H. L. Bertoni, L.-H. S. Cheo, and T. Tamir, "Frequency-selective reflection and transmission by a periodic dielectric layer," IEEE Transactions on Antennas and Propagation **37**, 78–83 (1989).

[12] M. Gale, K. Knop, and R. Morf, "Zero-order diffractive microstructures for security applications," Proceedings of SPIE, Optical Security and Anticounterfeiting Systems **1210**, 83–89 (1990).

[13] S. S. Wang, R. Magnusson, J. S. Bagby, and M. G. Moharam, "Guided-mode resonances in planar dielectric-layer diffraction gratings," Journal of the Optical Society of America A **7**, 1470–74 (1990).

[14] R. Magnusson and S. S. Wang, "New principle for optical filters," Applied Physics Letters **61**, 1022–24 (1992).

[15] S. S. Wang and R. Magnusson, "Theory and applications of guided-mode resonance filters," Applied Optics **32**, 2606–13 (1993).

[16] R. Magnusson, S. S. Wang, T. D. Black, and A. Sohn, "Resonance properties of dielectric waveguide gratings: theory and experiments at 4-18 GHz," IEEE Transactions on Antennas and Propagation **42**, 567–69 (1994).

[17] S. S. Wang and R. Magnusson, "Design of waveguide-grating filters with symmetrical line shapes and low sidebands." Optics Letters **19**, 919–21 (1994).

[18] R. Magnusson and S. S. Wang, "Transmission bandpass guided-mode resonance filters," Applied Optics **34**, 8106–9 (1995).

[19] T. K. Gaylord and M. G. Moharam, "Analysis and applications of optical diffraction by gratings," Proceedings of the IEEE **73**, 894–937 (1985).

[20] T. K. Gaylord and M. G. Moharam, "Planar dielectric grating diffraction theories," Applied Physics B Photophysics and Laser Chemistry **28**, 1–14 (1982).

[21] S. Peng and G. M. Morris, "Experimental demonstration of resonant anomalies in diffraction from two-dimensional gratings," Optics Letters **21**, 549–51 (1996).

[22] S. Peng and G. M. Morris, "Resonant scattering from two-dimensional gratings," Journal of the Optical Society of America A **13**, 993–1005 (1996).

[23] D. Rosenblatt, A. Sharon, and A. A. Friesem, "Resonant grating waveguide structures," IEEE Journal of Quantum Electronics **33**, 2038–59 (1997).

[24] A. Sharon, D. Rosenblatt, and A. A. Friesem, "Resonant grating–waveguide structures for visible and near-infrared radiation," Journal of the Optical Society of America A **14**, 2985–93 (1997).

[25] S. Fan and J. D. Joannopoulos, "Analysis of guided resonances in photonic crystal slabs," Physical Review B **65**, 235112 (2002).

[26] M. A. Cooper, ed., *Label-free biosensors* (Cambridge University Press, 2009).

[27] R. Magnusson, M. Shokooh-Saremi, and E. G. Johnson, "Guided-mode resonant wave plates," Optics Letters **35**, 2472–74 (2010).

[28] C. F. R. Mateus, M. C. Y. Huang, Y. Deng, A. R. Neureuther, and C. J. Chang-Hasnain, "Ultrabroadband mirror using low-index cladded subwavelength grating," IEEE Photonics Technology Letters **16**, 518–20 (2004).

[29] X. Fu, K. Yi, J. Shao, and Z. Fan, "Nonpolarizing guided-mode resonance filter," Optics Letters **34**, 124–26 (2009).

[30] T. Alasaarela, D. Zheng, L. Huang, A. Priimagi, B. Bai, A. Tervonen, S. Honkanen, M. Kuittinen, and J. Turunen, "Single-layer one-dimensional nonpolarizing guided-mode resonance filters under normal incidence," Optics Letters **36**, 2411–13 (2011).

[31] M. J. Uddin and R. Magnusson, "Highly efficient color filter array using resonant Si3N4 gratings," Optics Express **21**, 12495–506 (2013).

[32] M. Shyiq Amin, J. Woong Yoon, and R. Magnusson, "Optical transmission filters with coexisting guided-mode resonance and Rayleigh anomaly," Applied Physics Letters **103**, 131106 (2013).

[33] D. B. Mazulquim, K. J. Lee, J. W. Yoon, L. V. Muniz, B.-H. V. Borges, L. G. Neto, and R. Magnusson, "Efficient band-pass color filters enabled by resonant modes and plasmons near the Rayleigh anomaly," Optics Express **22**, 30843–51 (2014).

[34] T. Khaleque, H. G. Svavarsson, and R. Magnusson, "Fabrication of resonant patterns using thermal nano-imprint lithography for thin-film photovoltaic applications," Optics Express **21**, A631–41 (2013).

[35] T. Khaleque and R. Magnusson, "Light management through guided-mode resonances in thin-film silicon solar cells," Journal of Nanophotonics **8**, 083995 (2014).

[36] T. Buss, C. L. C. Smith, and A. Kristensen, "Electrically modulated transparent liquid crystal -optical grating projection," Optics Express **21**, 1820–29 (2013).

[37] E. Feigenbaum, K. Diest, and H. A. Atwater, "Unity-order index change in transparent conducting oxides at visible frequencies," Nano Letters **10**, 2111–16 (2010).

[38] K. Leosson, T. Rosenzveig, P. G. Hermannsson, and A. Boltasseva, "Compact plasmonic variable optical attenuator," Optics Express **16**, 15546–52 (2008).

[39] P. G. Hermannsson and K. Leosson, "Simulations of thermo-optic long-range surface plasmon polariton optical circuits," Proceedings of SPIE, Nanophotonics II **6988**, 69880A (2008).

[40] R. M. Parker, J. C. Gates, H. L. Rogers, P. G. R. Smith, and M. C. Grossel, "Using the photoinduced reversible refractive-index change of an azobenzene co-polymer to reconfigure an optical Bragg grating," Journal of Materials Chemistry **20**, 9118–25 (2010).

[41] L. Fábián, E. K. Wolff, L. Oroszi, P. Ormos, and A. Dér, "Fast integrated optical switching by the protein bacteriorhodopsin," Applied Physics Letters **97**, 023305 (2010).

[42] D. W. Dobbs and B. T. Cunningham, "Optically tunable guided-mode resonance filter," Applied Optics **45**, 7286–93 (2006).

[43] A. Dér, S. Valkai, L. Fábián, P. Ormos, J. J. Ramsden, and E. K. Wolff, "Integrated optical switching based on the protein bacteriorhodopsin," Photochemistry and Photobiology **83**, 393–96 (2007).

[44] F. Yang, G. Yen, G. Rasigade, J. A. Soares, and B. T. Cunningham, "Optically tuned resonant optical reflectance filter," Applied Physics Letters **92**, 091115 (2008).

[45] F. Yang, G. Yen, and B. T. Cunningham, "Voltage-tuned resonant reflectance optical filter for visible wavelengths fabricated by nanoreplica molding," Applied Physics Letters **90**, 261109 (2007).

[46] M. J. Uddin and R. Magnusson, "Guided-mode resonant thermo-optic tunable filters," IEEE Photonics Technology Letters **25**, 1412–15 (2013).

[47] M. J. Uddin and R. Magnusson, "Efficient guided-mode-resonant tunable color filters," IEEE Photonics Technology Letters **24**, 1552–54 (2012).

[48] B. T. Cunningham, P. Li, B. Lin, and J. Pepper, "Colorimetric resonant reflection as a direct biochemical assay technique," Sensors and Actuators B: Chemical **81**, 316–28 (2002).

[49] J. Homola, S. S. Yee, and G. Gauglitz, "Surface plasmon resonance sensors: review," Sensors and Actuators B: Chemical **54**, 3–15 (1999).

[50] D. Threm, Y. Nazirizadeh, and M. Gerken, "Photonic crystal biosensors towards on-chip integration," Journal of Biophotonics **5**, 601–16 (2012).

[51] B. T. Cunningham, M. Zhang, Y. Zhuo, L. Kwon, and C. Race, "Review of recent advances in biosensing with photonic crystal surfaces," IEEE Sensors Journal **PP**, 1–40 (2015).

[52] B. Lin, J. Qiu, J. Gerstenmeier, P. Li, H. Pien, J. Pepper, and B. T. Cunningham, "A label-free optical technique for detecting small molecule interactions," Biosensors and Bioelectronics **17**, 827–34 (2002).

[53] B. T. Cunningham, B. Lin, J. Qiu, P. Li, J. Pepper, and B. Hugh, "A plastic colorimetric resonant optical biosensor for multiparallel detection of label-free biochemical interactions," Sensors and Actuators B: Chemical **85**, 219–26 (2002).

[54] B. T. Cunningham, P. Li, S. Schulz, B. Lin, C. Baird, J. Gerstenmaier, C. Genick, F. Wang, E. Fine, and L. Laing, "Label-free assays on the BIND system," Journal of Biomolecular Screening **9**, 481–90 (2004).

[55] S. M. Shamah and B. T. Cunningham, "Label-free cell-based assays using photonic crystal optical biosensors," The Analyst **136**, 1090–102 (2011).

[56] S. Kaja, J. D. Hilgenberg, J. L. Collins, A. A. Shah, D. Wawro, S. Zimmerman, R. Magnusson, and P. Koulen, "Detection of novel biomarkers for ovarian cancer with an optical nanotechnology detection system enabling label-free diagnostics," Journal of Biomedical Optics **17**, 081412 (2012).

[57] B. T. Cunningham and R. C. Zangar, "Photonic crystal enhanced fluorescence for early breast cancer biomarker detection," Journal of Biophotonics **5**, 617–28 (2012).

[58] H. Shafiee, E. A. Lidstone, M. Jahangir, F. Inci, E. Hanhauser, T. J. Henrich, D. R. Kuritzkes, B. T. Cunningham, and U. Demirci, "Nanostructured optical photonic crystal biosensor for HIV viral load measurement," Scientific Reports **4**, 4116 (2014).

[59] R. Magnusson, "The complete biosensor," Journal of Biosensors & Bioelectronics **4**, 1–2 (2013).

[60] R. Magnusson, D. Wawro, S. Zimmerman, and Y. Ding, "Resonant photonic biosensors with polarization-based multiparametric discrimination in each channel," Sensors **11**, 1476–88 (2011).

[61] Y. Nazirizadeh, U. Bog, S. Sekula, T. Mappes, U. Lemmer, and M. Gerken, "Low-cost label-free biosensors using photonic crystals embedded between crossed polarizers," Optics Express **18**, 19120–28 (2010).

[62] Y. Nazirizadeh, U. Lemmer, and M. Gerken, "Experimental quality factor determination of guided-mode resonances in photonic crystal slabs," Applied Physics Letters **93**, 261110 (2008).

[63] Y. Nazirizadeh, J. G. Müller, U. Geyer, D. Schelle, E.-B. Kley, A. Tünnermann, U. Lemmer, and M. Gerken, "Optical characterization of photonic crystal slabs using orthogonally oriented polarization filters," Optics Express **16**, 7153–60 (2008).

[64] I. M. White and X. Fan, "On the performance quantification of resonant refractive index sensors," Optics Express **16**, 1020–28 (2008).

[65] C. Ge, M. Lu, S. George, T. A. Flood Jr., C. Wagner, J. Zheng, A. Pokhriyal, J. G. Eden, P. J. Hergenrother, and B. T. Cunningham, "External cavity laser biosensor," Lab on a Chip **13**, 1247–56 (2013).

[66] T. W. Ebbesen, H. J. Lezec, H. F. Ghaemi, T. Thio, and P. A. Wolff, "Extraordinary optical transmission through sub-wavelength hole arrays," Nature **391**, 667–69 (1998).

[67] H. F. Ghaemi, T. Thio, D. E. Grupp, T. W. Ebbesen, and H. J. Lezec, "Surface plasmons enhance optical transmission through subwavelength holes," Physical Review B **58**, 6779–82 (1998).

[68] L. Martín-Moreno, F. J. García-Vidal, H. J. Lezec, K. M. Pellerin, T. Thio, J. B. Pendry, and T. W. Ebbesen, "Theory of extraordinary optical transmission through subwavelength hole arrays," Physical Review Letters **86**, 1114–17 (2001).

[69] M. Zhang, M. Lu, C. Ge, and B. T. Cunningham, "Plasmonic external cavity laser refractometric sensor," Optics Express **22**, 20347–57 (2014).

[70] M. Zhang, C. Ge, M. Lu, Z. Zhang, and B. T. Cunningham, "A self-referencing biosensor based upon a dual-mode external cavity laser." Applied Physics Letters **102**, 213701 (2013).

[71] C. Vannahme, C. L. C. Smith, M. B. Christiansen, and A. Kristensen, "Emission wavelength of multilayer distributed feedback dye lasers," Applied Physics Letters **101**, 151123 (2012).

[72] C. Vannahme, M. C. Leung, F. Richter, C. L. C. Smith, P. G. Hermannsson, and A. Kristensen, "Nanoimprinted distributed feedback lasers comprising TiO2 thin films: design guidelines for high performance sensing," Laser & Photonics Reviews **7**, 1036–42 (2013).

[73] C. Vannahme, K. T. Soerensen, C. Gade, M. Dufva, and A. Kristensen, "Refractometric monitoring of dissolution and fluid flow with distributed feedback dye laser sensor," Optics Express **23**, 6562–69 (2015).

[74] M. B. Christiansen, J. M. Lopacinska, M. H. Jakobsen, N. A. Mortensen, M. Dufva, and A. Kristensen, "Polymer photonic crystal dye lasers as Optofluidic Cell Sensors," Optics Express **17**, 2722–30 (2009).

[75] C. L. C. Smith, J. U. Lind, C. H. Nielsen, M. B. Christiansen, T. Buss, N. B. Larsen, and A. Kristensen, "Enhanced transduction of photonic crystal dye lasers for gas sensing via swelling polymer film," Optics Letters **36**, 1392–94 (2011).

[76] L. L. Chan, S. L. Gosangari, K. L. Watkin, and B. T. Cunningham, "A label-free photonic crystal biosensor imaging method for detection of cancer cell cytotoxicity and proliferation," Apoptosis **12**, 1061–68 (2007).

[77] W. Chen, K. D. Long, M. Lu, V. Chaudhery, H. Yu, J. S. Choi, J. Polans, Y. Zhuo, B. A. C. Harley, and B. T. Cunningham, "Photonic crystal enhanced microscopy for imaging of live cell adhesion," Analyst **138**, 5886–94 (2013).

[78] Y. Nazirizadeh, J. Reverey, U. Geyer, U. Lemmer, C. Selhuber-Unkel, and M. Gerken, "Material-based three-dimensional imaging with nanostructured surfaces," Applied Physics Letters **102**, 011116 (2013).

[79] C. Vannahme, M. Dufva, and A. Kristensen, "High frame rate multiresonance imaging refractometry with distributed feedback dye laser sensor," Light: Science & Applications **4**, e269 (2015).

[80] A. Yariv and P. Yeh, *Photonics: optical electronics in modern communications* (Oxford University Press, 2006), 6th ed.

[81] S. A. Maier, *Plasmonics: fundamentals and applications* (Springer, 2007).

[82] D. H. Raguin and G. M. Morris, "Analysis of antireflection-structured surfaces with continuous one-dimensional surface profiles," Applied Optics **32**, 2582–98 (1993).

[83] M. G. Moharam and T. K. Gaylord, "Rigorous coupled-wave analysis of planar-grating diffraction," Journal of the Optical Society of America **71**, 811–18 (1981).

[84] M. G. Moharam, D. A. Pommet, E. B. Grann, and T. K. Gaylord, "Stable implementation of the rigorous coupled-wave analysis for surface-relief gratings: enhanced transmittance matrix approach," Journal of the Optical Society of America A **12**, 1077–86 (1995).

[85] M. G. Moharam, E. B. Grann, D. A. Pommet, and T. K. Gaylord, "Formulation for stable and efficient implementation of the rigorous coupled-wave analysis of binary gratings," Journal of the Optical Society of America A **12**, 1068–76 (1995).

[86] D. Maystre, "Rigorous vector theories of diffraction gratings," in "Progress in Optics XXI," , E. Wolf, ed. (North-Holland Physics Publishing, 1984), pp. 3–67.

[87] E. Noponen, A. Vasara, E. Byckling, J. Turunen, J. Miller, and M. Taghizadeh, "Synthesis of diffractive optical elements using electromagnetic theory of gratings," in "Optical Information Technology," , S. D. Smith and R. F. Neale, eds. (Springer-Verlag, 1993), pp. 39–46.

[88] M. Neviere and E. Popov, *Light propagation in periodic media: differential theory and design* (CRC Press, 2002).

[89] R. Magnusson, Y. Ding, K. J. Lee, D. Shin, P. S. Priambodo, P. P. Young, and T. A. Maldonado, "Photonic devices enabled by waveguide-mode resonance effects in periodically modulated films," Proceedings of SPIE, Nano- and Micro-Optics for Information Systems, **5225**, 20–34 (2003).

[90] C. Wei, S. Liu, D. Deng, J. Shen, J. Shao, and Z. Fan, "Electric field enhancement in guided-mode resonance filters," Optics Letters **31**, 1223–25 (2006).

[91] Y. Kanamori, T. Kitani, and K. Hane, "Guided-mode resonant grating filter fabricated on silicon-on-insulator substrate," Japanese Journal of Applied Physics **45**, 1883–85 (2006).

[92] U. Geyer, J. Hauss, B. Riedel, S. Gleiss, U. Lemmer, and M. Gerken, "Large-scale patterning of indium tin oxide electrodes for guided mode extraction from organic light-emitting diodes," Journal of Applied Physics **104**, 093111 (2008).

[93] M. J. Uddin, T. Khaleque, and R. Magnusson, "Guided-mode resonant polarization-controlled tunable color filters," Optics Express **22**, 12307–15 (2014).

[94] S. Y. Chou, P. R. Krauss, and P. J. Renstrom, "Imprint of sub-25 nm vias and trenches in polymers," Applied Physics Letters **67**, 3114–16 (1995).

[95] Y. Nazirizadeh, F. von Oertzen, K. Plewa, N. Barié, P.-J. Jakobs, M. Guttmann, H. Leiste, and M. Gerken, "Sensitivity optimization of injection-molded photonic crystal slabs for biosensing applications," Optical Materials Express **3**, 556–65 (2013).

[96] P. G. Hermannsson, K. T. Soerensen, C. Vannahme, C. L. C. Smith, J. J. Klein, M.-M. Russew, G. Grützner, and A. Kristensen, "All-polymer photonic crystal slab sensor," Optics Express **23**, 16529–39 (2015).

[97] D. A. Czaplewski and L. E. Ocola, "100 keV electron backscattered range and coefficient for silicon," Journal of Vacuum Science & Technology B **30**, 021604 (2012).

[98] J. Chen and C.-s. Poon, "Photocatalytic construction and building materials: From fundamentals to applications," Building and Environment **44**, 1899–906 (2009).

[99] G. E. Jellison, L. A. Boatner, J. D. Budai, B. S. Jeong, and D. P. Norton, "Spectroscopic ellipsometry of thin film and bulk anatase (TiO2)," Journal of Applied Physics **93**, 9537–41 (2003).

[100] J. R. DeVore, "Refractive indices of rutile and sphalerite," Journal of the Optical Society of America **41**, 416–19 (1951).

[101] G. E. Jellison and F. A. Modine, "Erratum: Parameterization of the optical functions of amorphous materials in the interband region," Applied Physics Letters **69**, 2137 (1996).

[102] G. E. Jellison and F. A. Modine, "Parameterization of the optical functions of amorphous materials in the interband region," Applied Physics Letters **69**, 371–73 (1996).

[103] A. Matsutani, M. Hayashi, Y. Morii, K. Nishioka, T. Isobe, A. Nakajima, and S. Matsushita, "SF6-based deep reactive ion etching of (001) rutile TiO2 substrate for photonic crystal structure with wide complete photonic band gap," Japanese Journal of Applied Physics **51**, 098002 (2012).

[104] *The National Metrology Institute of Germany* (Private communication, 2015).

[105] M. Galli, F. Marabelli, and G. Guizzetti, "Direct measurement of refractive-index dispersion of transparent media by white-light interferometry," Applied Optics **42**, 3910–14 (2003).

[106] I. K. Ilev, H. Kumagai, and K. Toyoda, "Refractive-index dispersion measurement of bulk optical materials using a fiber Raman laser widely tunable in the visible and near-infrared," Optical Review **4**, 61–64 (1997).

[107] A. B. Socorro, S. Soltani, I. Del Villar, J. M. Corres, and A. M. Armani, "Temperature sensor based on a hybrid ITO-silica resonant cavity," Optics Express **23**, 1930–37 (2015).

Published by:
DTU Nanotech
Department of Micro- and Nanotechnology
Technical University of Denmark
Ørsteds Plads, building 345B
DK-2800 Kgs. Lyngby

DTU Nanotech
Department of Micro- and Nanotechnology